ATOMIC FORCE MICROSCOPY–BASED INVESTIGATION OF PLASTIC DEFORMATION MECHANISMS IN DISORDERED NANOPARTICLE PACKINGS

Joel Allen Lefever

A DISSERTATION

in

Materials Science and Engineering

Presented to the Faculties of the University of Pennsylvania

in

Partial Fulfillment of the Requirements for the

Degree of Doctor of Philosophy

2018

Supervisor of Dissertation

Robert W. Carpick, John Henry Towne Professor and Chair,
Mechanical Engineering and Applied Mechanics

Graduate Group Chairperson

David J. Srolovitz, Joseph Bordogna Professor,
Materials Science & Engineering

Dissertation Committee
Zahra Fakhraai, Associate Professor, Chemistry
Daeyeon Lee, Professor, Chemical and Biomolecular Engineering
Andrea J. Liu, Hepburn Professor, Physics
Kevin T. Turner, Professor, Mechanical Engineering and Applied Mechanics

ATOMIC FORCE MICROSCOPY–BASED INVESTIGATION OF PLASTIC DEFORMATION MECHANISMS IN DISORDERED NANOPARTICLE PACKINGS

COPYRIGHT
2018
Joel Allen Lefever

ACKNOWLEDGEMENTS

Many people contributed to make this research possible, and I could not begin to list them all here. I would like to thank my advisor, Prof. Robert Carpick, for his advice, guidance, and patience in seeing me through this research.

The five faculty who have served on my thesis committee have been invaluable as well: Prof. Daeyeon Lee, Prof. Dan Gianola, Prof. Andrea Liu, Prof. Kevin Turner, and Prof. Zahra Fakhraai.

I also need to thank all of the members of the Carpick Research Group, past and present, who have helped me with developing experimental procedures, analyzing and interpreting my results, and providing feedback on my work. In particular, I thank Prof. Tevis Jacobs, who was my mentor in the first two years on this project. My two undergraduate students, Qizhan Tam and Jason Mulderrig, have also contributed a great deal of time, labor, and thought to this research project, and it was an honor to work with them.

The staff of the Materials Science & Engineering and Mechanical Engineering Departments have all provided a great deal of support in the logistics of performing my work, including Irene Clements, Pat Overend, Vicky Lee, Abigail Behrends, Peter Litt, Sue Waddington Pilder, Desirae Johnson, and Maryeileen Griffith.

I need to thank Dr. Matt Brukman, Dr. Jamie Ford, Dr. Doug Yates, and Steve Szewczyk for their technical support in working with the atomic force microscopes, electron microscopes, and the materials preparation labs. I could not have done this work without their tireless commitment and willingness to provide help at a moment's notice.

This project has benefited substantially from simulations performed by my collaborators, Dr. Xiaohui Liu at Shanghai Jiao Tong University and Ju Li at Massachusetts Institute of Technology. Their excellent work and technical insights have also been instrumental in directing the experimental component of this project forward.

I must also thank everyone who has inspired me in my teaching endeavors, especially Prof. Kevin Turner, Prof. Andrew Jackson, and Prof. Robert Carpick, who have given me opportunities for pedagogical development as a teaching assistant and laboratory instructor.

Finally, I must thank the faculty of Union College for giving me the opportunity to pursue this dream, as I begin working with them as a visiting assistant professor this Fall.

Use of the facilities of the Nano-Bio Interface Center and the Nanoscale Characterization Facility at the University of Pennsylvania are acknowledged. Funding the Ashton Foundation and from the National Science Foundation (Grants No. DMR-1720530 and DMR-1120901) are also acknowledged.

ABSTRACT

ATOMIC FORCE MICROSCOPY–BASED INVESTIGATION OF PLASTIC DEFORMATION MECHANISMS IN DISORDERED NANOPARTICLE PACKINGS

Joel A. Lefever

Robert W. Carpick

Understanding the plastic deformation mechanisms of disordered materials is a longstanding and complex problem in condensed matter physics and materials science. In particular, the elementary plastic rearrangement in a disordered material is believed to be the shear transformation zone, a localized cooperative motion of a handful of constituents. Although observed in mesoscale systems, the shear transformation zone has never been identified in an experiment at the nanoscale. In the present work, atomic force microscopy is used to probe the mechanical response of thin films of disordered nanoparticle packings that have been deposited by spin-coating and layer-by-layer deposition. Results demonstrate that these materials possess strong heterogeneity in their mechanical properties, which has also been observed in other materials including metallic glass. Topography imaging provides nanometer-level resolution, which allows rearrangements to be observed directly. These are the first rearrangements observed in a three-dimensional disordered material at the nanoscale.

By changing the relative humidity in the atomic force microscope chamber, the size of the condensed capillary is controlled. It is found that increasing the humidity causes the nanoparticle film to transition from a strong, brittle state under ambient conditions to a more ductile state at relative humidity above 90%. At saturation, a nearly viscous state is observed.

Disordered nanoparticle packings exhibit rearrangement events featuring avalanche scaling, which has previously been witnessed in numerous other materials including metallic glass and rocks. This is the first time that avalanche scaling has been observed in nanoscale granular materials. The number of rearrangement events is found to increase at high ambient humidity, but the shape of the distribution remains consistent regardless of the envi-

ronmental conditions. This suggests that avalanche scaling is independent of the strength of particle interactions.

The results presented in this work have implications how nanoparticle thin films might be toughened in commercial applications where they may be subjected to external stress. In addition, the close match in behavior between these nanoparticle packings and other disordered systems suggests that findings related to the present materials can also be applied to other disordered materials, including atomic glasses that cannot be probed at the constituent length scale.

TABLE OF CONTENTS

ACKNOWLEDGEMENTS iii

ABSTRACT v

LIST OF TABLES xi

LIST OF ILLUSTRATIONS xxiv

CHAPTER 1 : Introduction 1
  1.1 Disordered materials 2
    1.1.1 Applications of disordered materials 2
    1.1.2 The jamming transition 3
    1.1.3 Soft spots and mechanical heterogeneity 6
    1.1.4 Shear transformation zones and shear bands 7
    1.1.5 Analogies between disordered granular materials and thermodynamic glasses 12
  1.2 Investigating the mechanical properties of disordered materials using a multi-scale approach 14

CHAPTER 2 : Methods 16
  2.1 Depositing and characterizing the nanoparticle films 16
    2.1.1 Packings of 20 nm silica nanoparticles prepared by spin coating . . . 16
    2.1.2 Packings of 9 nm silica nanoparticles prepared by spin-coating . . . 19
    2.1.3 Titania and nanodiamond nanoparticle packings prepared by layer-by-layer deposition 21
  2.2 Atomic force microscopy and probe calibration 23
  2.3 Atomic force microscopy-based nanoindentation 27

CHAPTER 3 : Heterogeneity in the deformation mechanical response of spin-coated silica nanoparticles 31
3.1 Experimentally probing the sizes of rearrangements and the elastic properties of spin-coated silica nanoparticle films 32
3.2 Scaling of the mechanical response of nanoparticle packings to AFM-based nanoindentation 39
3.3 Identifying time-dependent strengthening mechanisms in nanoparticle packings 40
3.4 Demonstrating how compaction stiffens the nanoparticle packing 42
3.5 Mechanical response of a simulated disordered nanoparticle packing 44
3.6 Concluding remarks 46

CHAPTER 4 : Humidity affects the mechanical response of loosely packed two-component nanoparticle packings 48
4.1 Previous investigations of capillary effects in granular materials 48
4.2 Characterizing mechanical response of layer-by-layer deposited films using nanoindentation 50
4.3 Environmental conditions affect the stiffness and plasticity of disordered nanoparticle packings 51
  4.3.1 Load drops indicate the occurrence of intermittent rearrangement events 55
  4.3.2 A critical transition in behavior occurs upon reaching saturation . . 58
  4.3.3 Estimation of rearrangement sizes from topography images 60
  4.3.4 Estimation of elastic modulus of layer-by-layer assembled disordered nanoparticle packings 62
4.4 Concluding remarks 63

CHAPTER 5 : Loosely packed disordered nanoparticle packings exhibit yielding behavior in agreement with universal avalanche scaling 65
5.1 Review of avalanche scaling literature 65

5.2 Layer-by-layer deposited nanoparticle packings exhibit behavior that is consistent with avalanche scaling 67
5.2.1 The scaling cutoff shifts to higher forces as the applied load increases 71
5.2.2 The shape of the avalanche distribution is independent of environmental conditions 72
5.2.3 Constructing a composite force curve 74
5.2.4 Testing the accuracy of the avalanche scaling exponent 76
5.3 *In situ* TEM nanoindentation experiments allow imaging of rearrangement events 77
5.4 Radial distribution of deformation events exhibits exponential scaling . . . 80
5.5 Concluding remarks 83

CHAPTER 6 : Porosity enhances the ductility of nanoparticle films 84
6.1 Synthesizing and characterizing porous nanoparticle packings 84
6.2 Mechanical properties evaluated on porous films 85
6.3 Evaluation of intrinsic mechanical properties 88
6.4 Concluding remarks 91

CHAPTER 7 : Conclusions 93
7.1 Implications for the general problem of plasticity in disordered materials . . 93
7.2 Future work 96
7.2.1 Simulations facilitate understanding of the significance of material parameters that cannot be directly investigated in experiment 97
7.2.2 Varying deposition conditions can strengthen a disordered nanoparticle packing 98
7.2.3 Means of tuning porosity in layer-by-layer films 98
7.2.4 AFM-based scratch testing experiments suggest how disordered nanoparticle packings may survive working conditions 99

7.2.5 Nanoindentation on a disordered nanoparticle film under biaxial compression . . . 101

7.3 Implications of these results . . . 103

7.3.1 Strengthening films to improve durability in manufactured devices and applications . . . 104

7.3.2 Using disordered nanoparticle packings to model the response of other disordered materials . . . 105

BIBLIOGRAPHY . . . 106

LIST OF TABLES

TABLE 2.1 : Typical settings and parameters used in tapping-mode scanning for collection of topography images. 25

TABLE 3.1 : Experimentally-determined values of effective modulus and the best-fit power laws depicted in Figure 3.2. Displacement for the power law fit is assumed to be nanometers. 36

TABLE 4.1 : Contact stiffness, indentation depth, and energy dissipation each with their standard deviations for trials in the order in which they were performed. N is the minimum number of indentation experiments evaluated at that humidity level. In some specific trials, the stiffness could not be evaluated, but the indentation depth and energy dissipation are still reported. 52

TABLE 6.1 : Measured values of the effective elastic modulus and hardness of nanoparticle films prepared from 20 nm diameter silica nanoparticles, and the mean indentation depths observed for each set of experiments. The film deposited without adjusting the pH had no opportunity for aggregation. The second film was spin-coated immediately after adjusting the pH. All measurements were performed with a maximum load of 400 nN. 90

LIST OF ILLUSTRATIONS

FIGURE 1.1 : Schematic phase diagrams of the jamming transition for (a) frictionless granular materials and (a) granular materials with friction, showing the presence of the fragile and shear-jammed states which develop from particles with friction. The vertical axis indicates the shear stress, while the horizontal axis indicates the packing fraction. Figure reproduced with permission from Ref. [1]. 5

FIGURE 1.2 : Two pictures of an STZ resulting from shearing a 2D disordered material. (a) The early representation by Argon [2], showing a rearrangement of a roughly spherical region by sliding along a plane that bisects the region. (b) A more recent representation by Tanguy et al. [3], in which constituents move in a quadrupolar deformation field which has four lobes of alternating compressive and tensile strain. The vectors represent the motion of constituents resulting from shear applied to the top and bottom surfaces. Several STZs are shown. Figures reproduced with permission from Refs. [2] and [3], respectively. 10

FIGURE 1.3 : (a) A molecular dynamics simulation of a shear band propagating across a metallic glass pillar loaded in compression. The simulation box is 54.3 nm × 27.2 × 5.4 nm. (b) Shear bands occur in a $Zr_{35}Ti_{30}Co_6Be_{29}$ metallic glass pillar that has been loaded in compression. Multiple shear bands occur to accommodate entire vertical displacement; they occur in opposite directions because friction between the indenter and the top surface of the pillar holds the top of the pillar in relative alignment over the bottom of the pillar. Figures reproduced with permission from Refs. [4] and [5], respectively. 11

FIGURE 2.1 : (a) A topographic image of a film prepared from LUDOX CL nanoparticles composed of silica with an alumina coating, collected using tapping-mode AFM, and (b) the phase contrast image that results. (c) A topographic and (d) phase contrast image of a film prepared from LUDOX TM-40 silica nanoparticles without a coating. Note the more variegated, rough appearance of the TM-40 particles, particularly in the areas identified by the arrows. This rough appearance is due to the crystalline structure of these particles. The phase contrast image further shows the valleys between grains on the particles as light colored channels. No evidence of crystallinity has been found in the silica nanoparticles, and they are assumed to be amorphous, creating a much more nearly spherical particle. 17

FIGURE 2.2 : (a) A topographic and (b) a phase shift image of a film prepared from LUDOX SM nanoparticles composed of silica. Particles are roughly spherical; the slight oblong appearances can be attributed to thermal drift or probe asymmetry. Any asymmetry in the shape of the particle would be expected to appear in random directions, unlike the consistent vertical orientation shown here. This film was aged for 50 hours and has a porosity of 37% as measured by fluid cell ellipsometry. This packing fraction is very near the random close packing limit. In addition, the smooth nature of the particles can be seen in the phase image, similar to Figure 2.1b and in contrast to Figure 2.1d. 20

FIGURE 2.3 : (a) A topography scan of the layer-by-layer deposited nanodiamond and titania nanoparticle film. (b) A TEM image showing one such film, demonstrating that particle resolution can be obtained despite imaging the film in cross-section. 24

FIGURE 2.4 : Two directions of approach for the AFM cantilever: (a) in the direction normal to the cantilever axis, as used for nanoindentation experiments, and (b) in the direction normal to the substrate, as used for spring constant calibration. 26

FIGURE 2.5 : (a) A transmission electron micrograph of one of the AFM probe tips used in this study. The best-fit circle to the tip geometry is indicated in white, and has radius 16.7 nm. (b) An example force curve, showing an indentation on a 105 nm thick SiO_2 nanoparticle film. Figure adapted with permission from [6]. 28

FIGURE 3.1 : Topography of a film of silica nanoparticles taken using tapping-mode AFM (a) before and (b) after performing indentations. (c) A difference image, created by carefully aligning images (a) and (b) to correct for drift, and subtracting them. (d) A subset of the center of the difference image between the before and after scans (black square in (a)). The disturbed region limited to a single particle size, approximately 20 nm × 20 nm. Figure adapted with permission from [6]. 33

FIGURE 3.2 : Effective modulus as a function of depth for silica nanoparticle films with thicknesses of 105 nm (a) and 431 nm (b), determined using AFM nanoindentation with various maximum loads P_{max} as shown in the legend. The fits are best fits to $E_{eff} = K_E P_{max}/h_{max}^m$, where K_E and m are fitting parameters. The values of these parameters are presented in Table 3.1. The insets depict the modulus values normalized by P_{max}, demonstrating how all datapoints collapse onto a single curve. Figure reproduced with permission from [6]. . 35

FIGURE 3.3 : Several force curves to a fixed load of 800 nN representing AFM nanoindentations on various locations on a nanoparticle film, showing the significant variability in curve shape and indent depth. Inflection points characteristic of rearrangements are indicated with arrows in the deepest indents. Figure reproduced with permission from [6]. 36

FIGURE 3.4 : The distribution of effective moduli over time. Several probes were used in collecting the data, and each tick mark on the age axis represents an experiment that was performed. The red surface is the best fit surface from Equation 3.1. Each slice in the time axis represents a distinct experiment. The distribution of data points for every (load,time) coordinate is converted to a mean (the grayscale surface) and standard deviation (the black error bars). Some datasets were collected by Qizhan Tam under supervision of the author. Figure reproduced with permission from [6]. 41

FIGURE 3.5 : Several force curves from a repeated indentation on the same site on a spin-coated silica nanoparticle film, showing that the retract curves and subsequent approach curves do not overlap. Figure adapted with permission from [6]. 42

FIGURE 3.6 : (a) Modulus, (b) energy dissipation, (c) total deformation, and (d) recovered (elastic) deformation for consecutive indents on the same location, normalized to the value for the initial indent. Lines connect datapoints corresponding to the same location and set of indents. The stiffness increases slightly with compaction, while the energy dissipation and deformation—all measures of plasticity—decrease. Figure reproduced with permission from [6]. 43

FIGURE 3.7 : (a) Force-distance curves performed in various places on a simulated disordered granular packing. System parameters were tuned to match the parameters of the system investigated in this chapter, with the exception of the adhesion force which was set to five times the estimated value for the present films. The various indentation experiments result in a variety of indentation depths. (b) Force curves representing a series of simulated indentation experiments performed in the same location. Unpublished results reproduced with permission from Xiaohui Liu, Shanghai Jiao Tong University. 45

FIGURE 4.1 : An example of a force curve with the stiffness S used in determining the modulus denoted. Several load drops are also visible as serrations in the approach portion of the curve; one is shown in the inset. 50

FIGURE 4.2 : The measured (a) stiffness, (b) indentation depth, (c) energy dissipated, and (d) the pull-off force resulting from adhesion and capillary forces in the course of performing a nanoindentation experiment at various relative humidity levels. The error bars represent the standard deviation of the dataset; because of the very large sample sizes, the differences between the various distributions are statistically significant with $p < 0.05$ in almost all cases. The connecting lines indicate the order in which the experiments were performed. Experiments were performed by Jason Mulderrig under direct supervision by the author. 52

FIGURE 4.3 : Composite force curves at each selected humidity condition. Each composite force curve represents the average depth of all force curves binned at every load between 0 and 800 nN. The greater indentation depths at high relative humidity, shown in Figure 4.2b, are shown here as well. Only the approach portion of each force curve was incorporated into the average. 53

FIGURE 4.4 : The structure of the condensed water bridges (gray) in a granular material (black) in the (a) pendular, (b) funicular, and (c) capillary states. Figure reproduced with permission from Ref. [7]. 54

FIGURE 4.5 : (a) The average number of load drops occurring at each relative humidity condition investigated in the present study. More load drops are observed at higher humidity levels, excepting at saturation which is discussed in greater detail in Section 4.3.2 (b) Histogram of the magnitude of load drops normalized by the number of indentation experiments performed. Due to experimental challenges, the number of indentation experiments was not equal in all cases. The distribution at each humidity level is roughly exponential, as shown by the dotted lines which are fits to the data. . . . 56

FIGURE 4.6 : A force-displacement curve reflecting an indentation experiment performed under saturated conditions. Compare with Figure 4.1 . The sample deflects by over 30 nm requiring only minimal applied force. Most load drops at saturation occur at low loads, as shown by the arrows. In addition, the pull-off force is able to act over a distance of over 40 nm. This is a much greater distance than in unsaturated conditions, and is a result of the formation of a capillary bridge between the tip and the sample. This force curve is typical of many indentation experiments performed at saturation. The extended regime of deformation at low load is equivalent to that depicted previously in Figure 4.3, but is shown here in greater detail. 59

FIGURE 4.7 : Topography scan of a region collected after 256 nanoindentation experiments were performed on a square grid, under two different environmental conditions: (a) taken immediately after the scanning was complete, while the environment was at 100% humidity, and (b) taken after venting the chamber partially so that the environment was no longer saturated. Because of the abrupt change associated with venting the chamber, an exact measurement of the humidity is unavailable for Image 4.7b, but the relative humidity is almost certainly between 60% and 98%. No difference in scan quality is observed at humidities below 98%. 60

FIGURE 4.8 : (a) An example topography scan, taken prior to the experiments performed at 18% humidity. (b) A difference image; the topography after an indentation experiment has been subtracted from the topography prior to the indentation experiment. The disturbed region is approximately the area of a single particle, with no other particles disturbed. The region corresponds to the square in (a). . 61

FIGURE 5.1 : Scaling collapse of five different material systems onto a universal probability function, demonstrating that avalanche scaling is ubiquitous across many materials. Figure reproduced with permission from [8]. 66

FIGURE 5.2 : Nanoindentation experiments on disordered nanoparticle packings feature avalanche scaling. The probability distribution transitions from a power law to an exponential behavior over the range of load drop magnitudes accessible by experiment. Experiments performed on a comparatively thicker film exhibit more rearrangement events, while experiments performed with a comparatively larger AFM probe exhibit fewer rearrangement events. 68

FIGURE 5.3 : Load drop magnitude distribution data binned two ways: (a) linearly, on a linear axis, and (b) logarithmically, on a logarithmic axis. The dashed lines depict the shape that data with an exponential probability distribution would exhibit under each binning configuration. 70

FIGURE 5.4 : (a) Probability density distribution of load drop magnitude data from a sheared granular packing. The data has been grouped by the magnitude of applied force acting on the sample at the time the rearrangement occurred. The upper-magnitude cutoff moves to the right as the applied force increases. Adapted from [9]. (b) CCDF of load drop data from nanoindentation experiments on a disordered nanoparticle packing. The cutoff marking the right side of the distribution moves to the right under higher loads. This shift is most notable in the middle of the distribution, corresponding to load drop magnitudes between 30 and 80 nN. This region comprises a much larger portion of the data than the region above 90 nN, where some of the CCDFs cross. Figure (a) reproduced with permission from [9]. 71

FIGURE 5.5 : Complementary cumulative distribution function of magnitudes of rearrangement events occurring under a range of humidity conditions. Excepting the case of 100% saturation, there is no monotonic increasing or decreasing trend, suggesting that avalanche scaling is independent of the strength particle interactions. Note that the CCDF is only sensitive to the distribution shape and does not directly depict the absolute number of events. The number of rearrangement events in fact varies greatly between the five conditions shown here, as shown previously in Figure 4.5a. 73

FIGURE 5.6 : (a) A composite force curve (black) produced by averaging the indentation depths of a large number of force curves at every increment of applied force. (b) The average slope of all of the force curves as a function of depth. The mechanical response is approximately linear once the indenting probe has sunken in beyond its radius. 75

FIGURE 5.7 : The distribution of load drop data corresponding to nanoindentation experiments on a disordered nanoparticle packing. The four dotted lines are fits to Equation 5.1, for several values of the avalanche scaling exponent τ. The value of $\tau = 1.24$ is the value determined directly by a least squares fit. The fitted cutoff force magnitude ξ is also given in the legend; the cutoff is seen to vary with the value of τ. 76

FIGURE 5.8 : Two frames of a video from an indentation experiment performed *in situ* under the beam of a transmission electron microscope, viewed from the side, (a) before and (b) after a load drop occurs. In the inset force curve of (b), the load drop is visible at right. The silicon substrate is in the top right behind the inset, the diamond indenter is in the bottom left, and the nanoparticle film is in the center. The arrows point to locations where rearrangements, corresponding with the load drop, are visible. 78

FIGURE 5.9 : The distribution of load drop magnitudes for experiments performed in situ in the TEM. The blue curve represents load drops that occurred before the indenter made contact, which are part of the overall noise floor of the instrument. The root mean square of this noise is approximately 200 nN. The orange curve represents load drops that occurred after the indenter first made contact, but where mechanical oscillations caused the indenter to vibrate out of contact. The yellow curve represents load drops that occurred after the indenter made rigid contact, and was no longer vibrating. 79

FIGURE 5.10 : (a) A difference image collected between two topography scans before and after nanoindentation on a disordered nanoparticle packing, as shown previously in Figure 3.1c. This image features more indentation sites, which facilitates improved statistics. (b) A radial distribution of the heights of every pixel in 1 nm concentric annuli around all of the indentation sites. Beyond a particle radius, the shape of the distribution neatly fits an exponential decay with a decay length comparable to a particle diameter. The error bars represent the standard deviation of the mean of the displacements of all pixels within the annulus. The offset of the asymptote from zero is likely an artifact of the means by which the images were leveled. 81

FIGURE 6.1 : (a) the thickness and (b) the porosity of films prepared after various aggregation times, as measured by fluid-cell ellipsometry. Of these samples, the circled samples were selected for further study. . . . 86

FIGURE 6.2 : The measured (a) stiffness, (b) indentation depth, (c) elastic modulus evaluated via the Hertz model, and (d) energy dissipated resulting from indentation on films of two different species of nanoparticles, aggregated for different periods to produce films of various porosities. For the 20 nm particles, two different peak loads were selected: 800 nN to match with the 8.6 nm particles, and 400 nN to allow for an analysis of elastic modulus and hardness, as discussed in the text. The lines indicate the order in which the experiments were performed, which was randomized. Indentation depth and energy dissipation both decrease as density increases. There is no evidence that porosity affects the measured stiffness of the material. 87

FIGURE 6.3 : The measured (a) effective elastic modulus and (b) for two different films of nanoparticles. Hardness is seen to increase with packing fraction; the elastic modulus is seen to increase only for the 8.6 nm nanoparticles. Both of these trends can be explained by the change in indentation depth shown in Figure 6.2b, as discussed in the main text. The ellipsometry measurements were performed by Jyo Lyn Hor. 89

FIGURE 7.1 : Tapping-mode topography images collected (a) before and (b) after a scratching experiment was performed. The applied load during the scratch test was 400 nN, and the AFM probe moved in a zig-zag pattern from right to left. The scratch pattern is faintly visible in (b), as are several displaced particles. 100

FIGURE 7.2 : Cutaway view of a fixture conceived to allow a thin film to be loaded into compression by bending the substrate. The substrate with a thin film is placed over the hollow fixture and sealed with an O-ring. A vacuum is pulled on the fixture through the hose. Atmospheric pressure causes the substrate to bend, applying a nearly uniform compressive stress at the center of the thin film. By adjusting the pressure and moving to different radial locations, various states of stress can be explored. 102

FIGURE 7.3 : The radial and axial (a) strain and (b) that can be achieved with the indentation jig shown in Figure 7.2. The sample is assumed to be a 500 nm thick nanoparticle packing on a standard size silicon wafer, mounted against a 10 cm O-ring and a vacuum drawn to one half of atmospheric pressure. The lines marked residual stress and strain are rough estimates of the residual tensile stress that results from deposition. 103

CHAPTER 1 : Introduction

The study of disordered, or amorphous, materials is a relatively new component of condensed matter physics and materials science. The latter field was dedicated to the study of metallurgy for the majority of the 20^{th} century; crystalline materials such as metals were at the time the primary engineering material in infrastructure and machinery. A new interest in disordered materials has come about due to increasing usage in computers and miniaturized devices. The class of disordered materials may be broadly characterized as materials in which, at some length scale, constituents are randomly arranged in the absence of any kind of crystalline lattice or superlattice. Straightforward examples include atomic glasses such as silica-based glasses [10], metallic glasses [11], some ceramics, and diamond-like carbon (DLC) [12], but materials containing disordered structure at a larger scale may be included in this class as well. Such materials include disordered nanoparticle packings [6], colloids [13], granular materials such as sand [14], and even larger-scale materials such as sediment and rock. Noncrystalline materials such as polymers may also be considered disordered materials. Despite their drastically different structure, they share certain physical and thermodynamic similarities to other disordered materials, including the presence of a glass transition [15].

The primary mechanism of plastic deformation in a crystalline material is long understood to be the motion of a dislocation, a line defect which may be described as an "error" in the crystal structure consisting of an extra or misaligned half-plane of atoms [16]. By contrast, the primary mechanism of plastic deformation in a disordered material, at the atomic or fundamental constituent length scale, is not so intuitive. It certainly cannot be identified from a snapshot as a defect in the structure, as the constituents have no regular structure. Instead, the elementary rearrangement in a disordered material is understood to be a transient event, which leaves behind no obvious trace of its occurrence. Understanding the mechanics of these rearrangements is an outstanding research problem, although considerable progress has been made to date as will be discussed in Section 1.1.4.

1.1. Disordered materials

1.1.1. Applications of disordered materials

Disordered materials, broadly speaking, have been proposed and used for various commercial applications. For example, the disordered nanoparticle packings that will be investigated here have applications in optical coatings [17], where by adjusting the packing fraction the refractive index may also be tuned to reduce the reflection of visible light. Nanoparticle films which are superhydrophilic prevent the formation of water droplets, thus producing an anti-fogging coating [18, 19]. Nanoparticle films have also been demonstrated for use in nanoscale electronic devices [20], and due to their flexibility compared with crystalline metals, they show potential for use in electronic devices built with flexible substrates [21]. In both cases, the devices are fabricated through nanoprinting techniques. Furthermore, nanoparticle packings can be used in various electrochemical applications, owing to their porosity, which creates plenty of surface area on which electrochemical reactions may occur between the solid and fluid phases. In one example, nanoparticle packings have been used in electrochemical sensors, such as for hydrogen peroxide [22]. In many of these applications, for example in optical coatings and sensors, an exposed film may be susceptible to damage due to stress or scratching, thus necessitating a complete understanding of their mechanical properties. In addition, as will be discussed in Section 1.2, the mechanical properties of nanoparticle packings have relevance to other material systems as well, which are also of substantial scientific interest.

Another disordered material with substantial interest for mechanical and tribological applications is metallic glass. Metallic glasses are alloys of metal and occasionally non-metal constituents, which are deposited from vapor or flash-frozen into a solid state while still maintaining their amorphous structure. Metallic glasses have been proposed for use in various types of microelectromechanical systems [23, 24], for micro-scale gears [25], and for bearings [26]. In all of these applications, their tribological applications benefit from high hardness combined with the very smooth surfaces they can feature due to their non-crystalline state. Metallic glasses have also been shown to be effective materials for biomedical implants [27], as they have been found to be chemically compatible with biological materials and may feature low wear rates. Metallic glasses have also been used in numerous other applications, including athletic equipment, optical and magnetic devices, and sensors [28].

On a larger scale, many geological materials such as sand and silt feature an amorphous structure as well, and understanding these materials is important to understand and control geological processes such as landslides and erosion [29]. Materials including emulsions, which share some similarities to wet sand and mud, also exhibit properties of disordered materials [30]. A greater understanding of any one of these materials will further the understanding of the entire class of materials as well.

1.1.2. The jamming transition

Substantial evidence indicates that disordered granular materials feature a critical transition as a function of packing fraction, applied stress, or temperature known as the jamming transition [31, 32]. At this transition, characterized by a volumetric compression, the packing changes from a loose and free-flowing state to a rigid and fully confined state. Notably, unlike the conventional notion of a phase transition [33], no change in overall structure occurs, aside from the aforementioned compression.

Despite the lack of an instantaneous change in structure, the jamming transition is nevertheless an instantaneous transition under certain assumptions[1]. The critical condition governing this transition is that all degrees of freedom of the system must be constrained [31]. For frictionless spheres in three-dimensional space, an average of six contacting neighbors per sphere [30, 31] are needed to fully constrain the three translational degrees of freedom for each particle in the system, whereas for frictionless disks in two-dimensional space, an average of four contacting neighbors per disk are needed.

---

[1] These assumptions include that the constituents are rigid, smooth, and frictionless, that the applied load is constant, the loading rate is quasistatic, and the boundary conditions fully confine the granular packing.

The critical number of contacts per constituent can be determined for spheres or disks with friction as well, but is more dependent on the assumptions made regarding the nature of contact at the interface. For example, accounting for sliding, rolling, or torsional friction as well as adhesion can eliminate additional degrees of freedom. In these cases, every contact eliminates more than one degree of freedom. Importantly, by incorporating friction, one must also account for rotational degrees of freedom of the constituents, thus increasing the total degrees of freedom of the system. For disks in two-dimensional space with friction, the critical number of contacts is approximately three [32, 1], and for spheres with sliding and torsional friction but no adhesion, the critical number of contacts is four [30], but these figures can vary depending on the friction and adhesion interactions [32].

For a sufficiently large system of frictionless, monodisperse spheres, the jamming transition occurs at a packing fraction of approximately $\Phi_J = 64\%$ [34, 35, 30, 36]. This value may be compared with the crystalline close packing limit, which is 74.1% [34]. The crystalline close packing limit benefits from using long-range order to find a particular configuration where constituents are packed tightly; therefore, crystalline close packing also corresponds with a greater number of contacts per constituent—twelve—compared with six for random close packing. Still, elastic disks or spheres may be compressed to higher packing fractions beyond the jamming transition, corresponding to the jammed region in Figure 1.1a. An increase in shear stress τ can cause the packing to unjam and flow.

Simulations of elastic spheres have demonstrated that polydispersity in sphere sizes can result in a packing fraction greater than the random close-packing limit [36]. The presence of smaller spheres among a matrix of larger spheres allows for the smaller spheres to fill in voids that are too small for the larger spheres. Conversely, incorporating friction or adhesion allows for a disordered packing to transition to a rigid state below the random close packing limit [36], because fewer than six contacts per constituent are needed to eliminate all degrees of freedom, as described previously. Armed with this knowledge, it is possible to surmise some information about a rigid packing by determining its porosity or packing fraction alone. Specifically, a rigid disordered packing with a packing fraction

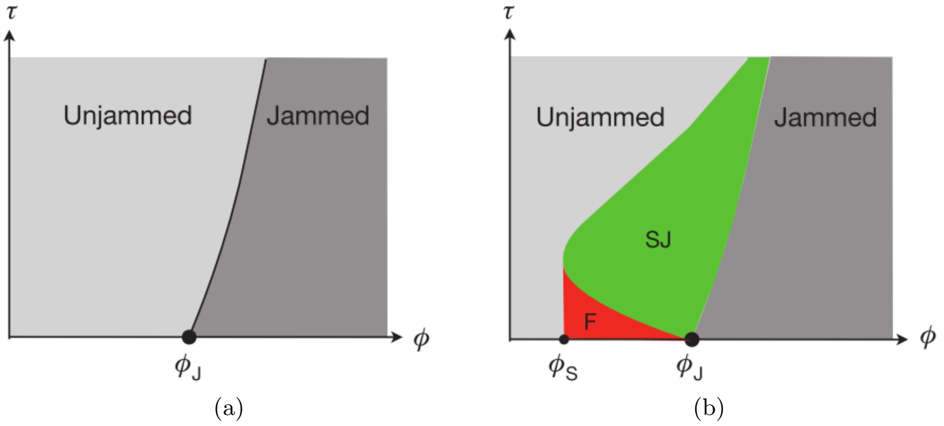

(a) (b)

Figure 1.1: Schematic phase diagrams of the jamming transition for (a) frictionless granular materials and (a) granular materials with friction, showing the presence of the fragile and shear-jammed states which develop from particles with friction. The vertical axis indicates the shear stress, while the horizontal axis indicates the packing fraction. Figure reproduced with permission from Ref. [1].

greater than the random close packing limit must necessarily have either polydispersity, irregularity in constituent shapes, or close-packed crystalline regions. A rigid packing with a packing fraction less than the random close packing limit must include friction, and in absence of external confinement, must contain adhesion as well.

In addition to allowing for jamming below the close packing limit, friction also allows for the introduction of an additional state known as shear jamming [1]. This state was identified by performing shearing and isotropic compression experiments on two-dimensional packings of photoelastic disks. Crossed polarizers on each side of the packing allowed the authors to identify the disks which transmitted the greatest forces. In the shear-jammed state, depicted in the phase diagram in Figure 1.1b, the packing remains rigid only in the presence of shear stress. This state may be sustained down to a packing fraction $\Phi_S < \Phi_J$ under some shear stress. Unlike the jammed state, the shear-jammed state relies on inter-constituent friction to maintain structural stability. The distinction between the shear-jammed state and the fragile state also shown in Figure 1.1b is related to the shape and distribution of the force network that transmits the applied stress state through the material [1]. Specifically, the force network in the shear jammed state fully spans the system and the system remains stable if the applied shear stress is partially relaxed. In the fragile state, the force network does not fully span the system, and the system may become unstable if the stress state is partially relaxed.

At the jamming transition, an abrupt change in mechanical properties occurs; specifically, the material behavior transitions from viscous-like flow to an elastic response [31]. The shear modulus and bulk modulus both become defined at this transition, and any further compression will result in an increase in the moduli as well as an increase in the number of contacts per constituent above and beyond the critical number for stability.

1.1.3. Soft spots and mechanical heterogeneity

Simulations of spring-connected model glasses [37], molecular dynamics-based simulations [38], experiments based on dynamic atomic force microscopy on metallic glass [39], and nanoindentation on metallic glass [40], have all demonstrated that the mechanical properties of disordered materials are not everywhere homogeneous, that is, that locally strong or weak locations exist. These weak regions, known as soft spots, can be viewed as regions where the restorative forces are weak and constituents may be easily disturbed under an applied force or stress. In one seminal study, simulations of a bidisperse mixture of two-dimensional disks which were treated as Hertzian contacts were compressed to a packing fraction well above the jamming transition [37]. The lowest resonance frequencies of the system were considered as the packing was progressively sheared; eventually, one vibrational mode dropped to zero. This drop to zero corresponds to an instability as the restorative force acting on one or more of the disks vanishes. The disks with the greatest displacement associated with a particular low-frequency vibrational mode were identified as soft spots.

Simulations of spring-connected networks have also demonstrated [41] that a greater concentration of soft spots are present at free surfaces. Using the same definition of soft spots as stated previously, an enhancement in mobility was observed in the particles within ten particle diameters of the free surfaces. This finding is analogous to the discovery of a liquid-like behavior on the surface of polymer glasses [42]. In this study, diffusion of polymer around a gold nanoparticle placed on the surface progressed at a rate much greater than would be expected due to the viscosity of the bulk material alone. In addition, in glassy nanotubes, enhanced diffusion was observed in the few nanometers of the surface of the material [43]. When performing surface-based mechanical properties measurements such as nanoindentation on a disordered material, it may be expected that a greater density of soft spots will be observed compared with the bulk material.

A more recent means of identifying and understanding softness has relied on using machine learning techniques to investigate various structure functions associated with every constituent in the material [44]. In this work, loose cylinders were placed upright on a flat platform to form a packing with an overall rectangular shape (a two-dimensional pillar). This column was compressed along its long axis from one end. The motions of the cylinders were tracked with a digital camera, and a simulated reconstruction was produced. The simulation was able to reproduce the overall behavior of the experiment, including many of the locations and times of occurrence of both the individual rearrangements and the shear bands. Machine learning was used to analyze a series of structure functions for every particle, and a measure of softness was created as a linear combination of the values of each structure function. This measure of softness classified 21% of the particles as soft, and 80% of the rearrangements occurred at particles that were identified by the algorithm as soft particles. This machine learning technique is an alternative to the prior definition of softness by way of vibrational modes [37]. It offers more predictive power of the structural configurations of a packing in which rearrangements might occur.

1.1.4. Shear transformation zones and shear bands

Evidence from simulations of disks suggests that the soft spots previously described are the sites at which plastic deformation is prone to occur in a disordered material [45]. Specifically, when a soft spot has been disturbed to the point that one of its vibrational modes reduces to zero frequency, the resulting instability causes a change in structure in which the constituents exchange nearest neighbors [37]. Due to computational complexity, the earlier study [37] ended their simulations after such an instability occurred.

This instability, and the rearrangement that results, is considered to be the fundamental unit of plastic deformation in disordered materials, similar to the dislocation defect in crystalline materials. Indeed, early pictures of this rearrangement sometimes treated it as the geometric equivalent of a dislocation [2, 46]. However, because disordered materials have no regular structure, defects cannot be readily identified: a defected region looks qualitatively the same as an un-defected region.

One of the earliest models of plasticity in disordered materials can be attributed to Spaepen (1977) [47]. This model, which was specifically intended for metallic glasses, treated every individual rearrangement as an atom hopping from one location into another location, driven in part thermodynamically. The rearrangements are isolated to single atoms, and any kind of cooperative rearrangement or motion of any neighboring atoms is minimal, excepting that the motion of one atom may provide a neighboring atom with space to complete a rearrangement. This model can be compared with the much later notion of a T1 process [48] which was developed for liquid-like hard-sphere packings. It is widely viewed [49, 50] that in a typical metallic glass, inadequate free space is available for atoms to move entirely without affecting any neighbors. Nevertheless, the Spaepen model did provide a possible explanation for the transition between homogeneous and heterogeneous flow in metallic glasses, a phenomenon which has been observed repeatedly [51, 52, 53].

Only two years later, Argon [2] developed a new model, this one implying a cooperative rearrangement of multiple atoms, which was driven by an applied shear. Argon [2] created a theoretical picture for what plastic deformation in a disordered material must look like: a cooperative rearrangement of several particles, which relaxes the local stress state. This argument is grounded in reducing the Helmholtz free energy. A rearrangement that allows a region of the packing to conform to the state of stress would reduce the free energy and therefore be thermodynamically favorable; such a rearrangement is named a shear transformation and the region where it occurs a shear transformation zone (STZ). This term had previously been used in the context of crystalline materials, often in the context of a phase transition [54, 55]. It is important to note, however, that a shear transformation in a disordered material is a near-instantaneous, discrete event, occurring in an isolated region, and it does not correspond to any kind of phase transition.

Argon and coworkers developed a physical representation of a shear transformation by producing a disordered material made of bubbles floating on the surface of water [56, 46]. By shearing this packing they were able to observe the types of rearrangements that occur. One such rearrangement is shown in Figure 1.2a; it consists of a collection of bubbles sliding past each other along a plane. The regions on either side of the plane are mostly undisturbed.

This is possibly the first use of a model material to simulate the mechanics of metallic glass [56], a powerful technique which continues in widespread use [57, 58, 6, 59]. The same group further investigated the energy landscape of a shear transformation, observing a series of peaks and valleys in the energy function over time [46]. Despite the simplicity of their model, they were able to reproduce the phenomenon of shear banding, which is the result of a series of shear transformation events occurring in rapid succession. Shear bands are well documented in many disordered materials, including metallic glasses [60, 61] and nanoparticle packings [62].

Numerous recent studies have produced a more complete and rigorous picture of the STZ in both experimental [63, 57, 44] and computational [64, 3, 65, 44] forms. In one study, a molecular dynamics model of a 2D glass was created where the particles interacted via a Lennard-Jones potential function [3]. This packing was sheared and the motions of particles were observed. They consistently found that rearrangements featured a quadrupolar strain state, where the region expanded along one axis and contracted along the opposite axis. This structure is shown in Figure 1.2b. A later 2D model confirmed this quadrupolar strain state [65], and also investigated the structure of a rearrangement that occurs at a free surface. Such a surface rearrangement, under a stress state that is tensile in the plane of the surface, features a similar quadrupolar strain state; however, only three lobes are physically realized as one compressive lobe is truncated by the free surface.

An STZ was later captured experimentally in a model glass constructed from silica

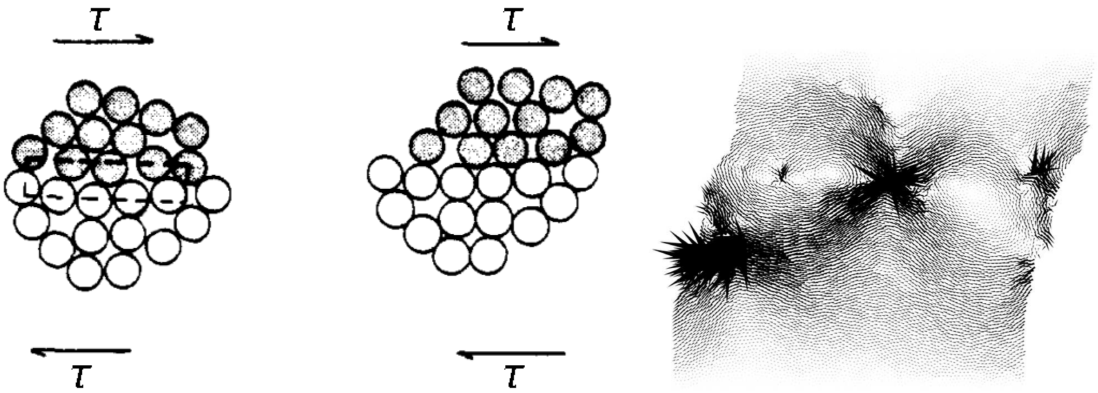

(a) (b)

Figure 1.2: Two pictures of an STZ resulting from shearing a 2D disordered material. (a) The early representation by Argon [2], showing a rearrangement of a roughly spherical region by sliding along a plane that bisects the region. (b) A more recent representation by Tanguy et al. [3], in which constituents move in a quadrupolar deformation field which has four lobes of alternating compressive and tensile strain. The vectors represent the motion of constituents resulting from shear applied to the top and bottom surfaces. Several STZs are shown. Figures reproduced with permission from Refs. [2] and [3], respectively.

spheres of nominally 1.5 μm in diameter [63]. These silica spheres were submerged in a fluid that was matched to the refractive index of the spheres and which contained a fluorescent dye. Confocal microscopy permitted the positions of the colloids to be mapped with high precision as the packing was sheared. As in the previous computational study [3], this experiment revealed a quadrupolar strain state. This experiment with silica colloids was the first observation of an STZ in an experiment outside of the early 2D bubble raft experiments [56, 46], and therefore the first mapping of a shear transformation zone in 3D [63].

The STZ, like the dislocation in crystalline systems, is understood to be the fundamental mechanism of plasticity in disordered materials at the smallest length scale [2, 3]. However, the STZ alone cannot describe bulk deformation, as the total size of the rearrangement is limited to a similar magnitude to the size of the constituents. As in crystalline materials, large-scale deformation results from the activation of multiple shear transformation zones, typically in rapid succession. These can be localized approximately to a plane in a phenomenon known as shear banding [66, 61, 62]. Molecular dynamics simulations can illustrate

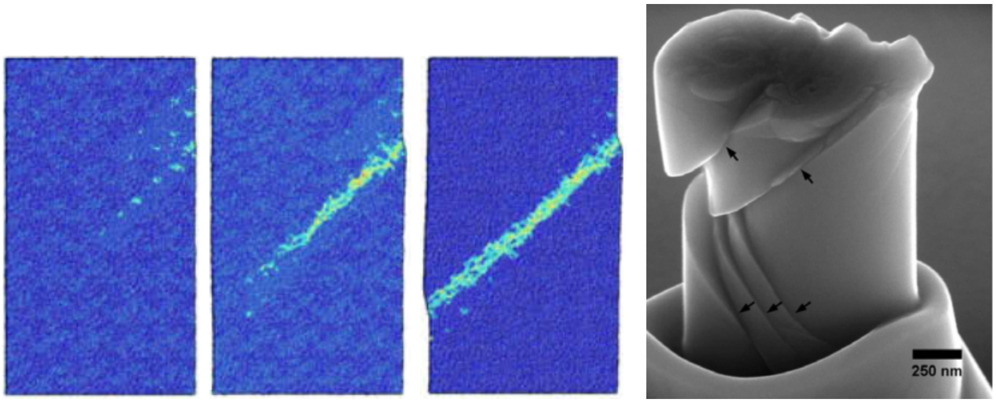

(a) (b)

Figure 1.3: (a) A molecular dynamics simulation of a shear band propagating across a metallic glass pillar loaded in compression. The simulation box is 54.3 nm × 27.2 × 5.4 nm. (b) Shear bands occur in a $Zr_{35}Ti_{30}Co_{6}Be_{29}$ metallic glass pillar that has been loaded in compression. Multiple shear bands occur to accommodate entire vertical displacement; they occur in opposite directions because friction between the indenter and the top surface of the pillar holds the top of the pillar in relative alignment over the bottom of the pillar. Figures reproduced with permission from Refs. [4] and [5], respectively.

the origin of shear banding: in one study, a rectangular pillar representing a Cu−Zr metallic glass was equilibrated and then deformed in compression [4]. This instability propagated to span the entire strained region, as shown in Figure 1.3a, and the propagation rate was close to the speed of sound [4]. This investigation demonstrated that shear bands originate at a single STZ. The STZ which has rearranged no longer supports the stress that it had previously supported, transferring some of the stress to neighboring regions. If the overall stress is great enough, the stress transferred to neighboring regions introduces an instability which causes other STZs to actuate nearby. The activation of a shear band results in relative motion between the bulk material on each side of the shear band, and facilitates large scale shear deformation in much the same way as stacking faults and twin boundaries allow for large-scale deformation in crystals.

Numerous experiments have observed shear bands in metallic glasses [52, 5]. In particular, both tensile tests of nanowires [52] and compressive tests of nanopillars [5] have demonstrated that shear bands tend to form at approximately a 45° angle to the loading direction, which matches the direction of the maximum shear stress. Examples of shear bands in a compression experiment on metallic glass can be seen in Figure 1.3b. Notably, these shear bands—referred to as heterogeneous deformation—are only observed in sufficiently large samples, whereas smaller samples exhibit ductile, homogeneous yielding which is not localized into bands [67, 68, 52]. Shear bands have also been observed in other disordered materials, including colloidal nanoparticles [62] and sand [69].

1.1.5. Analogies between disordered granular materials and thermodynamic glasses

Disordered granular materials are often taken to be analogs to atomic glasses [58, 8, 59]. Both classes of materials generally consist of spherical constituents in a configuration that lacks long-range order. Nonetheless, it is not immediately obvious why, for example, an atomic glass featuring strong metallic bonding would exhibit meaningful similarities to a material such as sand, in which the constituents are significantly larger and far more weakly bonded (if not completely repulsively interacting). Numerous parallels between these two classes of amorphous materials in fact suggest that their behaviors share certain similarities.

One major parallel between them is the presence of a critical transition: in granular materials, the jamming transition discussed in Section 1.1.2; in glassy materials, the glass transition [70]. These two transitions both correspond to a change from a flowing state to a solid, elastic state with no obvious change in structure [71, 70].

In addition to this similarity in the critical transition, both classes of disordered materials exhibit numerous similarities in physics. For example, under certain loading conditions, both exhibit sudden displacement events [9, 72]. The magnitudes of these events follow a power-law population probability distribution, which is consistent with the description of avalanche behavior [8]. Furthermore, numerous similarities are found in the responses of disordered materials subjected to mechanical testing. Mechanical testing performed on twelve different disordered materials and three different simulations of disordered materials all revealed a nearly uniform yield strain of $2.9 \pm 0.3\%$ [59]. This remarkable similarity held true even though the various experiments were performed in various geometries, including compression, tension, shear, and nanoindentation experiments. In addition, the sizes of the constituents spanned a remarkable ten orders of magnitude, with the stiffnesses of the packings spanning twelve orders of magnitude, and yet this uniform yield strain remained constant. Also, the length scales of rearrangements and of the regions described as locally soft (Section 1.1.3) were consistent across all three different simulations and for the three different experiments where the rearrangements could be directly determined via imaging [59].

Perhaps the single largest difference between granular materials and thermodynamic glasses is their thermal stability. Most materials classified as granular materials would be considered to be athermal systems, as the energy associated with rearrangements (1 – 30 keV for the systems to be discussed later in this work) is significantly greater than the thermal energy k_bT (26 meV at room temperature). Systems in which the energy required to induce a rearrangement is significantly greater than the thermal energy, and which may be considered to be athermal, include bubble rafts [56], sand [29, 14], and elastic disks [73]. However, shear transformation zones may be thermally activated in metallic glass, where the activation energy may be on the order of 0.4 eV [61]. Thermally activated shear transformation zones have been observed in 2D silica glass as well [74]. Furthermore, DLC is able to rehybridize at temperatures as low as 100 °C [75]. The process of rehybridization in DLC is a weakening mechanism which is similar to plastic deformation. Therefore, the structures of DLC and metallic glasses might be expected to gradually change in the absence of applied load, solely due to thermal fluctuations. By contrast, the structure of larger scale granular materials would not be expected to spontaneously change in absence of an external force. One implication of this difference is that thermodynamic glasses may be expected to diffuse and mechanically relax at high temperatures [76, 77]. Conversely, granular materials have a quasistatic response and their structures are not affected by temperature, excepting that temperature may change the surface chemistry and bonding structure of the constituents.

1.2. Investigating the mechanical properties of disordered materials using a multi-scale approach

Despite substantial research progress over the last few decades, the plastic deformation mechanisms of disordered materials remain inadequately understood. For example, shear transformations have not yet been experimentally observed at the Ångström length scale. The first observation of an STZ in three dimensions only occurred in 2007 [63], and it was at the micrometer length scale. The physical meaning of the concept of softness, and the way it leads to plastic deformation, is not fully understood. It is still not clear how the mechanical properties of metallic glasses might be tuned by changing deposition conditions [78]. Furthermore, the failure criterion that is most suitable to disordered materials is not yet established: in particular, it is unclear whether metallic glasses fail due to shear or due to deviatoric stress. Evidence suggests that compressive stress may mitigate this failure; however, it is unclear whether the governing factor is hydrostatic compression or axial stress normal to the plane on which shear will occur [66].

In addition to commonalities in yield strain as discussed previously [59], numerous disordered materials also feature avalanche scaling as well [8]. In this regime, the magnitudes of rearrangements exhibit a population probability distribution which features power-law scaling [9, 72]. This observation indicates that the rearrangements have a fractal structure, with many small slip events and proportionately fewer large slip events. With this mounting evidence suggesting that many disordered materials share similar physics, we are able to investigate many different disordered material systems and use each system as a model system for the others. Findings which are consistently observed to hold true in several different disordered material systems may be assumed to be true of other classes of disordered materials as well.

In this thesis, the plasticity and deformation mechanisms of disordered nanoparticle packings are investigated. These materials are large enough that the individual constituents may be observed using atomic force or electron microscopy, but small enough that the attractive forces between constituents are still relevant. This makes it possible to observe rearrangements at one of the smallest length scales ever observed. Nanoparticle packings have already been demonstrated to exhibit shear bands under conditions of nanoindentation [79] and drying [62]. Here, it is demonstrated that disordered nanoparticle packings share in this universal scaling which has been observed in disordered materials; in particular, they exhibit heterogeneity in mechanical response and also feature compaction effects [6].

We treat disordered nanoparticle packings as a model system for disordered materials in general, and use this to address numerous scientific gaps in the understanding of the mechanical response of disordered materials. Individual rearrangements have never been observed in three-dimensional disordered materials at the nanometer length scale. The effect of relative humidity has never been investigated on a disordered granular material on this scale. In addition, avalanche behavior has not been investigated in this class of material system, and will be investigated here for the first time. By altering the length scales of the system, it becomes possible to investigate the effects that each length scale has on the avalanche distribution. The new results presented here suggest how disordered materials will behave in applications involving applied stresses. By extension, these results provide insights on facets of the mechanical behavior of other disordered material systems such as atomic glasses that cannot be investigated by the same techniques with constituent-level resolution.

CHAPTER 2 : Methods

Understanding the mechanics of disordered materials, including disordered nanoparticle packings, requires the development of completely new experimental approaches, as conventional diffraction-based techniques for investigating crystals are unsuitable for these materials. In this chapter, the synthesis methods and mechanical testing techniques used to probe the plastic response of disordered nanoparticle packings will be described.

2.1. Depositing and characterizing the nanoparticle films

In the present work, three primary systems of disordered nanoparticle packings are investigated. Two varieties of silica nanoparticles were prepared by spin-coating, discussed in Sections 2.1.1 and 2.1.2. Additionally, a third material system composed of layer-by-layer deposited titania and nanodiamond was developed, as discussed in Section 2.1.3. Each of these material systems served specific purposes, to be discussed as follows.

2.1.1. Packings of 20 nm silica nanoparticles prepared by spin coating

Nanoparticle packings composed of silica nanoparticles with thin alumina coatings was prepared by spin-coating. The aqueous stock solution of silica nanoparticles (LUDOX CL, Sigma-Aldrich, St. Louis, MO) was diluted from 30% by weight to 5% by weight, and then spin-coated at 1500 RPM onto a clean silicon wafer. Under these conditions, crack-free films of approximately 100 nm thickness were obtained. In order to produce thicker films, this process was performed iteratively. A single deposition step with deposition conditions tuned to produce a thicker film would have induced cracking [80]. The radius of these particles was determined to be 20 ± 4.8 nm using both scanning and transmission electron microscopy (TEM) techniques to directly image the particles. These materials were used for the nanoindentation study outlined in Chapter 3.

This particular type of nanoparticle was selected as a suitable material system for several reasons. First, the particle diameter is comparable to the typical diameter of the tip of

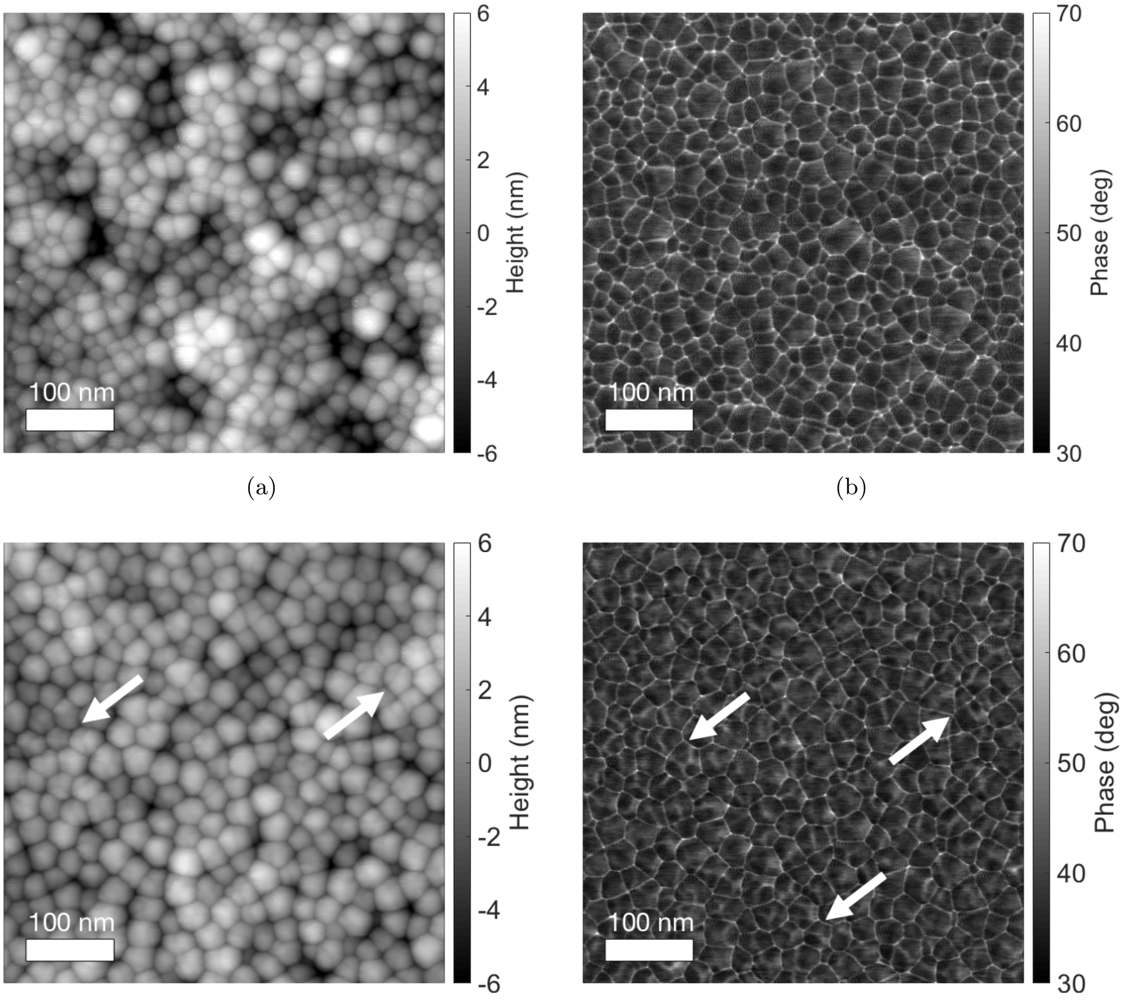

(a) (b) (c) (d)

Figure 2.1: (a) A topographic image of a film prepared from LUDOX CL nanoparticles composed of silica with an alumina coating, collected using tapping-mode AFM, and (b) the phase contrast image that results. (c) A topographic and (d) phase contrast image of a film prepared from LUDOX TM-40 silica nanoparticles without a coating. Note the more variegated, rough appearance of the TM-40 particles, particularly in the areas identified by the arrows. This rough appearance is due to the crystalline structure of these particles. The phase contrast image further shows the valleys between grains on the particles as light colored channels. No evidence of crystallinity has been found in the silica nanoparticles, and they are assumed to be amorphous, creating a much more nearly spherical particle.

an atomic force microscope (AFM) probe (typically 30–50 nm), allowing the particles to be imaged with resolution below the scale of individual nanoparticles. In addition, the nanoparticles themselves have a very uniform geometry due to the amorphous silica structure. TEM indicates that the individual particles are completely amorphous, as no crystalline lattice has been observed. Conversely, other silica nanoparticles can feature a crystalline structure, which results in a faceted, irregular geometry. Figure 2.1 shows AFM topography scans of the nanoparticles used in this study (LUDOX CL, Sigma-Aldrich), as compared with a crystalline nanoparticle (LUDOX TM-40, Sigma-Aldrich, diameter $= 24.2 \pm 2.7$ nm [81]). The topography image of the CL particles (Figure 2.1a) shows less angularity than does the TM-40 (Figure 2.1c). The differences between the smooth amorphous particles and the crystalline particles are even more pronounced in the phase shift images. This channel is particularly sensitive to changes in topography, because a region where both sides of a valley are in contact with the tip will result in greater adhesion and therefore a greater phase shift. Valleys between particles are clearly visible as a network of white lines in both Figures 2.1b and 2.1d. However, more shallow valleys can be seen bisecting many of the particles in Figure 2.1d. These shallow valleys indicate a locally concave regions on the surface of the TM-40 particles corresponding to an edge between facets; by contrast, these valleys are seldom observed on CL particles as shown in Figure 2.1b.

By adjusting the pH and then aging the nanoparticle solution, it is possible to tune the porosity of the resultant film [17]. This technique was originally developed to provide control over the index of refraction of an optical coating. Here, the technique was used to facilitate an investigation of how the packing fraction of a granular material affects its mechanical properties. Specifically, the packing fraction is known to play a significant role in jamming, as discussed previously (Section 1.1.2). Therefore, it is expected that increasing the porosity (and therefore reducing the packing fraction) of the packing would cause the material to transition from an elastic state to a more viscous state that is prone to plastic rearrangements.

The aqueous LUDOX CL solution diluted to 5% by weight, and then was brought to a pH value of 6.4 by addition of 1 M sodium hydroxide solution. Under these conditions the solution began to aggregate into clusters of multiple particles. This process was accelerated by storing the solution at a warm temperature of 60 °C, and after a holding time of zero to 120 hours the nanoparticle packing was deposited by spin-coating at 3000 RPM. Films were synthesized with packing fractions ranging from 47% to the random close-packed limit of 64%. The thickness and porosity of these films were both measured using fluid cell ellipsometry [82]. In this technique, the refractive index of the sample is measured both in air and while the sample is submerged in water. From the difference in refractive indices under these conditions, the volume fraction of water is evaluated. This volume fraction is also the porosity of the material under ambient conditions. These films are used for a study of the effect of packing fraction on the mechanical properties of granular media, as discussed further in Chapter 6.

2.1.2. Packings of 9 nm silica nanoparticles prepared by spin-coating

An additional set of films composed of amorphous silica nanoparticles was employed for the porosity study in Chapter 6. These films were prepared from LUDOX SM nanoparticles (Sigma-Aldrich); the solution was diluted to 5% by weight and the pH was adjusted to 7 using a solution of hydrochloric acid. After aging the solution at 50°C for a predetermined time, the solution was spin-coated onto a silicon wafer at 3000 RPM. These nanoparticles have a diameter 8.6 ± 1.3 nm [81], and an example topography image is shown in Figure 2.2.

These films were used exclusively for the porosity study undertaken in Chapter 6. Because of the small size of the constituents and the similarly small sizes of the voids between the particles, indentation depths were generally less than 20 nm even on films with very high porosity. The low indentation depth satisfied the assumptions used in nanoindentation analysis (Section 2.3), allowing the elastic modulus and hardness to be evaluated using conventional methods [83, 84]. Conversely, nanoindentation on aggregated LUDOX CL particles (discussed in Section 2.1.1) frequently produced indentation depths greater than the radius of the probe. In other words, the tapered shank of the tip was also indenting in

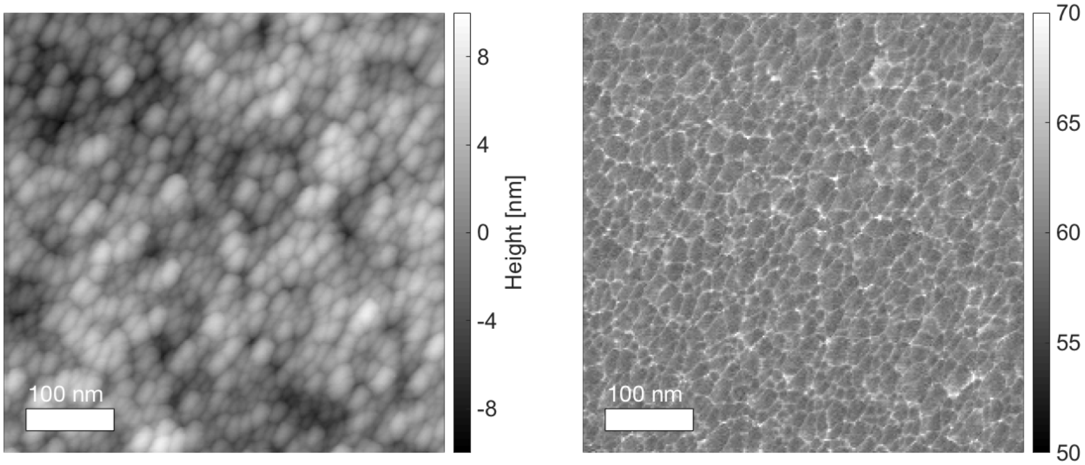

(a) (b)

Figure 2.2: (a) A topographic and (b) a phase shift image of a film prepared from LUDOX SM nanoparticles composed of silica. Particles are roughly spherical; the slight oblong appearances can be attributed to thermal drift or probe asymmetry. Any asymmetry in the shape of the particle would be expected to appear in random directions, unlike the consistent vertical orientation shown here. This film was aged for 50 hours and has a porosity of 37% as measured by fluid cell ellipsometry. This packing fraction is very near the random close packing limit. In addition, the smooth nature of the particles can be seen in the phase image, similar to Figure 2.1b and in contrast to Figure 2.1d.

to the film. In these cases, the assumption of the Oliver & Pharr method described below are no longer valid. Formulating a solution that accounts for the sharp angle and the resulting tangential forces on the contact is a complex problem with no existing solution. This results in uncertainty in the measured elastic modulus and hardness. The primary purpose for investigating this material system was to facilitate a direct measurement of hardness and elastic modulus while tuning the porosity.

Both classes of silica nanoparticles are susceptible to damage under an intense electron beam, which is another piece of evidence suggesting that they are not crystalline. High-energy electrons in the electron beam occasionally break bonds in the specimen, allowing atoms to reconfigure. Beam damage is typically observed in non-crystalline materials where the energy barrier to plastic deformation is low because atoms are not rigidly confined to a lattice and may move to form bonds with other neighbors. Therefore, these systems were not compatible with TEM, and a material system specifically selected to be compatible with TEM was desired, as outlined in the following section.

2.1.3. Titania and nanodiamond nanoparticle packings prepared by layer-by-layer deposition

One facet of the work that follows involves performing nanoindentation *in situ* in a TEM for visualization purposes. In order to perform an experiment in this way, the material must be carefully selected, as the experimental design creates several additional challenges not present in AFM-based work:

1. The nanoparticles must be able to withstand damage resulting from the electron beam. This eliminates most amorphous materials, including the silica nanoparticles discussed previously.

2. The apparatus used for performing these experiments applies a greater force than the AFM, on the order of a few micronewtons. The particles must be stiff to support this load, precluding the use of soft metals such as gold.

3. In order to image the packing, the system must be electron transparent and therefore

no more than a few hundred nanometers thick in the path of the beam. To create such a thin flat sample, the film is deposited onto a narrow wedge. Spin-coating cannot accommodate irregular geometry such as a wedge, so the films must be deposited using a layer-by-layer approach [82]. The layer-by-layer approach involves submersing the substrate alternately into aqueous solutions of two different types of nanoparticles, at which time a layer of particles assembles onto the surface. Of these two solutions one must have a negative zeta potential and the other must have a positive zeta potential under similar pH conditions.

4. Because the TEM images through several layers of particles, it is ideal to select these two nanoparticle solutions such that one is composed of a light element and the other a relatively heavy element, providing adequate Z-contrast.

5. The particles should be similar in size to the systems investigated previously, to facilitate direct comparison. Also, this size is convenient for imaging in the TEM, because the outlines of individual particles may be observed even as the magnification is low enough to resolve the entire indent region.

Using process of elimination, a material system was identified that satisfied all of these requirements: a layer-by-layer deposited film consisting of positively charged anatase titania (US Research Nanomaterials, Houston, TX) and negatively charged nanodiamond (RT-DND-SP, Ray Techniques Ltd., Jerusalem, Israel). The titania nanoparticles have diameters ranging from 5–15 nm, while the nanodiamond have diameters ranging from 3.5–5.5 nm. The titania solution was adjusted to a concentration of 0.05% by weight from a stock concentration of 15% by weight, and 1 M hydrochloric acid was added to lower its pH to 3. The nanodiamond solution was adjusted to 0.05% by weight from its stock concentration of 5% by weight, and the pH was adjusted to 4.

One additional challenge in performing layer-by-layer deposition is that not only must the zeta potentials of the two solutions be opposite, but the acidity of each solution must be nearly equal [82]. This condition maintains opposite charges between successive layers which causes each layer to bind to the preceding layer, while also preventing the preceding layer from becoming unbound and released into the solution. The pH values for each solution are optimized to nearly match, as described previously, while not inducing aggregation for either solution.

Substrates used for layer-by-layer deposition were silicon wafers and silicon wedges (Hysitron, Inc., Eden Prairie, MN) that had been solvent washed and plasma cleaned. The deposition was performed using a dip coater (HMS Series Programmable Slide Stainer, Carl Zeiss, Inc.) which was programmed to immerse the substrate in a bath of the titania solution for at least eight minutes, a duration long enough for the self-limiting deposition step to complete. After the deposition step, the substrate was transferred to each of three rinsing basins for three, one, and one minute respectively. This same process was repeated for the nanodiamond solution and three more rinsing baths. This process of eight solutions produced a single bilayer, and the procedure was repeated between 20 and 300 times depending on the desired film thickness, which was between 100 and 700 nm in all cases. Images of these layer-by-layer films are shown in Figure 2.3, taken using both AFM and TEM. It is possible in the TEM to observe outlines of individual particles as long as those particles are within the focus plane, as shown in Figure 2.3b. The layer-by-layer deposited material system was used for the study of the effects of relative humidity described in Chapter 4, and also for the study of avalanche scaling in Chapter 5.

2.2. Atomic force microscopy and probe calibration

Atomic force microscopy provides a convenient platform to image and investigate the mechanical properties of disordered nanoparticle packings. An AFM employs a thin, flexible cantilever which makes contact with the surface and probes the force acting between the force and the tip [85]. In this work, topography images are collected using tapping mode on a Bruker Dimension Icon AFM (Boston, MA), and a DLC-coated silicon tapping mode cantilever (Tap300DLC, BudgetSensors, Sofia, Bulgaria). These topography images allowed the exact positions of nanoparticles in the film to be determined, and they also confirmed

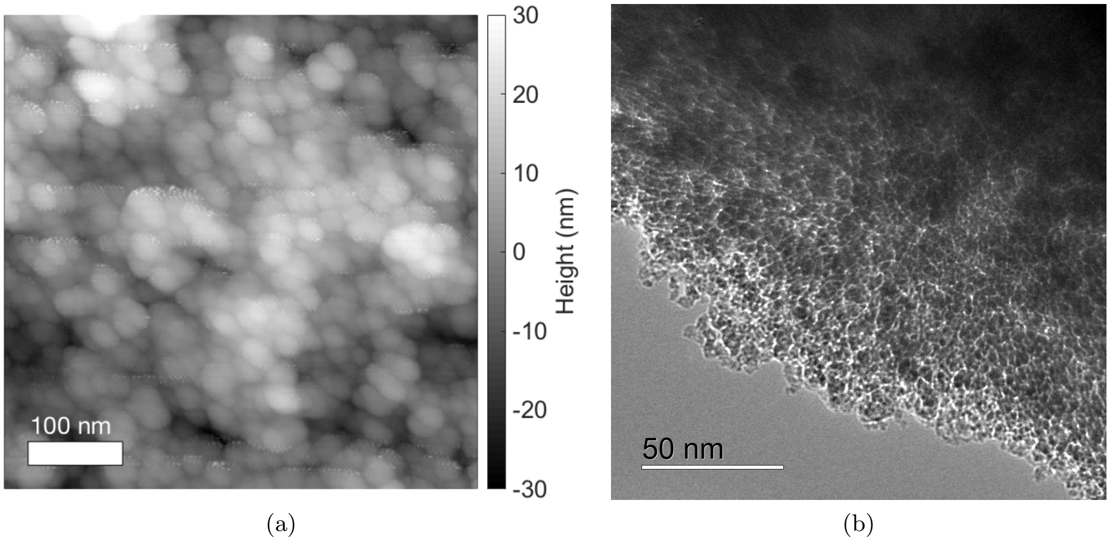

(a)

(b)

Figure 2.3: (a) A topography scan of the layer-by-layer deposited nanodiamond and titania nanoparticle film. (b) A TEM image showing one such film, demonstrating that particle resolution can be obtained despite imaging the film in cross-section.

that the samples were relatively flat and free of contamination.

In addition to being ideal for tapping-mode scanning, this type of probe was necessary to perform the nanoindentation experiments discussed in Section 2.3. Its high stiffness was comparable to that of the film, resulting in good sensitivity, while its DLC coating had the strength needed to apply loads of at least 1.5 μN. Also, the DLC coating exhibited lower adhesion to the nanoparticles compared with more conventional silicon probes, which reduced contamination of the probe with nanoparticles. Typical scan settings are given in Table 2.1.

Of the parameters in Table 2.1, the spring constant, deflection sensitivity, and tip radius must all be carefully calibrated. The spring constant and deflection sensitivity are both required to convert the signal from the AFM photosensitive diode from voltage to force:

$$\text{Force [nN]} = k_{s,\text{probe}} \times S_{\text{defl}} \times (\text{Signal [V]}) \tag{2.1}$$

where $k_{s,\text{probe}}$ is the spring constant of the AFM probe [nN/nm] and S_{defl} is the deflection sensitivity [nm/V], or optical lever sensitivity, of the probe. The deflection sensitivity

Table 2.1: Typical settings and parameters used in tapping-mode scanning for collection of topography images.

Parameter	Value
Spring constant	20–30 N/m
Deflection sensitivity	58–75 nm/V
Tip radius	18–32 nm
Free amplitude	280–290 mV
Resonance frequency	250–350 kHz
Set point	150–210 mV
Integral gain	0.7–2
Proportional gain	5

was calibrated by performing an indentation experiment against a rigid silicon wafer and fitting the slope of the force-distance curve that results. The spring constant is often calibrated by non-contact methods such as the thermal tune method [86] or the Sader method [87]; however, these methods produced unreliable results with the present tapping mode cantilevers, possibly due to their high stiffness and low aspect ratios (≈ 3) compared with the more commonly calibrated contact mode probes. Instead, the spring constant calibration was calibrated by performing an indentation experiment on a pre-calibrated reference cantilever of known stiffness (CLFC-NOBO, Veeco Instruments, Plainview, NY). The stiffness of the cantilever to be calibrated was then determined using a model of springs in series. Every AFM probe calibrated for use in this study was calibrated using the same reference cantilever. Any error in the calibration of that cantilever will systematically affect all data by the same scaling factor and can thus be neglected for the purposes of comparison. Repeated calibration experiments show that the reference cantilever method produces repeatable results with less than 20% error. To further reduce calibration error, wherever possible, the same AFM probe was used for any set of experiments for which the results were to be compared directly.

The calibrated spring constant for the reference cantilever is given at the end of the cantilever. In practice, it is nearly impossible to perform an indent precisely at the end of the reference cantilever. Instead, calibrations are performed at multiple points along

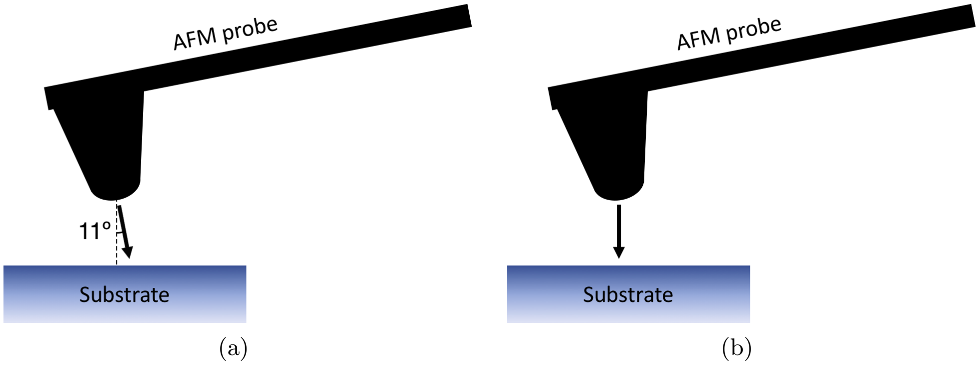

Figure 2.4: Two directions of approach for the AFM cantilever: (a) in the direction normal to the cantilever axis, as used for nanoindentation experiments, and (b) in the direction normal to the substrate, as used for spring constant calibration.

the axis of the cantilever. Given that the reference cantilever has a known length L, the apparent spring constant at a given location ΔL away from the end can be evaluated using the relationship [88]:

$$k_{s,\text{apparent}} = k_{\text{test}} \left(\frac{L}{L - \Delta L} \right)^3 . \tag{2.2}$$

In practice, the location ΔL cannot be determined exactly at a single point, so seven or more indentation experiments were performed at 5 μm intervals along the length of the reference cantilever, and the results were fit with a cubic polynomial to produce an accurate value for the spring constant of the cantilever to be calibrated. The distance ΔL can also be evaluated as a fitting parameter. Although it is not useful as an experimental result, it can be visually correlated with the image of the AFM cantilevers viewed via the optical microscope, and used as a check to verify that the fit is reasonable.

By design, the AFM cantilever and chip are mounted into the microscope so that the cantilever is at an 11° angle relative to the substrate surface, as illustrated schematically in Figure 2.4. In order to reduce sliding between the tip and the surface when the indentation is performed, and also to reduce buckling in the cantilever, all indentation experiments are performed by advancing the tip at an angle that is 11° to vertical, that is, perpendicular to the axis of the cantilever as shown in Figure 2.4a. Altering the angle of approach of the cantilever also alters its effective spring constant in the direction of approach [89, 90], so the spring constant $k_{s,probe}$ is adjusted by the appropriate factor of $1/\cos^2(11°)$ [90]. Note that this so-called tilt correction was not implemented when performing the calibration against the reference cantilever. Instead, the AFM probe was advanced toward the surface vertically as shown in Figure 2.4b. This approach direction is appropriate for calibration because the reference cantilever is calibrated in the normal direction and its surface is smooth flat, so sliding and buckling were not a concern.[2]

The AFM probes are imaged using transmission electron microscopy as shown in Figure 2.5a. A custom probe holder was used for imaging [91]; this holder guaranteed consistent alignment of the AFM probe relative to the electron beam, allowing probes to be imaged before and after experiments in the same orientations. The radius was measured by manually selecting points around the end of the probe, and fitting a circle to these points. All AFM probes were imaged in this fashion, and from the images their radii were measured, before and after every nanoindentation experiment to verify that the probes were not damaged. If the probe was fractured or no longer round, the data were discarded.

2.3. Atomic force microscopy-based nanoindentation

Mechanical properties of the nanoparticle packings were evaluated using nanoindentation performed using atomic force microscopy. Mechanical properties were determined quantitatively from the force-displacement curves using custom algorithms written in MATLAB (MathWorks, Natick, MA). The reduced modulus (of the probe and sample) was determined as

$$E_r = \frac{S\sqrt{\pi}}{2\beta\sqrt{A}} \tag{2.3}$$

where S is the slope of the retract curve as the unloading process begins, depicted in Figure

---

[2] For this reason, the correction factor $1/\cos^2(11°)$ is the reciprocal of that reported in Hutter *et al.*: the calibration was performed normal to the substrate and the indentation performed normal to the cantilever axis. Customarily, AFM probes are calibrated normal to their axes using a technique such as the Sader method [87], and then advanced vertically toward the sample, the opposite of what is done here.

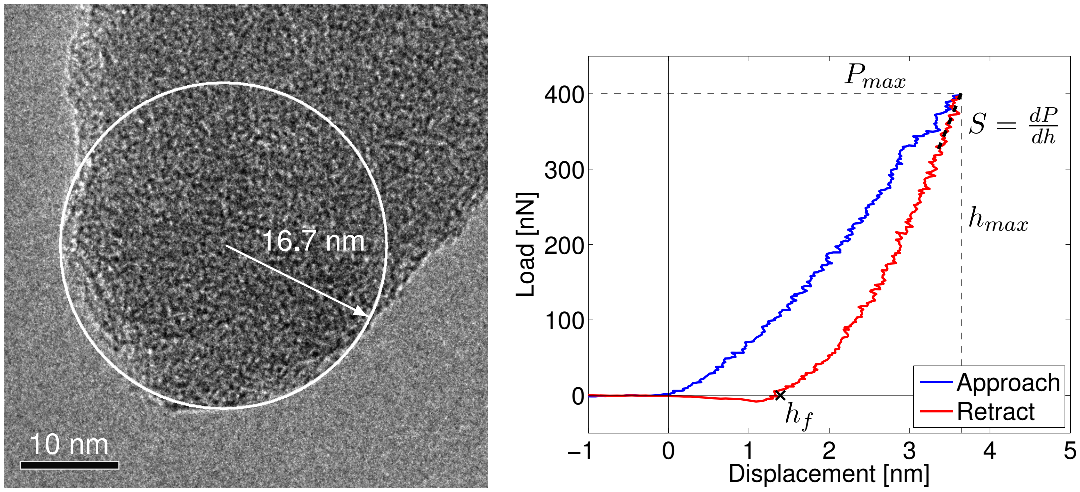

(a) (b)

Figure 2.5: (a) A transmission electron micrograph of one of the AFM probe tips used in this study. The best-fit circle to the tip geometry is indicated in white, and has radius 16.7 nm. (b) An example force curve, showing an indentation on a 105 nm thick SiO_2 nanoparticle film. Figure adapted with permission from [6].

2.5b, β is a fitting constant, which was taken to be unity following the procedure in Oliver and Pharr (2004), and A is the contact area, evaluated using a spherical area function for a probe of known radius R, evaluated using TEM (Fig. 2.5a) as discussed in Section 2.2. This radius was used to compute the spherical area function used in the measurement of hardness and elastic modulus. The probe was also imaged after scanning, verifying that it was not damaged. The area function was evaluated at a depth $h_{\mathrm{max}} - \epsilon P_{\mathrm{max}}/S$, where $\epsilon = 0.75$ following the procedure in References [83, 84] and P_{max}, S, and h_{max} are defined as shown in Figure 2.5b. The plane-strain modulus of the system as defined in Equation 2.3 is a reduced modulus which is a function of the moduli of the materials in contact:

$$\frac{1}{E_r} = \frac{1-\nu_s^2}{E_s} + \frac{1-\nu_p^2}{E_p}, \tag{2.4}$$

where E_s, ν_s, E_p, and ν_p are the Young's modulus and Poisson's ratio of the sample and probe, respectively [83, 84]. The Poisson's ratio is not known for the present disordered nanoparticle packings, and is likely to vary spatially depending on the local structure and packing density. Therefore, the Young's modulus cannot be evaluated directly and the effective modulus of the sample $E_{\text{eff}} = E_s/(1-\nu_s^2)$ will be reported in Chapter 3.

The hardness of the sample was evaluated using the equation

$$H = \frac{P_{\max}}{A}, \tag{2.5}$$

where $P_{\max}$ and A are as defined previously [83, 84].

It must be emphasized that the common methods for analyzing nanoindentation experiments assume that the indenter forms a shallow indent with the surface. Conventional nanoindentation is frequently performed with a Berkovich tip, which has a half-angle of 70.3° [84] and therefore an ideal indenter forms a 19.3° angle with a flat substrate. The same equations are also consistent for rigid spherical indenters [84], and they recover the equations of the Hertz contact model for contact between spheres [92] with an appropriate choice of area function. The Hertz contact model assumes small deformation, so its formulation also precludes indentation where the indentation depth is large compared to the indenter radius. If the indentation depth is very large compared to the radius, the scenario might be viewed as more closely resembling a pin or knife inserted into the material rather than as a compression experiment. The majority of the deformation is then in the lateral direction, rather than normal compression, and the assumptions made in evaluating the modulus are not appropriate.

In portions of the present work, indentation depths were as low as a few nanometers, which is significantly less than the tip radius (15-30 nm) and small enough that the assumption described in the previous paragraph is valid. In other portions, significantly greater indentation depths of greater than 50 nm are observed, and the assumption is no longer valid. Therefore, in Chapter 3 the elastic modulus and hardness will be reported in keeping with the methods of Oliver and Pharr, whereas in Chapter 4 the stiffness S and indentation depth $h_{\max}$ will be reported instead. In Chapter 6, both sets of parameters will be reported as they are applicable.

Notes

A portion of Section 2.3 appears in print: Adapted with permission from Joel A Lefever, Tevis D B Jacobs, Qizhan Tam, Jyo Lyn Hor, Yun-Ru Huang, Daeyeon Lee, and Robert W Carpick. Heterogeneity in the small-scale deformation behavior of disordered nanoparticle packings. Nano Letters, 16(4):2455-2462, 2016. Copyright (2016) American Chemical Society.

CHAPTER 3 : Heterogeneity in the deformation mechanical response of spin-coated silica nanoparticles

It is desirable to apply the findings of prior research on various disordered materials to disordered nanoparticle packings, and conversely to apply the results discussed here to the broader picture of understanding disordered materials. However, before this logical jump can be made, it must first be demonstrated that these disordered nanoparticle packings exhibit similarities with other disordered materials. In addition, to facilitate commercial use of disordered nanoparticle packings, their mechanical properties must first be fully understood. This chapter will demonstrate that that spin-coated, disordered silica nanoparticle packings exhibit substantial mechanical heterogeneity: strong and weak areas are identified in terms of hardness and elastic modulus, and we propose that the low strength regions are associated with the presence of soft spots discussed previously in Section 1.1.3. In addition, certain fundamental mechanical properties, including the elastic modulus and hardness, will be measured at the single constituent level. This material also exhibits compaction effects, and the particle bond strength increases over time. All of these behaviors must be understood in order to make use of this material system in applications or as a model.

Recently the mechanical properties of disordered nanoparticle films have been characterized using conventional indentation techniques, demonstrating that they exhibit properties of both granular and viscoplastic materials [93]. For example, nanoindentation revealed that atomic layer deposition may be used to strengthen nanoparticle packings [94, 95]. Nanoindentation experiments also showed that particle shape anisotropy causes an increase in toughness and a reduction in the stiffness of nanoparticle packings [79]. However, the fundamental deformation and failure mechanisms of nanoparticle packings due to external stress, such as resulting from nanoindentation, have not yet been determined.

In the present chapter, nanoindentation was performed on nanoparticle packings using atomic force microscopy (AFM) [6]. With its nanometer-scale spatial resolution, AFM is able to probe the mechanical heterogeneities hypothesized to occur in amorphous materials. Since soft spots are favorable at free surfaces [41], there is an increased likelihood of finding them with AFM-based mechanical measurements that probe the surface of the nanoparticle packing. It is proposed that those nanoparticles having a strong mechanical connection via a force chain to the substrate [96] can be identified with AFM nanoindentation.

3.1. Experimentally probing the sizes of rearrangements and the elastic properties of spin-coated silica nanoparticle films

AFM-based nanoindentation experiments performed on nanoparticle films often cause plastic deformation by moving particles. Experiments were performed by driving the base of the cantilever at a constant velocity until a predetermined maximum load was reached. This maximum load ranged between 100 and 800 nN. A more complete description of the nanoindentation procedure is provided in Section 2.3. In order to perform these experiments, it was necessary to determine that the region in which the experiments are to be performed is suitable for nanoindentation.

Amplitude modulation AFM topographic imaging was used to characterize the surface of the film, confirming that it is flat and free of contamination. A typical topography scan is shown in Figure 3.1a, where the entire 500 nm × 500 nm scan has a root-mean-square (RMS) roughness of 2.23 nm, or 2.11 nm after line-by-line flattening has been applied. Over a collection of ten 500 nm scans, the RMS roughness was 2.97 ± 0.30 nm, or 2.41 ± 0.21 nm with line-by-line flattening. This is well below the particle diameter of 20.0 ± 4.8 nm, indicating an extremely smooth film. The RMS roughness is affected by imaging artifacts resulting from tip convolution, which tend to reduce the measured roughness below that of a particle radius [97]. However, the low roughness over an area that is large compared to the particle size indicates that the film topography is generally uniform, with no substantial relief or variance in thickness. The roughness that is observed is due to the curved topography of the particles themselves. This shape effect may be compared with ångström-scale roughness and atomic corrugation in conventional materials [98].

Topography scans obtained using tapping mode AFM before and after performing indents are used to estimate the affected volume of a single indentation. Figure 3.1a shows

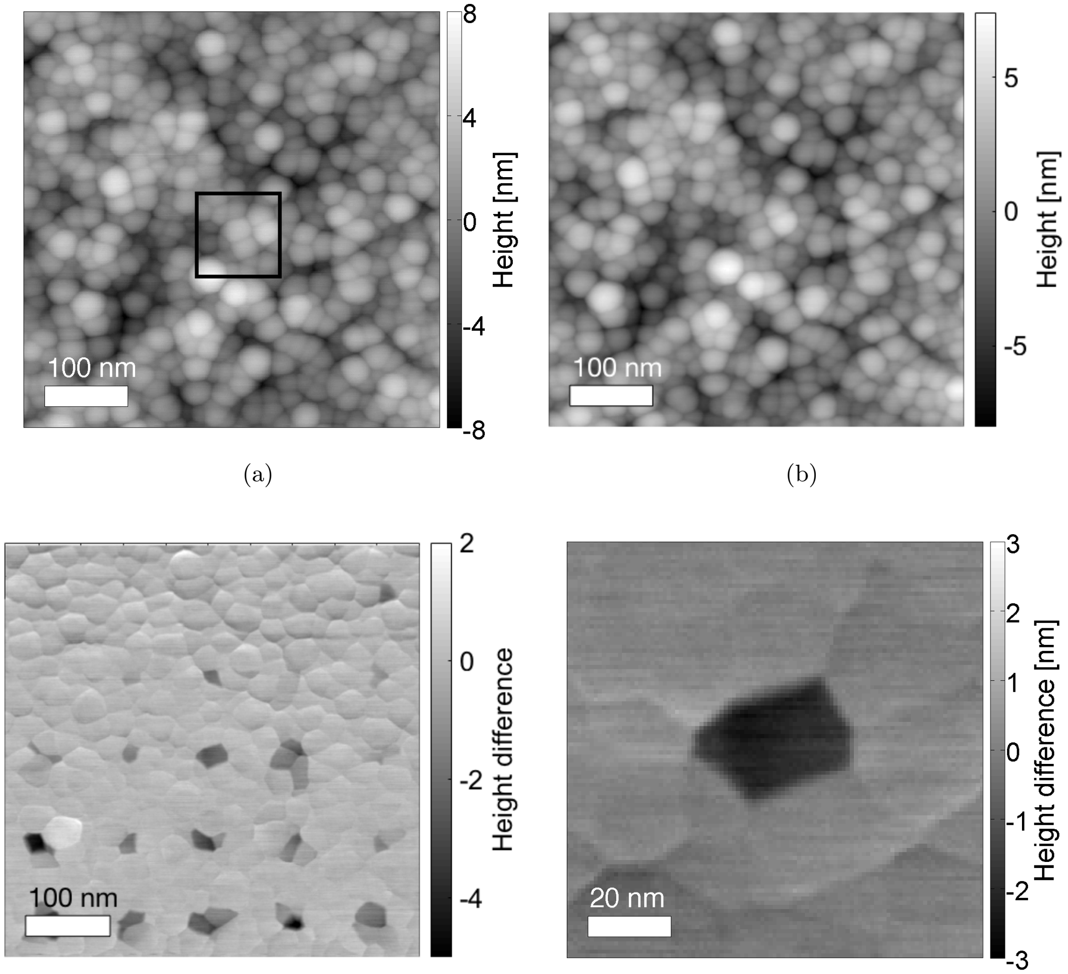
100 nm
8
4
0
-4
-8
Height [nm]
100 nm
5
0
-5
Height [nm]
100 nm
2
0
-2
-4
Height difference
20 nm
3
2
1
0
-1
-2
-3
Height difference [nm]

(a)

(b)

(c)

(d)

Figure 3.1: Topography of a film of silica nanoparticles taken using tapping-mode AFM (a) before and (b) after performing indentations. (c) A difference image, created by carefully aligning images (a) and (b) to correct for drift, and subtracting them. (d) A subset of the center of the difference image between the before and after scans (black square in (a)). The disturbed region limited to a single particle size, approximately 20 nm × 20 nm. Figure adapted with permission from [6].

a topography scan taken before a series of indents. The post-indent topography scan (Fig. 3.1b) is visually difficult to distinguish from the pre-indent scan. However, there is a measurable post-indent (plastic) displacement. To facilitate the subtraction of pre- and post-indent scans to determine this displacement, the pre- and post-indent scans are correlated together using a custom image-correlating drift-correction routine. Figure 3.1c shows the result of subtracting the pre-indent topography scan from the post-indent topography scan. Figure 3.1d is a subset of Figure 3.1c, showing that the affected region is clearly evident and localized to a single particle. This demonstrates the high spatial resolution of this technique. The slight shading of the surrounding particles indicates a small mismatch in the correlation of the scans, which nonetheless is usually less than one nanometer. Moreover, it shows that the plastic deformation at the surface is confined to the extreme limit of a single particle. Consistently across hundreds of indent sites, the affected region is typically only one to three particles, as shown by example in Figure 3.1c.

The effective elastic moduli of the films ($E_s/(1-\nu_s^2)$), as measured using AFM nanoindentation, are plotted against total indentation depth in Figure 3.2. Each data point is calculated from single unique indentation at a unique location. The considerable spread in the measured values of modulus and hardness indicates local variations in the film structure (the root mean square of the modulus values can be up to 40% of the mean value across a given sample). When a similar investigation was performed on homogeneous poly(methyl methacrylate), no such variation was observed. The accessible range of depths using AFM nanoindentation is from zero to 20 nanometers. The insets for each plot show the effective modulus values normalized by the load P_{max}, which collapses the power law fit to a single line. The uniformity of the data is readily apparent, demonstrating that all of the scatter can be attributed to a single structural degree of freedom in addition to the pre-selected applied load. This degree of freedom likely corresponds to the softness or stiffness of the measured region. In addition, the fact that the form of the curve is uniform suggests that the mechanism of yielding is the same regardless of the applied load or stress.

The size of the error bars is determined from uncertainty in the determination of tip

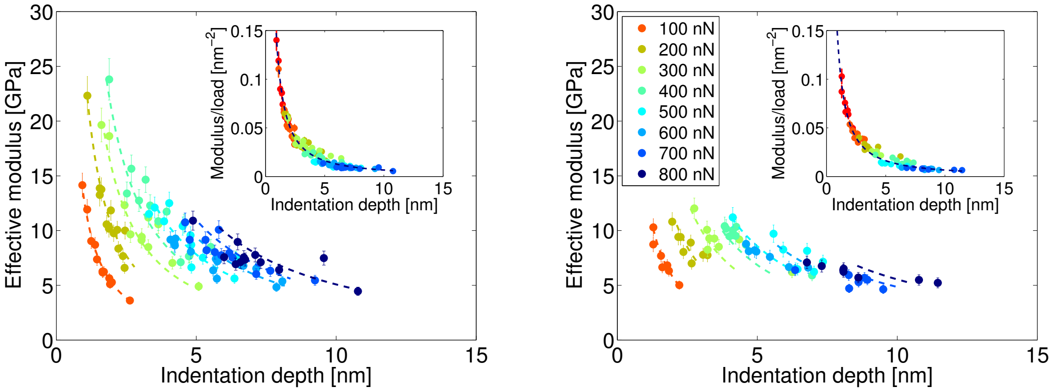

(a) (b)

Figure 3.2: Effective modulus as a function of depth for silica nanoparticle films with thicknesses of 105 nm (a) and 431 nm (b), determined using AFM nanoindentation with various maximum loads P_{max} as shown in the legend. The fits are best fits to $E_{eff} = K_E P_{max}/h_{max}^m$, where K_E and m are fitting parameters. The values of these parameters are presented in Table 3.1. The insets depict the modulus values normalized by P_{max}, demonstrating how all datapoints collapse onto a single curve. Figure reproduced with permission from [6].

radius, which becomes slightly blunted in the course of indentations. The limits of the error bars represent the modulus as evaluated using the tip radius from TEM images before versus after the indentation session. For example, the tip shown in Figure 2.5a had an initial radius of 20.6 nm, and it was measured to be 21.4 nm after a series of 128 indentations. All of the probes used in this study had radii between 16 and 39 nm, and any change in their shapes was recorded. This is believed to be the greatest source of uncertainty in the study, and its effect is always less than 8% for modulus, and 16% for hardness. This experimental uncertainty is distinct from the spread in the data, with the latter being a real characteristic of the mechanical properties of the film. The combined effects of both the uncertainty and spread in the data are indicated in the range of moduli given in Table 3.1.

Films were studied at ages between four days and six months from synthesis. The effect of age on mechanical properties will be discussed later, but for consistency all data shown in Figure 3.2 and Table 3.1 were collected four days after synthesis with the same AFM probe.

The variation in the values of effective modulus is much greater for a thin film of 105 nm

Table 3.1: Experimentally-determined values of effective modulus and the best-fit power laws depicted in Figure 3.2. Displacement for the power law fit is assumed to be nanometers.

Film thickness	E_{eff} [GPa]	Power-law fit	H [GPa]
105 nm	9.3 ± 3.6	$E_{eff} = 0.127 P_{max}/(h_{\max})^{1.301}$	1.03 ± 0.51
431 nm	7.8 ± 1.9	$E_{eff} = 0.141 P_{max}/(h_{\max})^{1.307}$	0.71 ± 0.24

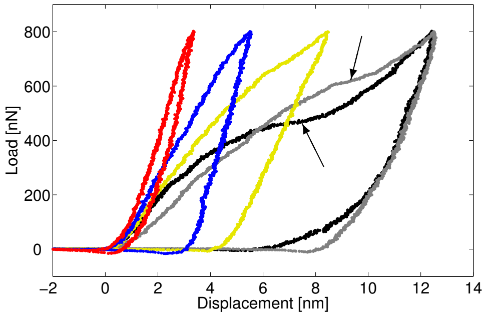

Figure 3.3: Several force curves to a fixed load of 800 nN representing AFM nanoindentations on various locations on a nanoparticle film, showing the significant variability in curve shape and indent depth. Inflection points characteristic of rearrangements are indicated with arrows in the deepest indents. Figure reproduced with permission from [6].

(Fig. 3.2a) than for a film with 431 nm thickness (Fig. 3.2b). The effect of film depth on the variance of the effective modulus (shown in Table 3.1) indicates that the effective modulus is related to film depth—meaning that in the thinner film, “strong” and “weak” spots exist. The difference between these strong and weak spots is due in part to how well particles at the surface can communicate mechanically with the rigid substrate. It is worth emphasizing that each indent is performed to a fixed maximum load, so the range of moduli and indentation depths indicate the degree to which the film is locally strong or weak.

A consistent trend in the data was the significant spatial variation of local modulus. This effect was not present on homogenous, monolithic reference samples such as rigid silicon and poly(methyl methacrylate). Conventional nanoindentation with a Berkovich indenter was also performed, and this substantial variance was not observed: in conventional nanoindentation, the sampled region is significantly larger, representing an average of tens or hundreds of particles. These regions with lower modulus presumably correspond to preexisting soft spots found at the free surface. Soft spots have already been witnessed to be enhanced in their population at free surfaces in simulations of harmonic spring-connected spheres [41]. The kinks or inflection points in many of the deepest force curves (Fig. 3.3) indicate that some yielding event took place, which are attributed to rearrangements of nanoparticles in shear transformation zones. The highest values of moduli appear for values of $200 \leq P_{max} \leq 600$ nN, suggesting that the nanoparticle packing rearranges plastically at higher loads to accommodate the indenter tip. Particle motion is observed in the pre- and post-indentation scans, especially for loads above 400 nN, as seen in Figure 3.1.

The relationship between film thickness and measured modulus does not match the standard predictions for substrate effects resulting from nanoindentation on homogeneous thin films [99, 100]. Standard predictions assume that indents that are shallow compared to the film depth will have lower measured moduli but the distribution will be wider than for deeper indents [99], possibly due to surface roughness or uncertainty in the shape of the indenter's blunted end. Conversely, for these nanoparticle packings, the distribution is wider for thinner films as seen in Table 3.1. The lower end of the modulus distribution is comparable for both 105 nm and 431 nm films, indicating that "weak" regions are mechanically disconnected from the substrate and independent of film thickness effects. The thinner film has an exaggerated upper bound of its modulus distribution, indicating that "hard" regions are strongly mechanically connected to the substrate, which further demonstrates the structural inhomogeneity of these films. For example, a column of five colinear particles connecting the substrate to the indenter may be mechanically stiff or hard, whereas a region where the nanoparticles are staggered in a zig-zag pattern could be soft [101, 96]. Note that these structural features do not necessarily imply that the local packing fraction is greater in the vicinity of a hard region.

The observed relationship between maximum applied load and measured modulus—wherein the loads between 200 nN and 600 nN produced the stiffest material response—was confirmed valid across 11 similar datasets with $p < 0.05$ confidence. This distribution is independent of the observed aging effects. A homogeneous, linear material should exhibit a uniform elastic modulus at every location, regardless of the load. The fact that this material exhibits both an increasing modulus trend with increasing load at low loads, and a decreasing modulus with increasing load at higher loads, indicates that at least two nonlinear deformation mechanisms must be at play. It is reasonable to deduce that the lower-load mechanism is that of jamming, as the system compacts under the load [102, 31]. The higher-load mechanism is proposed to be a yielding mechanism which softens the material under adequate stress, as mentioned previously. This deformation takes the form of particle rearrangements, and may correspond to the activation of shear transformation zones [2]. Fluid cell ellipsometry was used to measure the porosity of the films, and the packing fraction was determined to be $0.70 \leq \Phi \leq 0.81$ [82]. This range of values is significantly greater than the predicted value $\Phi \approx 0.64$ for random jammed packing of monodisperse spheres [102], but is typical of measured values for nanoparticle packings [17]. It is likely that the discrepancy between the measured value and the predicted value is due to the polydispersity of the spheres, thin alumina coating, and random error in the method. Nevertheless, the present packings are likely very close to the jamming transition, such that they jam locally when a load of $200 - 600$ nN is applied to a single particle.

The major difference between "stiff" and "soft" force curves lies in their shapes, as seen in Figure 3.3. Regions identified as "stiff" behave in a nearly hard-wall or homogeneous fashion, as shown in the red and blue curves. "Soft" regions exhibit much deeper indents. The gray and black curves both exhibit inflection points at depths of 7–10 nm, which is comparable to the particle radius. This indicates that a local, plastic rearrangement of nanoparticles has taken place, and the rearrangements can sometimes be identified in the topography scans taken before and after indents (Fig. 3.1d).

It is challenging to accurately calculate the density of soft spots in the present material. However, a rough estimate can be made from the size and depth of the indentation sites, and an estimate of the fraction of indentation sites at which rearrangements occur. From the difference topography image in Fig. S1(c), it can be estimated that rearrangements are 1–3 particles in size on the surface, and from the depth of the force curves in Figure 3.3, which is on the order of one particle radius, the depth is approximately two particles. Thus a reasonable estimate is that 4-6 particles are involved in a rearrangement in this system. If 10% of the sites are soft—again judging from the difference image and Figure 3—then the soft spot density is approximately one per 40–60 particles. This value falls within the wide range of amorphous material defect densities reported elsewhere [40, 45, 41, 58]. The value determined for the present system may be affected by the system properties, including its packing fraction which is below jamming, the threshold for softness used in this analysis, and the fact that the technique only probes particles within a few diameters of a free surface, where soft spots are known to have an enhanced population [41].

3.2. Scaling of the mechanical response of nanoparticle packings to AFM-based nanoindentation

Despite its substantial variance, the data for each film thickness can nevertheless be fit to a single power law of the form $E_{eff} = K_E P_{max}/h_{max}^m$ (Insets in Figure 3.2). In other words, a single pair of values for K_E and m fit all of the data for each film thickness (Table 3.1). This relationship was chosen based on dimensional analysis: E_{eff} and P_{max}, the only quantities with force dependence, must be linearly related, while the relationship between modulus and indentation depth may vary due to the presence of other length scales contributing to the relationship (particle radius, probe radius, and film thickness, although the latter is seen to have no effect on the power law as seen in Table 3.1) [103].

The effective modulus data fits a power law with $m \approx 1.3$, independent of the indentation depth, suggesting that the mechanisms of elastic deformation remain consistent regardless of film thickness. Among various datasets taken on multiple films with multiple probes, the value of m varied in the range $0.9 \leq m \leq 1.35$. However, the power law consistently fits the dataset with high accuracy. For example, in the experiments shown here, the 95% confidence intervals are 1.301 ± 0.062 for the 105 nm film, and 1.307 ± 0.083 for the 431 nm film. The exponent may vary as a result of varying experimental parameters such as the probe size and shape. However, within a single experiment, the value of m remains remarkably consistent, and all data shown in Figure 3.2 were collected with the same probe. For the thinner

105 nm film, several outliers with high modulus—still fitting the power law—are visible (Fig. 3.2a) which are not present in the 431 nm film. These stiffer sites only occur for values of P_{max} near the middle of the range investigated. Furthermore, the hardness is closely correlated with the modulus at each site. Typical values of $H/E_{eff} = 0.10 \pm 0.02$, which are comparable to existing data for the yield strain of a range of disordered packings (including colloidal assemblies and metallic glasses) [13] using reasonable estimates for yield stress from hardness [104]. This suggests that these nanoparticle packings also exhibit what has been proposed as a universal mode of cooperative plastic deformation in glassy systems that have the capability for finite plastic flow [13, 59].

3.3. Identifying time-dependent strengthening mechanisms in nanoparticle packings

The distributions of the effective moduli were analyzed for eleven experiments, each of which consisted of loads between 100 and 800 nN on 105 nm thick films, performed between 4 and 180 days after synthesis. Error bars indicate the standard deviation of values for a given load and age, with mean values shown by the surface. The best-fit polynomial surface in load/logarithmic time follows the relation:

$$E_{eff} = 5.22 + 0.0209 P_{max} - 2.25 \times 10^{-5} P_{max}^2 + 1.07 \ln(\text{age}) \tag{3.1}$$

with E_{eff} in GPa, P_{max} in nN, and age in days. This surface, shown in Figure 3.4, is concave down over the range of loads analyzed with confidence $p < 0.05$, further demonstrating that the highest moduli appear for loads in the middle of the range. In addition, the positive coefficient of the ln(age) term shows that the films exhibit slight stiffening with age. The sign of each term in Equation 3.1 is confirmed with confidence $p < 0.05$.

Films exhibited a small but measurable stiffening behavior as they aged from 4 to 180 days from synthesis, as shown in Equation 3.1 and Figure 3.4. This stiffening behavior may be attributed to the formation of either hydrogen bonds or oxide bridges between nanoparticles, as the surfaces of the alumina-coated particles are expected to possess a significant

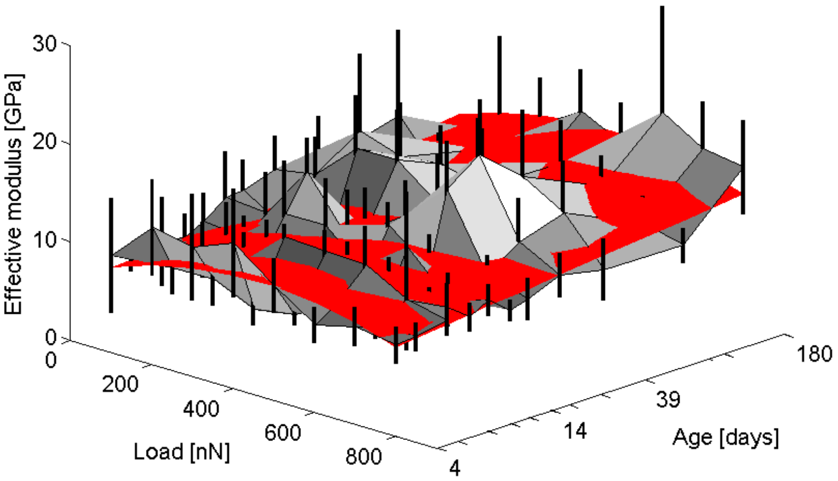

Figure 3.4: The distribution of effective moduli over time. Several probes were used in collecting the data, and each tick mark on the age axis represents an experiment that was performed. The red surface is the best fit surface from Equation 3.1. Each slice in the time axis represents a distinct experiment. The distribution of data points for every (load,time) coordinate is converted to a mean (the grayscale surface) and standard deviation (the black error bars). Some datasets were collected by Qizhan Tam under supervision of the author. Figure reproduced with permission from [6].

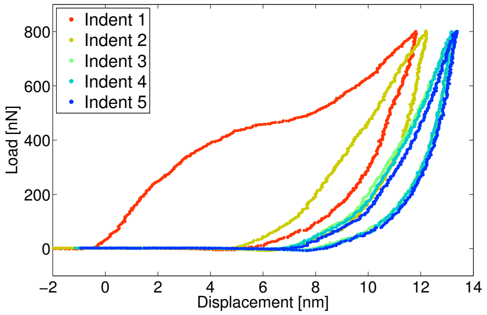

Figure 3.5: Several force curves from a repeated indentation on the same site on a spin-coated silica nanoparticle film, showing that the retract curves and subsequent approach curves do not overlap. Figure adapted with permission from [6].

density of −OH groups. Molecular dynamics simulations have previously revealed aging in silanol-terminated silica surfaces, albeit over a shorter time scale [105]. Strengthening behavior (increasing static friction) with time has been observed in friction experiments for time scales of up to days in macroscopic tests [106], and over shorter time scales (seconds) in nanoscale single asperity contact tests [107]. These nanoparticles are coated with alumina. It is hypothesized that Al−O−Al bridges form over time, which makes the particles more strongly bound.

3.4. Demonstrating how compaction stiffens the nanoparticle packing

Performing repeated indentations at the same location allows the effects of elastic and plastic deformation to be separated. Representative samples of a series of five indents per site between 400 nN and 800 nN, are shown in Figure 3.5. The measured elastic modulus, dissipated energy, total deformation, and recovered elastic deformation ($h_{max} - h_f$, with h_f defined as shown in Figure 2.5b) are plotted in order for each set of five consecutive indents in Figure 3.6. Each is normalized by the value of the respective parameter on the first indent. (The contact area for all indents was assumed to be equal to that of the first indent. This assumption is necessary because the sample deforms plastically to match the shape of the indenter during the unloading of the first indent, preventing a reasonable evaluation for successive indents. Note that with this assumption, and with load fixed, the hardness

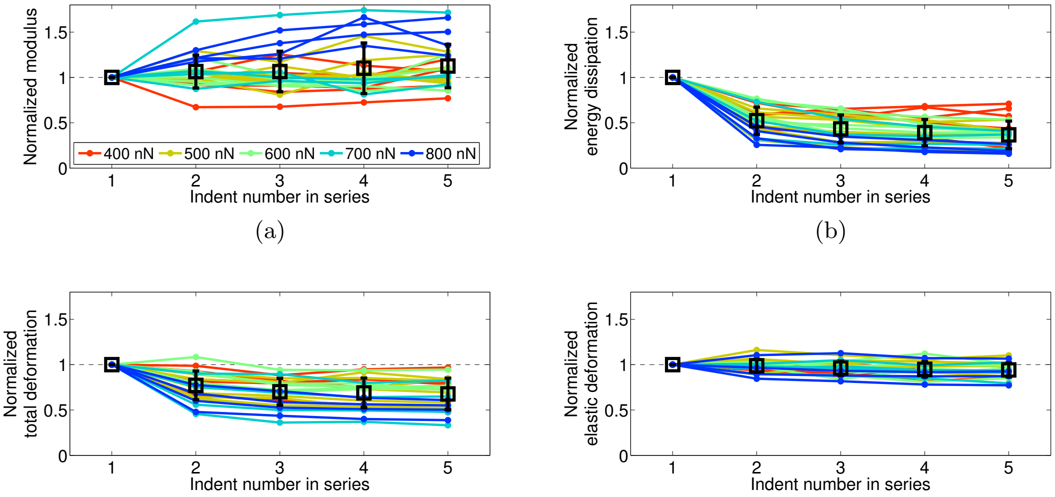

(a) (b)

(c) (d)

Figure 3.6: (a) Modulus, (b) energy dissipation, (c) total deformation, and (d) recovered (elastic) deformation for consecutive indents on the same location, normalized to the value for the initial indent. Lines connect datapoints corresponding to the same location and set of indents. The stiffness increases slightly with compaction, while the energy dissipation and deformation—all measures of plasticity—decrease. Figure reproduced with permission from [6].

$H = P_{max}/A$ remains constant by definition.)

Figure 3.6 reveals that the dissipated energy is generally highest on the first indent and reduces significantly with successive indents. This energy is proposed to be dissipated through friction between moving particles, indicating that the film rearranges to a more stable configuration under the applied force and retains that position after reloading. The total deformation is seen to decrease almost monotonically for all indents, while the recovered deformation varies nearly randomly. The total deformation is affected by plasticity, and thus is greatest on the first indent, while the recovered deformation reflects only the elastic response from the unload and is relatively unaffected by reloading. This demonstrates that the mechanisms at play are related to particle motion rather than other effects, such as plastic deformation of the tip or particle. The measured elastic modulus (Fig. 3.6a) increases somewhat with reloading (but with significant scatter). This stiffening may be related to compaction of the film. However, because the elastic indentation depth remains relatively constant after the first indent (Fig. 3.6d), it is not expected that the modulus should change significantly.

The behavior observed in Figure 3.5 is not expected for an ideal elastoplastic material. For such a material, if the indenter is reloaded, the reloading portion of the force curve for the subsequent indent should exactly match the withdrawal portion of the previous one [83]. Here the curves do not overlap (Fig. 3.5). This indicates some energy dissipation mechanism which is at play during the retraction and reloading. This is plausibly due to interparticle friction, as has been witnessed previously in nanoindentation on nanoparticle packings [79]. This also explains why the energy dissipation does not drop all the way to zero in Figure 3.6b, as would otherwise be expected. This type of interparticle friction has been observed in granular packings at larger scales [108, 96]. Further study into the nature of adhesion and friction between the nanoparticles is warranted. A means of tuning the attractive forces between particles by adjusting the ambient relative humidity will be discussed in Chapter 4. Friction is harder to adjust in an experiment, but one option to further investigate the effects of friction is to turn to computational simulations as follows.

3.5. Mechanical response of a simulated disordered nanoparticle packing

A collaborator[3] has demonstrated that the heterogeneity observed in the present material system can also be observed in simulation. The simulation made use of a molecular dynamics framework (LAMMPS, Sandia National Labs, Albuquerque, NM) to represent a disordered packing in which the system parameters were matched as closely as possible to those of the present material system. The mechanical properties were taken to be those of amorphous silica: $E = 73$ GPa, and $\nu = 0.17$ [109]. The work of adhesion was taken to be 383.6 mJ/m^2, which was a sevenfold increase over the value measured experimentally, and the equilibrium separation distance was chosen to be 0.165 nm [98]. The concession of an unusually high work of adhesion was necessary in order to produce a stable packing.

Particle contacts were initially modeled using finite element analysis, with interparticle

---

[3] Xiaohui Liu, Shanghai Jiao Tong University, with help from Ju Li, Massachusetts Institute of Technology

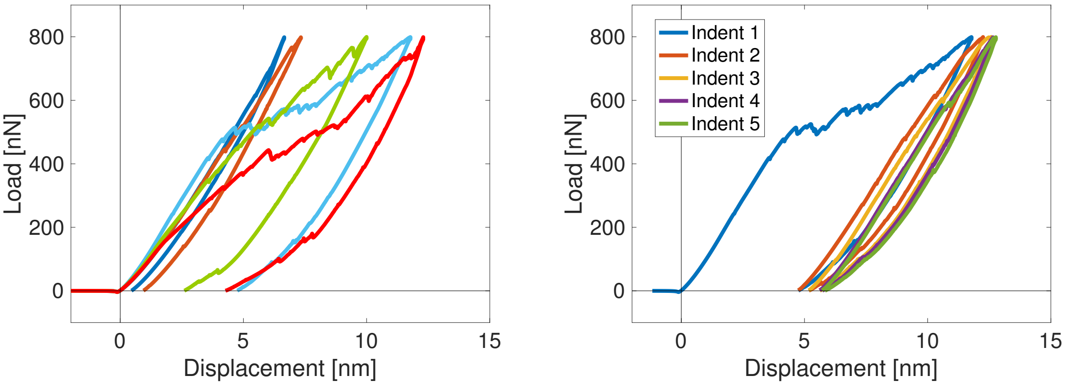

(a) (b)

Figure 3.7: (a) Force-distance curves performed in various places on a simulated disordered granular packing. System parameters were tuned to match the parameters of the system investigated in this chapter, with the exception of the adhesion force which was set to five times the estimated value for the present films. The various indentation experiments result in a variety of indentation depths. (b) Force curves representing a series of simulated indentation experiments performed in the same location. Unpublished results reproduced with permission from Xiaohui Liu, Shanghai Jiao Tong University.

forces modeled using a combination of conventional linear elastic mechanics (which may be modeled using Hertz contact theory [92]) and van der Waals interactions, which were modeled in the finite element model using a Lennard-Jones potential function. The finite element results were then used to develop a suitable potential function for the spherical contacts, which was derived using the functional form of the Derjaguin-Müller-Toporov model for adhesive contact [110]. The coefficient of friction between particles was 0.25. The simulation box was approximately $380 \times 380 \times 110$ nm^3 with periodic boundary conditions on all sides, and a rigid layer of particles on the bottom. The polydispersity of particle sizes was chosen to be 20.0 ± 4.8 nm, which matches that of the LUDOX CL nanoparticles used in this study. The top surface was indented by a spherical particle with size and mechanical properties chosen to match the AFM probe tip.

These simulations were able to reproduce several of the significant experimental results discussed in this chapter. Most notably, the substantial heterogeneity in the mechanical response was evident, as shown in Figure 3.7a. This variation in response may be compared with Figure 3.3. In addition, the range of indentation depths is comparable with that found experimentally. The simulations also demonstrated a similar mechanical response to repeated nanoindentation, with substantial hysteresis in the first indent and less hysteresis in subsequent indents, as shown in Figure 3.7b. This matches favorably with the similar experiment depicted in Figure 3.5. The overlap between successive indents is greater in the simulations than the experiments, which is likely due to the artificially high adhesion force. Friction is the primary dissipative mechanism in these materials. Friction is also the cause to which the hysteresis in Figure 3.5 may be attributed: energy is lost due to sliding friction between particles. In the present system, the increased adhesion likely increases the friction forces, reducing the amount of sliding and leading to better overlap between the retract portion of one indent and the approach portion of the subsequent. Because simulations can successfully replicate many of the salient features of these experiments, it is reasonable to use computational models to investigate the effects of tuning various parameters of the present material system, which represents an opportunity for continued exploration.

3.6. Concluding remarks

This study provides unprecedented measurement of the mechanical properties of a disordered nanoparticle packing resolved at the level of the single constituent particles. This permits loads to be applied to individual particles, and both their local motions (and those of their neighbors) and their mechanical responses may be observed. This has not previously been accomplished in a disordered system at this length scale, where the effects of adhesion between the constituent particles are still relevant.

These films are mechanically inhomogeneous, and the measured effective elastic modulus varies by up to 80% at different locations. However, despite this large spread, the elastic modulus has a clear power-law dependence on maximum load and depth at all locations. The observed displacements at the single particle level combined with the measured force-displacement response supports a picture where plasticity is related to rearrangements of a few particles, in accordance with the stress-driven shear transformation zone theory in amorphous materials. The observed failure strain is consistent with that observed for other disordered packings. This response is markedly distinct from that expected for crystalline arrangements which accommodate flow via dislocation motion. Similar behavior can also be observed in simulations of disordered nanoparticle packings, which hold promise for further in-depth study of these phenomena.

These results are potentially useful in the design of nanoparticle coatings, especially those with applications that involve mechanical aspects or where structural integrity and durability are needed. The results may also assist in the ongoing search for toughening mechanisms of disordered packings. Specifically, because plasticity likely originates at soft spots, it is expected that they contribute to ductility. Therefore, materials designed using processing routes which enhance the sizes or concentrations of soft spots may be less susceptible to fracture.

Atomic force microscopy has also demonstrated mechanical heterogeneity in metallic glass [39], lending credence to the idea that nanoparticle films are effective analogs for atomic glasses. This is especially true for those amorphous materials with isotropic bonding configurations, such as metallic glasses, colloidal suspensions, and granular packings, particularly those that are bound by adhesive forces between the particles. The spatial variability of mechanical properties demonstrated here, and their structural dependence, are potentially exhibited in many of these systems as well.

Notes

A significant portion of this chapter appears in print: Adapted with permission from Joel A Lefever, Tevis D B Jacobs, Qizhan Tam, Jyo Lyn Hor, Yun-Ru Huang, Daeyeon Lee, and Robert W Carpick. Heterogeneity in the small-scale deformation behavior of disordered nanoparticle packings. Nano Letters, 16(4):2455-2462, 2016. Copyright (2016) American Chemical Society.

CHAPTER 4 : Humidity affects the mechanical response of loosely packed two-component nanoparticle packings

Disordered nanoparticle packings have been proposed for optical coatings [82] and sensors [21, 22], among other applications. In many of these applications, the device is exposed to the elements. The response of granular materials is known to be affected by the environmental conditions [7, 111]. The ambient humidity can alter the strength of interparticle bonds in disordered nanoparticle packings by changing the capillary shape [112]. Similarly, in large-scale granular materials, the shape of the capillary bridges affects the strength of the resultant packing. For example, a sand castle can be built from damp sand, but either an excess or total lack of water will cause the castle to collapse [98]. Although it is well known that capillary shape qualitatively alters the mechanical properties of disordered granular materials, the effect of humidity on the mechanical strength of nanoparticle packings is not understood. Therefore, it is also important to investigate how the plasticity of the film is affected by environmental conditions [13]. In this chapter, it will be demonstrated that increasing the relative humidity inside the AFM chamber causes capillaries to condense in the nanoparticle packing, and that the capillary bridges affect the mechanical response of the material. This information is useful in the design of commercial devices. Moreover, this information also helps to facilitate the use of disordered nanoparticle packings as a model system for other disordered materials.

4.1. Previous investigations of capillary effects in granular materials

Substantial prior research has focused on the question of understanding how humidity affects the mechanical properties of granular materials. In one previous study, an increase in humidity was seen to result in enhanced stiffness and hardness of a silica nanoparticle superlattice [113]. However, the relative humidities that were explored were relatively dry ($\leq 35\%$), and controlled indirectly via temperature. In experiments on polystyrene disordered colloidal packings, an increase in relative humidity was found to increase the total energy dissipated upon compression, which suggests that humidity enhances plastic deformation [13]. Molecular dynamics simulations have also demonstrated the strength of capillary forces between a pair of spherical silica nanoparticles [112]. This study demonstrated that the forces exerted by capillary bridges are weakest at relative humidity levels above 80% and below 10%; the forces are greatest in the intermediate range. In addition, at high humidity levels, the range over which the capillary force can act is increased, because the maximum length of a capillary bridge is greater than at low humidity levels [112].

Simulations have extended the analysis of capillary-mediated interactions to two-dimensional disordered granular packings [111], and found that the maximum force that can be sustained by the capillary varies nonmonotonically with water content. However, the effect of relative humidity on the deformation mechanisms of a disordered nanoparticle packing has not been investigated experimentally. In addition to changing the interparticle bonding via capillary bridge formation [7], humidity may also affect the propensity to form hydrogen bonds or covalent metal oxide bonds between nanoparticles [107, 105]. As such, humidity control offers a convenient means to tune the interactions between neighboring particles, which may further enhance the use of nanoparticle packings as model systems for other types of disordered materials including metallic glasses, which are more strongly bonded due to interatomic interactions, and granular packings, which are far more weakly bonded and often purely repulsive.

This chapter will investigate the effect of humidity on the mechanical properties of two-component disordered nanoparticle packings which have been deposited using layer-by-layer deposition. This deposition technique produces films which have a lower packing fraction than those created by spin-coating. Due to the lower packing fraction, the rearrangements that occur are more prominent and more readily quantified than those observed previously in spin-coated films [6]. This chapter will demonstrate that capillary condensation alters the mechanical properties of disordered nanoparticle packings. In addition, it will examine the distribution of the sizes of the rearrangements that occur.

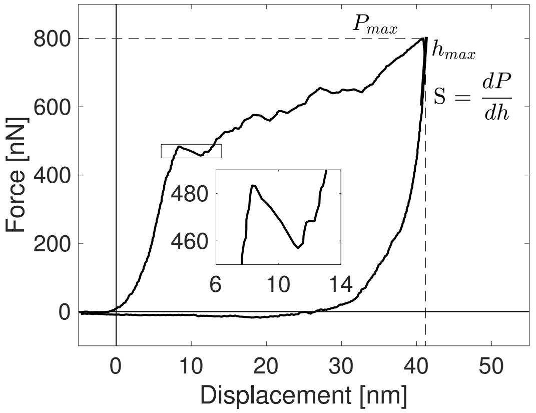

Figure 4.1: An example of a force curve with the stiffness S used in determining the modulus denoted. Several load drops are also visible as serrations in the approach portion of the curve; one is shown in the inset.

4.2. Characterizing mechanical response of layer-by-layer deposited films using nanoindentation

For this study, disordered nanoparticle packings were synthesized from aqueous solutions of anatase titania and nanodiamond, as discussed previously in Section 2.1.3, which was selected for compatibility with the TEM. This compatibility will be leveraged in Chapter 5. AFM-based nanoindentation experiments were performed using a tapping-mode AFM probe (Section 2.3). Due to the porous nature of the layer-by-layer film, the force curves that resulted from these nanoindentation experiments featured numerous load drops, as shown in Figure 4.1. These load drops indicate the occurrence of intermittent relaxation events corresponding to the rearrangement of one or more nanoparticles. This figure may be contrasted with Figure 3.3, which includes several force curves collected on a more densely-packed spin coated film. No serrations are visible in that case; instead, only smooth yielding characterized by inflection points are present.

The humidity in the AFM chamber was varied by opening the chamber to reach ambient relative humidity (RH $\approx$ 40-55%), by flooding the chamber with a supply of dry nitrogen (RH $\approx$ 0), and by placing open dishes of nearly boiling water inside the sealed chamber. These conditions facilitated access to relative humidity levels between 18% and 100%. The boiling water did not affect the temperature of the air inside the chamber by more than 2°C. A hygrometer (Fisher Scientific, Waltham, MA) was used to measure the relative humidity. Topography images were obtained in tapping mode both before and after indentation to verify that the surface was uniform and to determine the deformation of the sample due to the indentation.

To investigate the possibility of any hysteresis effects related to the formation of capillary bridges, experiments were performed first under nearly saturated conditions, and then the humidity was incrementally reduced to ambient conditions, followed by dry, ambient, and saturated conditions. No significant hysteresis in the results was seen. The data obtained at high humidity is further divided into 98% and 100% conditions, for reasons to be discussed later. With the exception of experiments performed near saturation, no systematic change was observed in measurements over 20 minutes after reaching a particular humidity level. Therefore, experiments were begun immediately after reaching the target humidity.

4.3. Environmental conditions affect the stiffness and plasticity of disordered nanoparticle packings

The mechanical properties of the sample change with the relative humidity, as can be seen in Figure 4.2. These results are numerically tabulated in Table 4.1. The stiffness decreases with an increase in humidity, while the indentation depth and energy dissipation both increase. Since plasticity is involved, the latter two effects are coupled; a greater indentation depth will necessarily result in more mechanical work.

The difference in the mechanical response of the packing under each humidity condition is demonstrated graphically in Figure 4.3. These composite force curves are produced by taking an average over all experiments: at every force value, the plotted depth represents the mean indentation depth of all measurements at that force and collected at a given humidity level.[4] The greater indentation depth at high humidity is readily evident. In addition,

---

[4] The opposite configuration, in which the indentation loads are averaged at every depth, does not facilitate a convenient comparison as indents drop out of the calculated average after reaching their maximum depth. The composite force curve becomes dominated by "soft" or weak regions at deeper indentation depths.

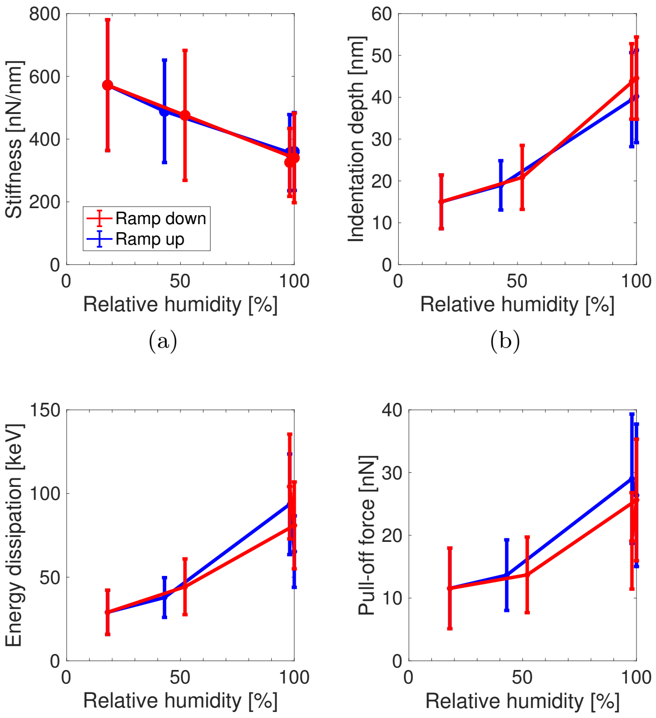

(a) (b)

(c) (d)

Figure 4.2: The measured (a) stiffness, (b) indentation depth, (c) energy dissipated, and (d) the pull-off force resulting from adhesion and capillary forces in the course of performing a nanoindentation experiment at various relative humidity levels. The error bars represent the standard deviation of the dataset; because of the very large sample sizes, the differences between the various distributions are statistically significant with $p < 0.05$ in almost all cases. The connecting lines indicate the order in which the experiments were performed. Experiments were performed by Jason Mulderrig under direct supervision by the author.

Table 4.1: Contact stiffness, indentation depth, and energy dissipation each with their standard deviations for trials in the order in which they were performed. N is the minimum number of indentation experiments evaluated at that humidity level. In some specific trials, the stiffness could not be evaluated, but the indentation depth and energy dissipation are still reported.

RH [%]	N	Stiffness [nN/nm]	Indentation depth [nm]	Energy dissipation [keV]
98	36	326 ± 108	43.8 ± 9.0	104.2 ± 31.3
100	91	340 ± 143	44.6 ± 9.8	80.9 ± 26.0
52	170	476 ± 207	20.9 ± 7.6	44.3 ± 16.7
18	195	572 ± 209	15.0 ± 6.4	29.0 ± 13.2
43	197	489 ± 163	18.9 ± 5.9	37.8 ± 11.9
98	79	357 ± 121	39.4 ± 11.2	93.6 ± 30.1
100	67	360 ± 124	40.2 ± 11.0	65.3 ± 21.4

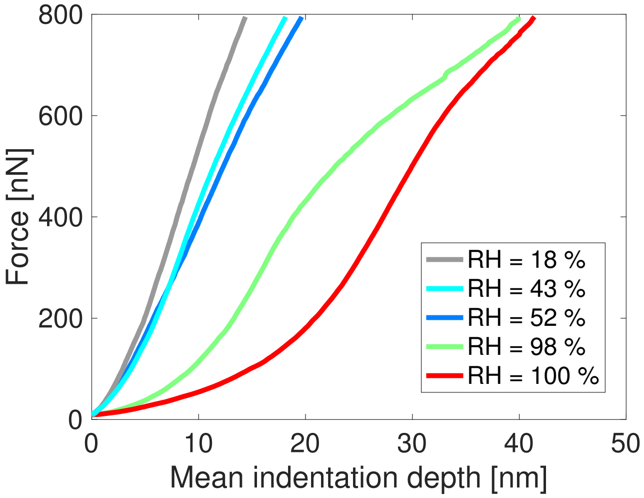

Figure 4.3: Composite force curves at each selected humidity condition. Each composite force curve represents the average depth of all force curves binned at every load between 0 and 800 nN. The greater indentation depths at high relative humidity, shown in Figure 4.2b, are shown here as well. Only the approach portion of each force curve was incorporated into the average.

a marked contrast is apparent between the shapes of the force curves collected at 98% humidity and 100% humidity: substantially more deformation occurs at low loads under the saturated condition. The difference between these two curves is particularly significant because it corresponds to only a small change of 2% relative humidity. This represents an important transition, which will be discussed further in Section 4.3.2.

The uptake of water results in a change in the shape of the menisci in the sample. These menisci are the likely reason why a film which is more compact might also be less stiff. Under very humid conditions, the meniscus transitions from a pendular to a funicular or capillary state [7]. These states represent different stages of formation of the condensed water bridges between particles, as shown in Figure 4.4. The reduction in air-liquid interfacial area reduces the capillary force resulting from surface tension. Furthermore, capillarity no longer plays a role as the particles become increasingly surrounded by condensed water, so the capillary pressure becomes uniform on all sides of each particle, while at the same time the capillary pressure comes to equilibrium with the air pressure. A similar weakening of the interparticle forces was previously observed in simulation [112], although that

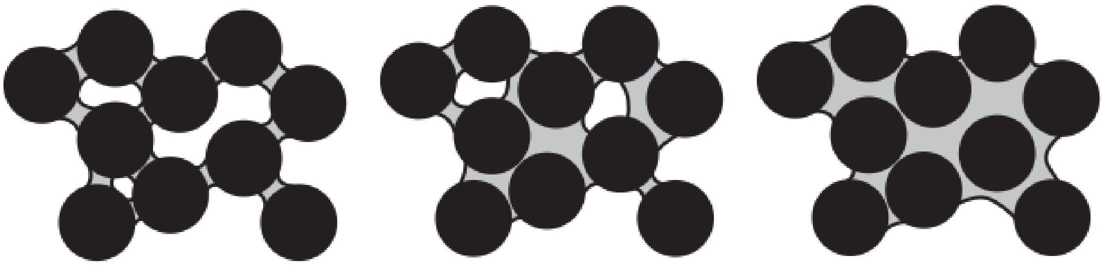

(a) (b) (c)

Figure 4.4: The structure of the condensed water bridges (gray) in a granular material (black) in the (a) pendular, (b) funicular, and (c) capillary states. Figure reproduced with permission from Ref. [7].

simulation considered only a single pair of particles. Therefore, the overall structure of a capillary bridge connecting multiple particles was not considered. The weakening of the particle-particle interactions permits the sample to deform farther under a given load, and to also have a weaker restorative force or stiffness. Due to the large sample sizes used here, the difference between the distributions of each parameter—stiffness, indentation depth, energy dissipation, and adhesion—under each set of environmental conditions is statistically significant with $p < 0.05$ in almost all cases.

The gradual increase in the pull-off force shown in Figure 4.2d demonstrates that the capillary structure between the tip and the sample is changing. The pull-off force is in part the result of a capillary bridge that forms between the tip and sample, which can be sustained to greater distances and under greater forces at high humidity because the size and surface area of the capillary increase. This trend opposes the trend of decreasing adhesion force between a pair of spheres at very high humidity predicted by Leroch and Wendland [112]. The discrepancy may be attributed to the rough topography of the nanoparticle packing; rough surfaces have been observed to exhibit greater pull-off forces at high humidity than at intermediate humidity levels [114]. It is possible to form capillary bridges with multiple particles rather than with just a single particle, and this is more likely to occur at higher humidity levels where the capillaries are generally larger. This increase in capillary size results in greater capillary force due to the increase in surface area on which surface tension can act.

Our observation of material weakening at high humidity stands in contrast with the findings of Gallego-Gómez et al. [113], in which conventional nanoindentation was performed on a film composed of a superlattice of colloidal silica. The authors of that study observed a lower elastic modulus and hardness at decreased humidities. The range of relative humidity investigated was from 0 to 35%. However, their means of varying the humidity was to vary the temperature of the substrate, assuming that by raising the temperature to above the boiling point, the water in the capillaries would evaporate. The lower modulus and hardness observed at low humidity may in fact be due to the higher temperature and greater thermal activation. In addition, their experiments were only able to reach the dry and pendular states [7] of meniscus formation because they did not supply the chamber with an extra source of water vapor, whereas the present experiments reach the funicular and capillary states.

The indentation depths are systematically greater in the results presented here than in those presented in Chapter 3, which were conducted using nominally identical probes, applying the same maximum load, on a nanoparticle packing that was produced via spin coating of silica nanoparticles [6]. Therefore, all differences between the present behavior and the behavior witnessed previously may be attributed to the different material system. This observation, as well as the fact that the indentation depth increases with humidity, may both be attributed to the load drops that are frequently visible in the force curves collected on this material system. These load drops appear as serrations in the force curve, as shown in Figure 4.1, and more load drops are seen at high humidity than at ambient or dry conditions, as seen in Figure 4.5a.

4.3.1. Load drops indicate the occurrence of intermittent rearrangement events

At every level of relative humidity investigated, the distribution of the magnitudes of all load drops is roughly exponential, as shown in Figure 4.5b. The dotted lines represent exponential fits to each dataset. The decay length for each magnitude population distribution

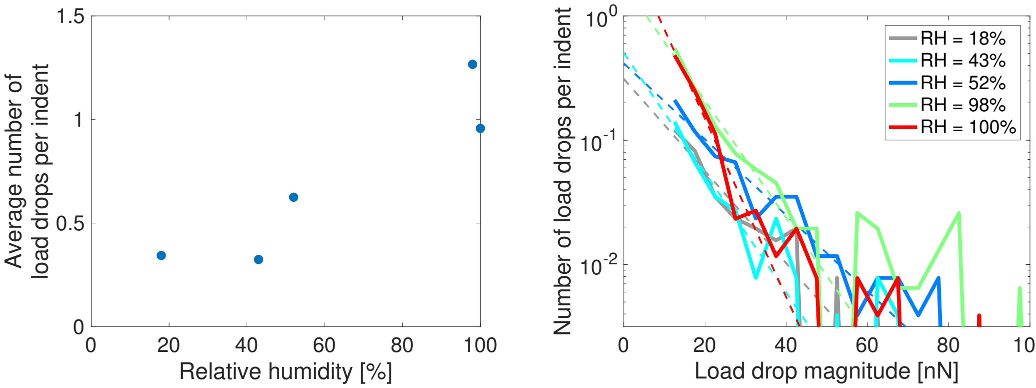

(a) (b)

Figure 4.5: (a) The average number of load drops occurring at each relative humidity condition investigated in the present study. More load drops are observed at higher humidity levels, excepting at saturation which is discussed in greater detail in Section 4.3.2 (b) Histogram of the magnitude of load drops normalized by the number of indentation experiments performed. Due to experimental challenges, the number of indentation experiments was not equal in all cases. The distribution at each humidity level is roughly exponential, as shown by the dotted lines which are fits to the data.

ranges from 9–20 nN, but this decay length has no clear, monotonic dependence on humidity. It is reasonable to assume that the decay length of the distribution is nominally the same for all datasets, and the discrepancies observed are due to variability in experimental factors. The shape of these distributions will be discussed in greater detail in Chapter 5, in the context of avalanche scaling.

The load drops observed in the layer-by-layer deposited disordered titania-nanodiamond nanoparticle packing were never observed in our prior work on spin-coated silica nanoparticles [6]. There are several important distinctions between the nanoparticle packings used in these two studies. These include the particle composition, polydispersity, deposition method, and particle geometry. Of these differences, most likely the deposition method has the largest impact, because layer-by-layer deposition of the titania-nanodiamond system results in a packing fraction that is below the random close-packed limit of 64%. The low packing fraction is in part due to the repulsive interactions between particles of the same composition. By contrast, the particle composition itself likely has minimal effect because all species investigated here and previously are hard relative to the properties of the packing as a whole. The titania and nanodiamond nanoparticles, being crystalline, have a somewhat rougher (i.e. faceted) geometry than the silica nanoparticles which are quite smooth and spherical. However, any effect related to particle roughness should strengthen the present packings when in fact a new, weakening mode of plasticity is observed. Similarly, if bidispersity had a major effect, it would be to contribute to a more densely packed film [36], which should be less conducive to sudden load-drop events. Therefore, the reduction in packing fraction is the most obvious explanation for the observed enhancement in plasticity in the layer-by-layer nanoparticle films as compared with the spin-coated films.

In layer-by-layer deposition, nanoparticles in each deposition step cannot form a dense monolayer atop an existing packing of nanoparticles due to electrostatic repulsion, and a packing fraction much lower than the random close packing limit of 64% is expected [81]. This stands in contrast to the spin-coated silica nanoparticle films [6] investigated in Chapter 3, which were expected to be very near the close-packing limit. An in-depth investigation of porosity will be conducted in Chapter 6; however, it is safe to say that the greater porosity in the present films nonetheless has a significant influence on the modes of plasticity observed here.

The transition from the smooth yielding observed on silica nanoparticle packings to the load drops observed here suggests that the mechanism of deformation is different in these two materials. Fluid-cell ellipsometry [82] and Rutherford backscattering experiments suggest that the porosity is much greater in layer-by-layer deposited films. The porosity is likely greater than 50%, although experimental difficulties prevent obtaining a precise value. As the silica nanoparticle films are nearly at the close-packing limit, their likely mode of plasticity is a cooperative rearrangement of many particles such as an STZ [2, 63], discussed previously in Section 1.1.4. In contrast, the instantaneous yielding exhibited by the porous layer-by-layer films might exhibit behavior closer to a T1 process, which is a rearrangement principally involving only a single particle moving into a region of excess free volume [48]. Because the T1 process requires this free volume, it is more likely to occur in the porous film. Then as soon as a freestanding particle breaks loose from its neighbors, the force curve exhibits a load drop due to the collapse of the void underneath. It is also possible that a more complex process is at play, such as a combination of the mechanics of a T1 process and an STZ. However, more work would be necessary to identify such a process. Simulations may be required to accomplish this task, because current experimental techniques cannot map the motion of particles in the interior of a nanoparticle packing.

4.3.2. A critical transition in behavior occurs upon reaching saturation

It is virtually impossible to maintain the humidity in the AFM chamber just below saturation for the extended duration needed to perform hundreds of indentation experiments without disturbing the apparatus. For this reason, the data collected at high humidity are divided into two categories. The data collected before reaching saturation is labeled as "98%" in the figures and tables, and the data labeled as "100%" are that collected after the AFM began showing signs of extended pull-off regimes characteristic of reaching a saturated capillary state. In particular, the capillary bridge between the film and the AFM probe can be sustained to a very large separation distance of several tens of nanometers, so a weak tensile force is sustained after the tip is no longer in contact with the particles themselves. An example of such a force curve is shown in Figure 4.6. The challenge associated with maintaining the humidity just below saturation is also responsible for the small sample size in these trials, as seen in Table 4.1. In practice, the humidity fluctuated by about 3% in every trial except when the humidity was at 100%. No discernible differences in mechanical properties were noted over a range of humidity of less than 3%, except in the case of varying between 98% and fully saturated.

We observe a sharp transition in behavior between a humidity of 98% and complete saturation. As the chamber reaches total saturation, more load drops occur at very low loads below 200 nN and fewer load drops occur at high loads above 400 nN. In addition, the force curves collected at 100% humidity suggest that a capillary bridge forms between the tip and the sample which does not break until the AFM tip is tens of nanometers away. (At humidity levels below 60%, this bridge seldom extends more than 5 nm, if it

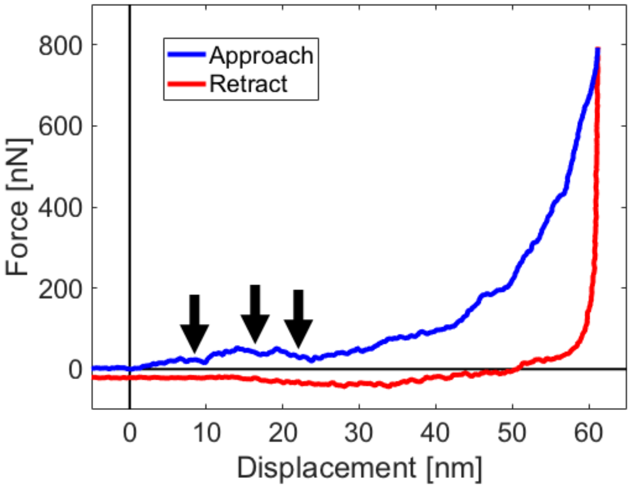

Figure 4.6: A force-displacement curve reflecting an indentation experiment performed under saturated conditions. Compare with Figure 4.1 . The sample deflects by over 30 nm requiring only minimal applied force. Most load drops at saturation occur at low loads, as shown by the arrows. In addition, the pull-off force is able to act over a distance of over 40 nm. This is a much greater distance than in unsaturated conditions, and is a result of the formation of a capillary bridge between the tip and the sample. This force curve is typical of many indentation experiments performed at saturation. The extended regime of deformation at low load is equivalent to that depicted previously in Figure 4.3, but is shown here in greater detail.

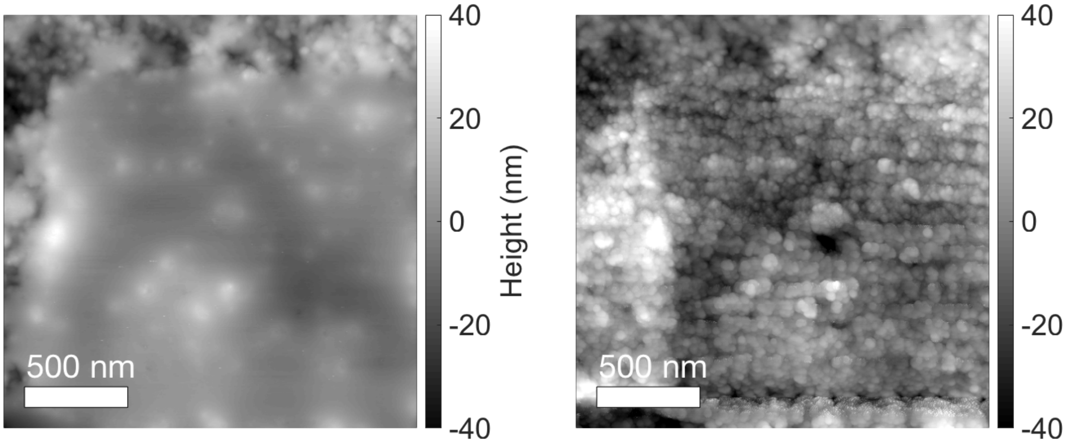

(a) (b)

Figure 4.7: Topography scan of a region collected after 256 nanoindentation experiments were performed on a square grid, under two different environmental conditions: (a) taken immediately after the scanning was complete, while the environment was at 100% humidity, and (b) taken after venting the chamber partially so that the environment was no longer saturated. Because of the abrupt change associated with venting the chamber, an exact measurement of the humidity is unavailable for Image 4.7b, but the relative humidity is almost certainly between 60% and 98%. No difference in scan quality is observed at humidities below 98%.

forms at all.) At such high humidity, the tip leaves a clearly visible track on the sample when traveling between indentation sites (Fig. 4.7b), despite the applied normal load being quite small, on the order of 80 nN. Once the packing is fully saturated, it loses some of its solid structure, weakening to what is proposed to be a viscous, almost slurry-like state. An example topography scan collected while the system was at saturation is shown in Figure 4.7a. This abrupt transition is also our best confirmation of the accuracy of the hygrometer, which registered 100% humidity at approximately the same time as the transition occurred. In addition, fogging and accumulation of condensation on the glass window further substantiated the estimate that the AFM chamber reached saturation.

4.3.3. Estimation of rearrangement sizes from topography images

Figure 4.8a shows a topography scan taken prior to indentation experiments. By comparing this image with its counterpart taken after indentations are performed, the extent

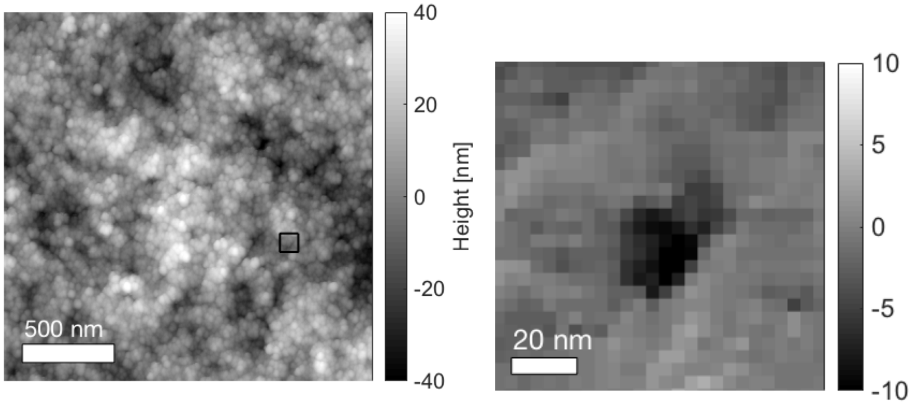

(a) (b)

Figure 4.8: (a) An example topography scan, taken prior to the experiments performed at 18% humidity. (b) A difference image; the topography after an indentation experiment has been subtracted from the topography prior to the indentation experiment. The disturbed region is approximately the area of a single particle, with no other particles disturbed. The region corresponds to the square in (a).

of plastic deformation can be observed. The two scans are carefully correlated to correct for drift and subtracted to observe the portions of the film that rearrange as described previously [6]. Figure 4.8b shows one such difference image. The plastically deformed region is limited to approximately 20 nm across, which suggests that only one or two particles have been perturbed. Deformation limited to such a small region might be most suitably represented by one or two T1 events, especially because the material is quite porous. By contrast, an STZ typically consists of multiple particles, typically moving in several directions [2, 3, 63] which may be expected to induce pile-up. There is no evidence to suggest that a single load drop event corresponds to motion of multiple neighboring particles, in the region shown in Figure 4.8b or in many other regions in the film. The depths of these load drop events were typically less than 3 nm, which is less than the diameter of even the smallest particles, which further demonstrates that the rearrangements are limited to only a handful of particles. A rearrangement of only 2 or 3 particles may have some properties of both types of event.

4.3.4. Estimation of elastic modulus of layer-by-layer assembled disordered nanoparticle packings

Although the present experiments violate some assumptions of the Oliver and Pharr model associated with small deformation [83, 84], it is nevertheless possible to estimate the elastic modulus for the AFM-based experiments using Equation 2.3. The probe is modeled using a spherical area function, and the contact depth is evaluated according to the method of Oliver and Pharr as discussed in Chapter 2. In those cases where the indentation depth is greater than the radius of the AFM tip, the contact area is taken to be a circle with the same radius as the indenter. This is a reasonable approximation because the tip is approximately cylindrical above the hemispherical end. It is important to note that with this analysis, it is not possible to appropriately account for sink-in: because the indentation depth is greater than the probe radius, the contact area is unchanged regardless of the choice of ϵ in Equations 2-3 of Oliver and Pharr.

Making the assumptions stated above, and given that the radius of this tip is 23 nm, the reduced elastic modulus is evaluated to be 11 ± 4 GPa at high humidity. The reduced modulus reached a maximum value of 19 ± 7 GPa at 18% humidity, which was the lowest humidity that could be attained with the current apparatus. These values are significantly greater than the values previously determined for silica nanoparticle packings in Chapter 3. As those silica nanoparticle films are believed to be more densely packed than the present films, this stiffening is primarily attributed to the rougher geometry of these crystalline particles. The softening at higher humidity may be attributed to three effects: the formation of larger liquid domains, which eventually merge and no longer benefit from surface tension; the reduction in capillary pressure near saturation [98]; and the shielding of adhesion forces brought about by the introduction of the liquid phase.

4.4. Concluding remarks

Layer-by-layer assembled disordered packings of titania and nanodiamond nanoparticles exhibit localized plastic deformation events during indentation which are similar to those reported previously for other disordered materials [2, 63, 48]. The magnitudes of these load drops feature an exponential probability distribution with many small rearrangements and fewer large rearrangements. This exponential function resembles the upper magnitude cutoff of an avalanche distribution [72]. The distribution shape and its significance will be discussed in greater detail in Chapter 5. The number of load drops that occur at a given indentation site varies with the relative humidity, with the material exhibiting more deformation at higher humidity. Under saturated conditions, the capillary bridges become continuous and the material behaves as a thick colloidal slurry. The indentation depth and energy dissipation per indent both increase, owing to the greater plastic deformation that occurs in this fluid-like state.

These results show that the mechanical response of the layer-by-layer assembled disordered nanoparticle packings depends strongly on the relative humidity of the environment. The results also suggest that this material system in its current form is not well suited for applications where mechanical stress may be applied while the environment is nearly saturated, because the packing is not structurally stable. Strengthening techniques such as atomic layer deposition [94, 95] or capillary rise infiltration [115, 116] may be able to overcome this obstacle. However, the transition in mechanical behavior at saturation may be useful in reshaping or molding disordered nanoparticle packings into different shapes or patterns on a surface, or to mitigate cracking. Also, the system could serve as a model system to represent a granular packing near the jamming transition, as well as disordered materials with various compositions or strengths of the inter-constituent bonds. This possibility will be exploited in Chapter 5, to demonstrate how this material system, placed under a variety of humidity conditions, can demonstrate the universality of avalanche scaling which has been previously observed in a variety of materials [8].

Future research may focus on distinctions in the magnitude and spatial extent of rearrangements that occur in disordered materials, as varied by tuning the humidity. The transition to a viscous state at high humidity may be of use in studying the surface mobility of glassy materials [41, 43] for the first time with constituent-level resolution.

Notes

A substantial portion of this chapter has been submitted for publication.

CHAPTER 5 : Loosely packed disordered nanoparticle packings exhibit yielding behavior in agreement with universal avalanche scaling

Many classes of materials, including both those with disordered structures and those that are crystalline, are known to exhibit discrete plastic deformation events that follow a scaling relationship known as avalanche behavior [9]. These materials include foams [117], metallic glasses [118, 119], the geological materials responsible for earthquakes [8], and nanocrystals [8]. As well, the behavior has been observed in finite element simulations which were intended to approximate a broad range of material systems while not specifically representing any particular material [72]. In the present chapter, it will be demonstrated that the nanoparticle packings investigated here also exhibit avalanche behavior, and that the humidity dependence of disordered nanoparticle packings may be leveraged to demonstrate the universality of avalanche probability statistics.

Avalanche behavior describes a particular relationship between the number and magnitudes of rearrangements. These rearrangements or relaxations are often described as slip events [118]. Specifically, the probability of a slip event occurring with a particular magnitude is inversely proportional to a particular power of the magnitude. The population probability distribution is a decaying function with a power law dependence, implying that the magnitudes of rearrangements are fractal in nature [9, 72]. The power law distribution ends at some upper cutoff of slip magnitudes, and the probability distribution drops off rapidly via an exponential decay [72]. This cutoff represents a maximum force or size of rearrangement that is possible in a sample of a given composition or size, which in some cases may be a system-spanning rearrangement [72] such as a shear band.

5.1. Review of avalanche scaling literature

Early work on avalanche dynamics was focused simulations of foam structures [120, 117]. In both of these studies, a simulated foam was constructed in a two-dimensional box and subsequently sheared. The slip events in both models consisted of bubbles either exchanging neighbors, or collapsing. Both observed that the magnitudes of slip events s followed a

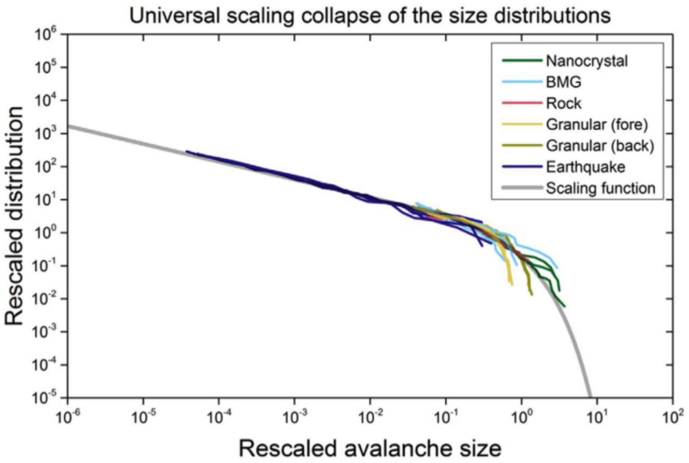

Figure 5.1: Scaling collapse of five different material systems onto a universal probability function, demonstrating that avalanche scaling is ubiquitous across many materials. Figure reproduced with permission from [8].

power-law probability distribution of the form $P(s) \propto s^{-\tau}$, where τ is a constant. The value of τ is not consistent between these studies, with Okuzono and Kawasaki reporting $\tau = 1.5$ and Durian reporting $\tau = 0.7$. The value reported by Okuzono and Kawasaki is consistent with mean field theory [121], and also with more recent literature [8, 9]. Durian chooses a value of s which is equal to the amount of energy released by the slip event normalized by the average energy per bubble, whereas Okuzono and Kawasaki normalize the amount of energy released by the total system volume. This discrepancy could account for the differences in scaling exponent.

More recent work on avalanches have investigated a wider range of material systems as discussed previously. Hard materials including rocks and bulk metallic glasses have been shown to exhibit avalanche scaling, consistently with a scaling exponent of $\tau = 1.5$ [8]. Several of these systems also exhibited the upper-magnitude cutoff described previously. The absolute magnitudes and number of observed slips varied greatly across the range of materials investigated, but when suitably scaled, all of the probability functions collapsed onto a single function relating slip event size and probability, as shown in Figure 5.1. The nature of these intermittent rearrangement events is that they imply causality: one slip event will sometimes trigger further events in the vicinity [121, 8, 37]. Smaller-scale slip events in a disordered material may take the form of an STZ [8], while a series of rapidly actuating STZs can comprise a system-spanning rearrangement in the form of a shear band [72]. It is worth noting that the word *avalanche* is sometimes used to refer to any type of intermittent plastic deformation event which does not necessarily exhibit avalanche scaling [35, 37]. Here, avalanche scaling specifically refers to intermittent plastic deformation events that exhibit a fractal distribution of relaxation magnitudes.

Due to challenges associated with binning small populations of data, some studies [8] choose to plot a complementary cumulative distribution function (CCDF) rather than a probability distribution function. Switching to this alternative plotting method has the effect of integrating the probability distribution, modifying the power law exponent τ from 1.5 to 0.5 [8]. The exponential cutoff remains present, although its functional form changes due to the integration. In the present work, both probability distribution functions and CCDFs will be used as appropriate depending on the number of data points, and the function being used will be identified clearly.

5.2. Layer-by-layer deposited nanoparticle packings exhibit behavior that is consistent with avalanche scaling

As demonstrated in Chapter 4, disordered nanoparticle packings that are deposited layer-by-layer exhibit load drop rearrangement events when subjected to AFM-based nanoindentation. These load drops are relaxation events, which are quite similar to the slip events described elsewhere in avalanche literature. In this section, it will be demonstrated that the magnitudes of these rearrangements exhibit avalanche scaling. This information can be used to further understanding of both nanoparticle packings, and also avalanche scaling.

It was observed in Chapter 4 that more load drops occur at relative humidities between 90% and 98% than at relative humidities in the ambient range of 20% to 50% (Fig. 4.5a). In order to collect statistics efficiently, in the present work all experiments have been performed under environmental conditions that were close to saturation (RH $>$ 90%), except as noted.

The distribution of load drop magnitudes resulting from nanoindentation of a disordered

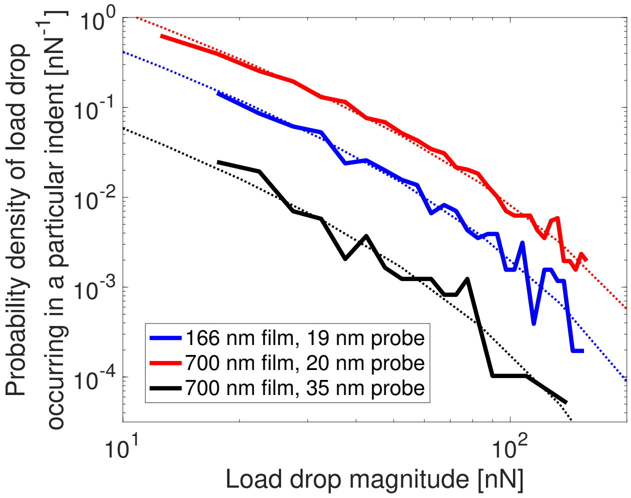

Figure 5.2: Nanoindentation experiments on disordered nanoparticle packings feature avalanche scaling. The probability distribution transitions from a power law to an exponential behavior over the range of load drop magnitudes accessible by experiment. Experiments performed on a comparatively thicker film exhibit more rearrangement events, while experiments performed with a comparatively larger AFM probe exhibit fewer rearrangement events.

nanoparticle packing is shown in Figure 5.2. The distributions are reported for three different permutations of film thickness and probe size. The number of load drops observed for each dataset is normalized by the bin width and also by the total number of indentation experiments performed under the given condition. This normalization produces a probability density which may be compared directly to an empirical probability distribution function. Also, the relative numbers of load drops observed in each scenario may be compared, as a greater total number of load drop events will shift the distribution upward.

Increasing the thickness of the film from 166 nm to 700 nm (corresponding to 30 and 300 bilayers respectively; the rate of deposition is not constant) results in a significant increase in the number of load drops. This increase is attributed to the increased likelihood that a weak region will be found somewhere under the indenter in the thicker film. This observation is similar to the observation of consistently less stiff behavior observed in a thicker film reported in Chapter 3. Increasing the probe size is found to dramatically reduce the number of load drops that are observed, most likely because a larger probe samples a larger contact area. A single displacement burst of a given distance requires that a larger volume of material be compressed, necessarily requiring a rearrangement of more particles. As rearrangements of larger sizes are more scarce, fewer are observed in total.

Each distribution features a slight downward curvature which fits the probability distribution proposed in Denisov et al. [9]:

$$P(s) \propto s^{-\tau} e^{-s/\xi}, \tag{5.1}$$

where ξ is a cutoff above which very few avalanches are observed, and the other parameters are as described previously. The value of τ was prescribed to be equal to 1.5, in accordance with prior studies [120, 8, 9] and mean field theory [121]. The cutoff magnitude ξ sets the force magnitude where the distribution shape transitions from a power law to an exponential distribution. In that sense, it is a characteristic force scale of the system; however, its interpretation is different from the decay length of an exponential distribution. In an exponential distribution, the decay length represents a “typical” size of rearrangements. Conversely, in avalanche scaling, the cutoff magnitude could hypothetically be arbitrarily large, and the majority of rearrangements would still be much smaller due to the fractal scaling below the cutoff. For the datasets shown in Figure 5.2, the cutoff magnitude was found to be in the range $30 < \xi < 95$ nN. However, across several datasets, the cutoff magnitude ξ was not found to have a consistent dependence on either probe size or film thickness.

The overall concave down appearance of the distributions in Figure 5.2 is quite repeatable. Nevertheless, it is not unreasonable to be skeptical of the proposition that the distribution shape shows the cutoff magnitude, as the shape of the curve is nearly linear. By altering the binning and normalization, it is possible to very convincingly demonstrate that a transition between power-law and exponential scaling is observed. In Figure 5.3, the data for the 700 nm film and 20 nm probe (red line in Fig. 5.2) is plotted with linear binning on a linear scale, and with logarithmic binning on a logarithmic scale. However, the number of load drops per bin have not been normalized by the bin width. An exponen-

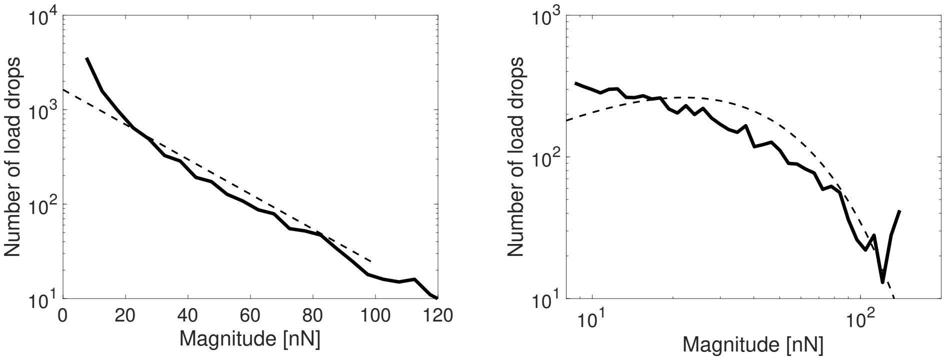

(a) (b)

Figure 5.3: Load drop magnitude distribution data binned two ways: (a) linearly, on a linear axis, and (b) logarithmically, on a logarithmic axis. The dashed lines depict the shape that data with an exponential probability distribution would exhibit under each binning configuration.

tial distribution would appear as a straight line under the binning configuration depicted in Figure 5.3a, whereas a power law distribution would appear as a straight line in Figure 5.3b. The shape of data exhibiting an exponential probability distribution is shown as a dashed line in both cases. The exponential distribution decays on the left side of 5.3b because the logarithmically spaced bin sizes become small faster than the exponential distribution grows.

The distribution of data exhibits exponential behavior on the right side of both plots, decaying rapidly toward the abscissa where power law scaling would feature a fatter tail. This observation is in keeping with the upper magnitude cutoff of an avalanche distribution. However, Figure 5.3b clearly shows a monotonically decreasing function, including a linear regime at the left side, which is unlike an exponential distribution but is in keeping with the behavior of a power law distribution. It is therefore reasonable to state that within the data there exists a transition from power law scaling to exponential scaling. It would be ideal to extend the data at the small end of the spectrum; however, the lower cutoff is limited by the noise floor of the AFM and no means to circumvent this problem has been identified.

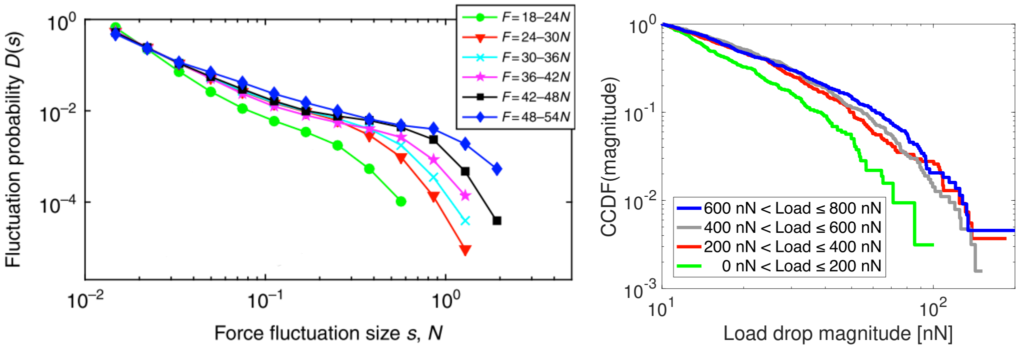

(a) (b)

Figure 5.4: (a) Probability density distribution of load drop magnitude data from a sheared granular packing. The data has been grouped by the magnitude of applied force acting on the sample at the time the rearrangement occurred. The upper-magnitude cutoff moves to the right as the applied force increases. Adapted from [9]. (b) CCDF of load drop data from nanoindentation experiments on a disordered nanoparticle packing. The cutoff marking the right side of the distribution moves to the right under higher loads. This shift is most notable in the middle of the distribution, corresponding to load drop magnitudes between 30 and 80 nN. This region comprises a much larger portion of the data than the region above 90 nN, where some of the CCDFs cross. Figure (a) reproduced with permission from [9].

5.2.1. The scaling cutoff shifts to higher forces as the applied load increases

The location of the scaling cutoff has been seen to be dependent on the applied load, as observed by Denisov et al. In that study, the authors sheared a granular packing of poly(methyl methacrylate) spheres immersed in an index-matched aqueous solution containing fluorescein which allowed the spheres to be imaged optically and their locations mapped. The force required to shear the packing was measured using a load cell. The packing exhibited slip events, which followed an avalanche distribution. The data was then divided into slip events that occurred at applied forces in each of several ranges, and the distributions of slip magnitudes occurring in each range of applied forces was plotted (Fig. 5.4a). The upper magnitude cutoff was seen to shift rightward under higher applied loads.

The data from the load drop magnitude distributions on disordered nanoparticle packings is able to approximately reproduce this force dependence. In Figure 5.4b, the load drop magnitude data from 593 individual indentation experiments has been divided by the applied load at the beginning of each load drop. The data is plotted as a CCDF due to the relatively small sample size of load drops occurring in each range of applied load. The cutoff representing the transition between power law scaling and avalanche scaling appears the same way in a CCDF as it does in a probability distribution function, excepting that the slope of the power law becomes 0.5 instead of 1.5. The cutoff shifts to the right at higher load, as predicted by Denisov et al. [9], indicating that under a greater applied load, it is also possible to initiate rearrangements of greater magnitude. Note that the CCDF is only sensitive to the shape of the distribution; that is, it is not sensitive to the number of load drops that occur. The data in Figure 5.4b should not be construed to imply any relationship between the number of load drops that occur in each range of force. Indeed, there was no repeatable trend in the number of load drops occurring in a particular range of forces.

5.2.2. The shape of the avalanche distribution is independent of environmental conditions

As discussed in Chapter 4, tuning the relative humidity in the AFM chamber provides a convenient means to tune interparticle forces. Under high humidity conditions more load drops are observed than at low humidity (Fig. 4.5a), implying a transition to a more viscous state in which plasticity occurs more readily. This enhancement in plasticity results from a change in capillary structure from the pendular or funicular state to the capillary state [7]. The change in capillary structure reduces the capillary force acting between particles. This occurs because the air pocket volumes and surface areas decrease at high humidity, resulting in a decreased contribution from surface tension, and because the capillary pressure comes to equilibrium with the atmospheric pressure as the relative humidity approaches saturation [98]. The flexibility to change the particle strength on demand allows disordered nanoparticle packings to be used as a model system for many other types of disordered materials, including strongly bonded metallic glasses and more weakly bonded granular materials.

Interestingly, tuning the environmental conditions is seen to have no effect on the shape of the avalanche distribution, except at saturation. This independence is seen in Figure 5.5.

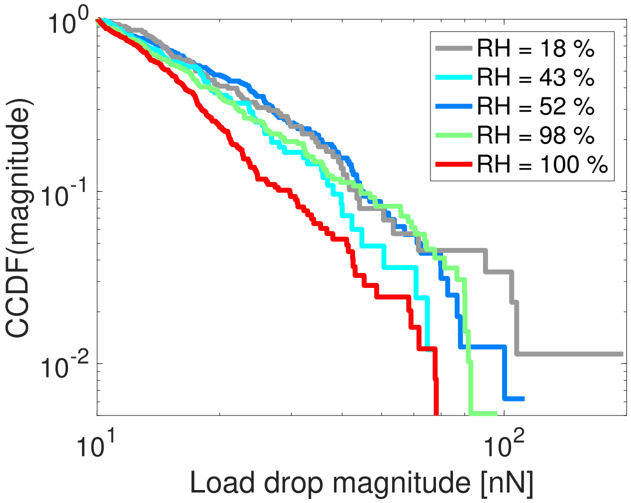

Figure 5.5: Complementary cumulative distribution function of magnitudes of rearrangement events occurring under a range of humidity conditions. Excepting the case of 100% saturation, there is no monotonic increasing or decreasing trend, suggesting that avalanche scaling is independent of the strength particle interactions. Note that the CCDF is only sensitive to the distribution shape and does not directly depict the absolute number of events. The number of rearrangement events in fact varies greatly between the five conditions shown here, as shown previously in Figure 4.5a.

As noted previously, the CCDF reflects only the distribution shape, and not the number of load drops that occur, as the latter effect is normalized. Chapter 4 demonstrated that the absolute number of load drops that occur is significantly greater at higher humidity; here it is observed that the shape of the distribution is unaffected. In particular, although the curves do not overlap perfectly in Figure 5.5, the positions of the curves reflecting relative humidities of 18%, 43%, 52%, and 98% do not shift monotonically left or right with humidity. Only the saturated curve appears to be distinctly out of line with the rest of the trend. Saturation may be thought of as a transition to a slurry [7], gel, or nearly fluid state [122], and the only resistive forces are due to viscosity and the weak adhesion interactions between particles. Therefore, the load drops, though perhaps more numerous, are generally smaller in magnitude under avalanche scaling.

This collapse of the datasets demonstrates that avalanche scaling is independent of interparticle bond strength, up to the limit where the material transitions to a nearly viscous state at saturation. This discovery helps to explain why avalanche scaling is observed in so many different material systems with a wide variety of adhesion forces: it can be stated that the scaling behavior is a function of the geometric structure of a disordered material, rather than a function of the strength of its bonding. This experiment marks the first time that interparticle interactions could be tuned in an experiment while simultaneously investigating avalanche statistics. In most other experimental systems, such bulk metallic glass [118] and colloids [9], the particle-particle interactions cannot be tuned in this way.

5.2.3. Constructing a composite force curve

The nanoindentation geometry used in the present study is unique among material systems in which avalanche scaling has been investigated, in that the predicted force-displacement response for a homogeneous material is nonlinear [92]. Many other experiments in which avalanche scaling is investigated are performed in shear [120, 117, 8, 9, 72] or uniaxial compression [118, 8]. In these systems, the expected relationship between the applied force and the sample deformation is linear, so the mechanical stiffness is expected to remain constant. Therefore, the magnitude of the slip event may be compared directly to the stiffness of the material without any correction.

In nanoindentation experiments with a spherical indenter undergoing small deformation, the expected relationship between force and displacement is a power law with an exponent of 3/2, due to the changing contact area. However, once the indenter sinks in beyond its radius, the contact area remains approximately constant and the stiffness may possibly be linear. In order to investigate whether there is a nonlinear response which may affect the avalanche distribution, here a composite force curve is generated. Figure 5.6a depicts a total of 768 unique indentation experiments, performed under the same environmental conditions and using the same AFM probe. The composite force curve, shown as a thick black line, represents the average indentation depth of all of the force curves at a particular load, in the same fashion as was done previously in Figure 4.3. The mean slope of all force curves is plotted as a function of depth in Figure 5.6b. It must be emphasized that the mean slope of all force curves plotted here is not equivalent to the slope of the composite

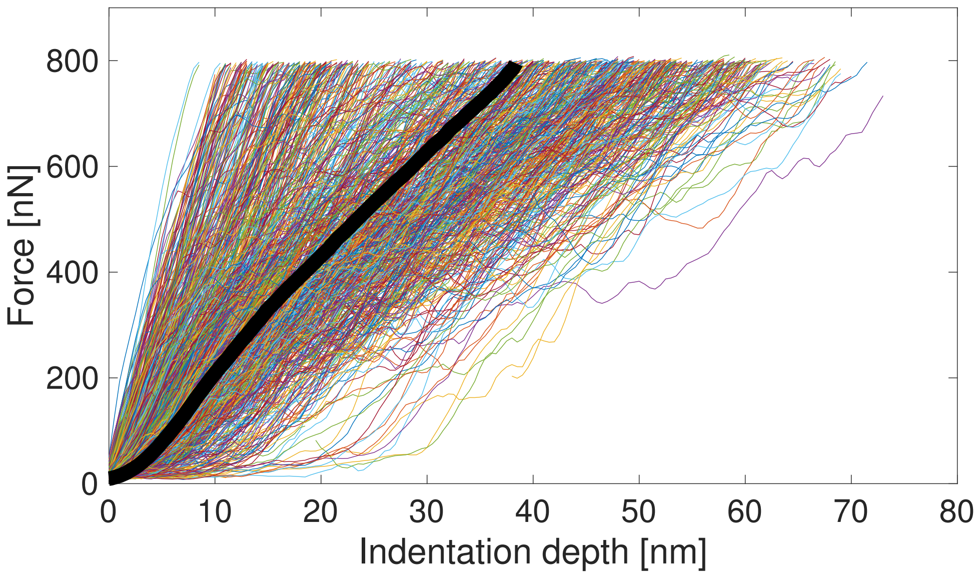

(a)

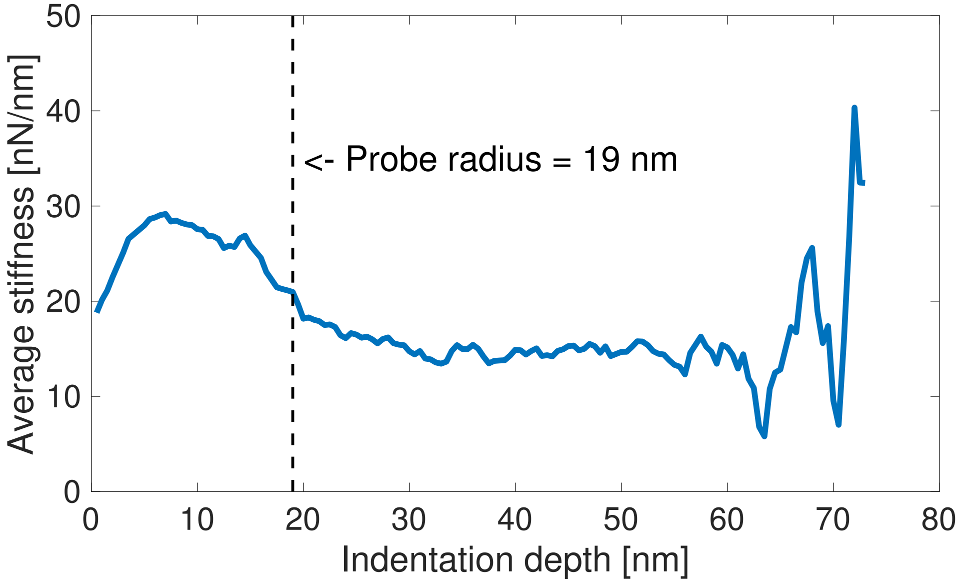

(b)

Figure 5.6: (a) A composite force curve (black) produced by averaging the indentation depths of a large number of force curves at every increment of applied force. (b) The average slope of all of the force curves as a function of depth. The mechanical response is approximately linear once the indenting probe has sunken in beyond its radius.

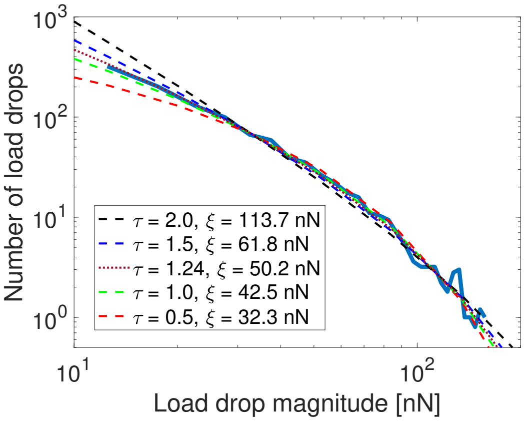

Figure 5.7: The distribution of load drop data corresponding to nanoindentation experiments on a disordered nanoparticle packing. The four dotted lines are fits to Equation 5.1, for several values of the avalanche scaling exponent τ. The value of $\tau = 1.24$ is the value determined directly by a least squares fit. The fitted cutoff force magnitude ξ is also given in the legend; the cutoff is seen to vary with the value of τ.

curve, because each of the force curves drops out of the moving average as it reaches its maximum value. The initial mechanical response is nearly (although not exactly[5]) Hertzian. Additionally, a Hertzian response would have an intercept at zero force and zero stiffness, which is not observed here. In this regime, relatively few load drops occur, and the mechanical response is dominated by elasticity. Once the indenter has sunken in beyond its radius, the contact area remains constant. Additionally, plasticity in the form of load drops contributes to weaken the material, producing the observed drop in stiffness. The stiffness becomes approximately constant above an indentation depth of 19 nm, which recovers a linear response, indicating that the present results can be compared with those in other experimental geometries discussed previously.

5.2.4. Testing the accuracy of the avalanche scaling exponent

Throughout this chapter, the value of the avalanche scaling exponent τ has been assumed to be equal to 1.5, which is consistent with many previous studies on metallic glass, geological materials, nanocrystalline materials, and colloidal packings [120, 118, 8, 9] and with mean field theory [121]. However, the scientific community is not in universal agreement on the value of this exponent, with some studies reporting values such as 0.7 in foams [117] and 1.27 in finite-element simulations [72].

---

[5] An exactly Hertzian response would correspond to a power-law relationship where stiffness $\propto \sqrt{\text{depth}}$.

Figure 5.7 shows how the avalanche distribution function (Eqn. 5.1) fits the data for several values of τ. The data presented corresponds to indentation experiments performed on a 700 nm film with a 20 nm probe (red curve in Fig. 5.2). The data most closely matches a value of $\tau = 1.24$, as determined using a least-squares fit; other datasets also produced exponents in the range $1.0 < \tau < 1.5$. The scaling exponent for the present system appears to be slightly less than the most commonly accepted value of 1.5, suggesting a slightly greater propensity toward larger size rearrangements as compared with other material systems. The value of the cutoff magnitude ξ varies with the avalanche exponent τ, as shown in the legend. This is expected: the avalanche scaling function attempts to fit the left side of the distribution with a constant, pre-determined slope, but depending on the selected value of the slope, more or less of the distribution can be fit in this way. Nevertheless, all fitted values of the cutoff magnitude are reasonable and within the range of the data, indicating that the cutoff between the power-law and exponential regimes was in fact observed in the present experiments.

5.3. *In situ* TEM nanoindentation experiments allow imaging of rearrangement events

In order to better observe the rearrangements that occur in association with avalanche scaling, an experiment similar to those discussed previously was performed *in situ* under the beam of a TEM. Two frames from a video of these experiments are shown in Figure 5.8, along with the force curve before and after a load drop occurs. A rearrangement about 60 nm across is visible in the center of the image. This rearrangement corresponds with the load drop of 2.3 μN, which is visible in the inset in Figure 5.8b. The slight recoil toward the bottom of the load drop occurs because the experiment is performed in displacement control, but the controller does not respond quickly enough to prevent overshoot when such a load drop occurs. The spatial extent of the rearrangement, as observed in the

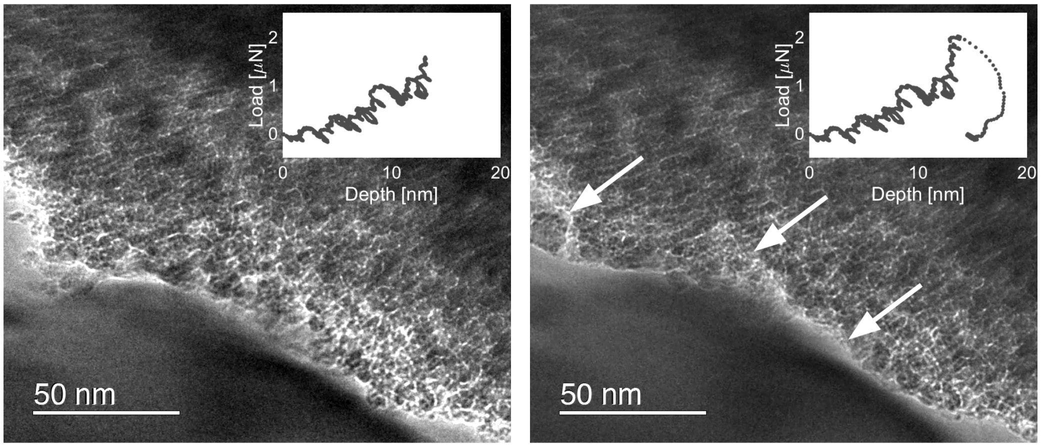

(a) (b)

Figure 5.8: Two frames of a video from an indentation experiment performed *in situ* under the beam of a transmission electron microscope, viewed from the side, (a) before and (b) after a load drop occurs. In the inset force curve of (b), the load drop is visible at right. The silicon substrate is in the top right behind the inset, the diamond indenter is in the bottom left, and the nanoparticle film is in the center. The arrows point to locations where rearrangements, corresponding with the load drop, are visible.

micrograph, indicates that it more closely matches the STZ picture of rearrangements than the T1 process; it may even be large enough to constitute a system-spanning rearrangement of multiple particles.

Due to the larger contact area, the magnitude of this load drop is much greater than the maximum load ever applied in AFM-based nanoindentation experiments in this study. The ranges of load drop magnitudes that can be explored by the type of experiments do not substantially overlap. Nevertheless, these *in situ* experiments exhibit an exponential distribution, as shown in Figure 5.9, which is similar to the high-magnitude cutoff observed in the AFM-based experiments. The exponential distribution is consistent for rearrangements that occur in dynamic contact, in which the indenter continues to vibrate but is in contact for the majority of an oscillation cycle, and the distribution is also consistent for rearrangements that occur in rigid contact where vibration has ceased. The oscillations out of contact do not feature the same scaling. Unlike in Figure 5.2, these data are not normalized by the total number of load drops. These experiments were performed in displacement control with a maximum depth specified, so the maximum force varies between indentations

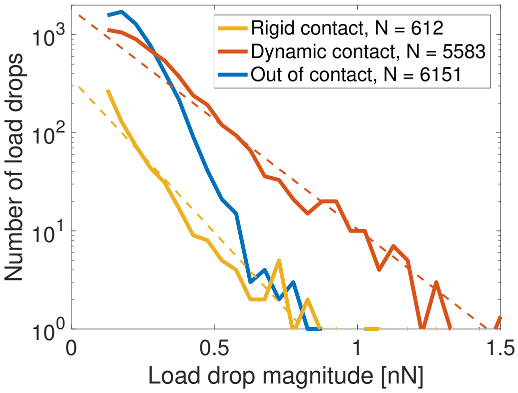

Figure 5.9: The distribution of load drop magnitudes for experiments performed in situ in the TEM. The blue curve represents load drops that occurred before the indenter made contact, which are part of the overall noise floor of the instrument. The root mean square of this noise is approximately 200 nN. The orange curve represents load drops that occurred after the indenter first made contact, but where mechanical oscillations caused the indenter to vibrate out of contact. The yellow curve represents load drops that occurred after the indenter made rigid contact, and was no longer vibrating.

and normalizing the data by the number of indentations would be nonsensical.

Because many of the load drops occurring in dynamic or rigid contact are smaller in magnitude than the amplitude of free oscillation out of contact, it must be demonstrated that the load drops in contact are not artifacts of the instrument's background noise. The similarity between the distributions corresponding to dynamic and rigid contact strongly suggests that these distributions represent the same mode of deformation. Conversely, the distribution due to the noise floor of the instrument is distinct from the other two distributions. This parallel between the dynamic and rigid contact data, and distinction from the out of contact data, confirms that white noise can be distinguished from authentic rearrangements, and that the exponential distributions observed here are reflective of the response of the material.

The exponential distributions observed in the *in situ* TEM nanoindentation experiments are consistent with the distribution shape observed in avalanche scaling above the upper-magnitude cutoff. Rearrangement events whose magnitudes are near or above this cutoff may be interpreted to be system-spanning, which is consistent with the large-scale rearrangement appearing visibly in multiple locations in Figure 5.8b. However, the decay lengths of the exponential distributions are on the order of 140-180 nN, which is not only larger than the cutoffs or decay lengths observed in the AFM-based experiments but also larger than all but the largest load drops ever observed in AFM. This larger decay length may be due to the larger contact area, or to the increased mechanical noise present in this system. In the *in situ* TEM-based system, the root mean square of the mechanical noise out of contact is approximately 200 nN, whereas for the AFM, it is only 0.5 nN. The vibration of the apparatus also serves to nucleate plastic rearrangements, and this dynamic effect combined with the larger contact area are likely responsible for the greater decay length. No power law scaling is observed, potentially because the TEM apparatus does not have adequate resolution to observe load drops less than 100 nN in magnitude, which a typical range for the cutoff as discussed previously in Section 5.2. Nonetheless, the *in situ* experiments demonstrate visually that load drops correspond with small particle-level rearrangements rather than any other mechanism of plasticity such as fracture or plowing.

It is worth mentioning that the TEM-based experiments are performed under high vacuum conditions, in which capillaries would not form. This stands in contrast with the AFM experiments, which were all performed at ambient pressure with relative humidity between 18% and 100%. However, as discussed in Section 5.2, the strength of bonds appears to have no effect on avalanche scaling except to change the number of events that occur. Therefore, it is reasonable to assume that the physical mechanisms that are at work in the AFM-based experiments are at work in the TEM-based experiments as well.

5.4. Radial distribution of deformation events exhibits exponential scaling

In this section, the average shape of a rearrangement event in the present nanoparticle packings is discussed. It is possible to quantify the spatial extent of a rearrangement by observing the displacement of the film, specifically based on the difference image between the topography images collected before and after a series of indentation experiments were performed. Figure 5.10a shows one such image, on a region in which a 16 × 16 grid of

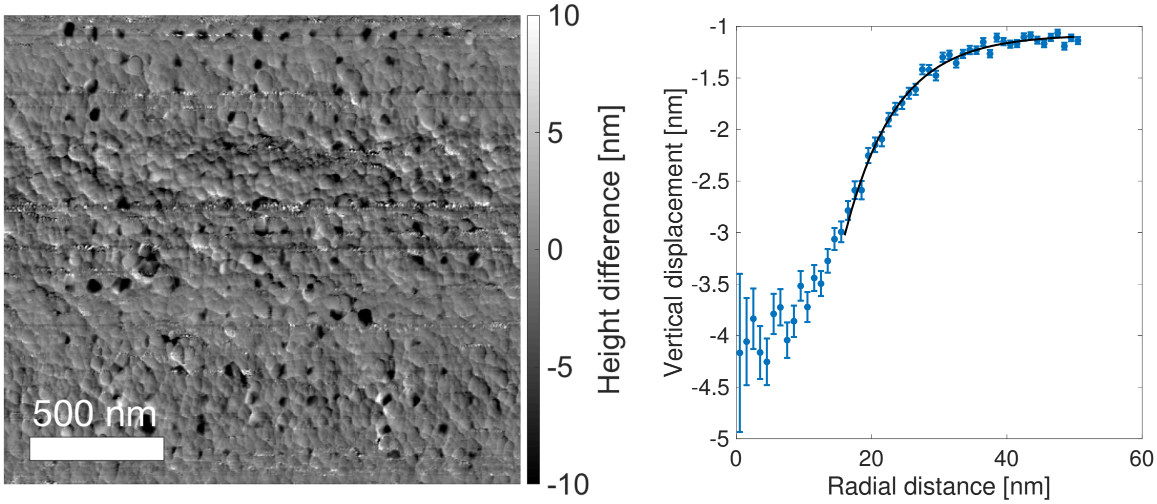

(a)

(b)

Figure 5.10: (a) A difference image collected between two topography scans before and after nanoindentation on a disordered nanoparticle packing, as shown previously in Figure 3.1c. This image features more indentation sites, which facilitates improved statistics. (b) A radial distribution of the heights of every pixel in 1 nm concentric annuli around all of the indentation sites. Beyond a particle radius, the shape of the distribution neatly fits an exponential decay with a decay length comparable to a particle diameter. The error bars represent the standard deviation of the mean of the displacements of all pixels within the annulus. The offset of the asymptote from zero is likely an artifact of the means by which the images were leveled.

indentations was performed with 100 nm spacings, each to a maximum load of 800 nN. This image is collected in the same way as described in Section 3.1. An average radial distribution function was evaluated by dividing the regions around each indentation site into concentric annuli, each with width 1 nm. The distribution function in Figure 5.10b represents mean and standard deviation of the mean of the collection of all points falling within a particular radius interval of their respective indentation sites.

Beyond a particle radius, the radial distribution function exhibits an exponential shape with decay length 7.57 nm. The observation that the radial distribution exhibits an exponential scaling is in good agreement with prior work investigating the length scale of cooperative rearrangements [59]. In that work, the spatial distribution of rearrangements in six distinct disordered materials were quantified using the D^2_{min} metric, which evaluates the mean square deviation of the motion of a constituent from an affine deformation of the nearby constituents [59]. It was determined that the magnitude of D^2_{min} decays exponentially with distance away from the epicenter of the rearrangement. The length scale of this exponential decay is 1.1 times the constituent diameter. Taking this factor, the decay length of 7.57 nm corresponds roughly to a constituent size of 6.9 nm. In the present system the particle diameters are 3.5-5.5 nm for the nanodiamond particles and 5-15 nm for the titania nanoparticles, which is in agreement with the prediction.

It is worth noting that the indentation depth varies greatly in different locations in the film, due to the structural heterogeneity that is present [6]. The data shown in Figure 5.10b was not normalized by the indentation depth, as it was determined that such a normalization does not significantly reduce the spread in the aggregated data. The distribution shown here can be taken to be the mean of 256 exponential distributions with similar decay lengths, and accordingly the resulting decay length is also an exponential.

The spatial extents of rearrangements in the current nanoparticle packings are in excellent agreement with the size scaling documented previously in simulations and experiments on colloids and granular materials [59]. The agreement between these studies furthermore indicates that this universality in the spatial extent of a rearrangement is independent of the means by which the rearrangement size is probed.

5.5. Concluding remarks

This chapter documents the first time that avalanche scaling has been observed in a granular material at the nanometer length scale. The reproducible behavior closely matches results previously reported by other researchers for nanocrystals, metallic glass, and geological materials [8, 9, 118]. Uniquely in the present disordered nanoparticle packings, it is convenient to tune the strengths of the interparticle interactions by way of adjusting the capillary force, and observe that the shape of the avalanche distribution remains relatively unchanged. The avalanche scaling that has been seen to be universal among many distinct material systems is here observed to also be universal within a single material system, in which the strengths of the particle interactions have been modified.

The universality of plastic modes of deformation among disordered materials [59] here extends to the length scale of rearrangements as well. This observation is particularly remarkable because the technique proposed here for identifying the length scale of a rearrangement is very different from that identified earlier [59]. The remarkable relationships between the plastic deformation mechanisms of various disordered materials are phenomena that are not fully understood. In the present results, the length scales and water content of the system were all varied and the mechanisms of rearrangement remained consistent. This strongly suggests that the nature of plastic deformation in disordered materials is primarily a consequence of the intrinsic random structure of the material, and not a consequence of the specific chemical composition or overall size scale.

Notes

Section 5.3 is adapted from text which has been submitted for publication.

CHAPTER 6 : Porosity enhances the ductility of nanoparticle films

The mechanics of granular materials are known to be strongly dependent on the density of the packing, as well as any externally applied stress [31]. At sufficiently high density, granular materials behave as a jammed solid, whereas at low density or under applied stress, they can flow in a viscous fashion similar to liquids. However, the mechanisms governing the transition from a solid-like state to a fluid-like state are not fully understood. This transition, the jamming transition outlined in Section 1.1.2, corresponds with a slight volumetric compression but no other change in structure. In granular materials featuring friction and adhesion, it is possible to attain another state: shear jamming [1]. Shear jamming represents a state where the packing density is below the random close packing fraction, but friction resulting from an externally applied stress provides the additional constraint needed to stabilize the packing. Understanding the mechanism of jamming as a packing is compressed remains an open research problem.

In this chapter, the mechanical properties of disordered nanoparticle packings with tuned packing fractions are examined. It will be demonstrated that indentation experiments on porous films exhibit greater indentation depths than on more densely packed films, and energy dissipation is greater. The stiffness of the packing, as probed at the level of a single nanoparticle, is not observed to change in the present results. These results suggest that less porous films have greater ductility than the closely-packed films. These results also suggest that shear jamming is at play: the packing is able to remain structurally stable at packing fractions well below the random close packing limit, but can more readily be made to deform under applied stress.

6.1. Synthesizing and characterizing porous nanoparticle packings

Two species of silica nanoparticles are used in the present chapter: LUDOX CL (Sigma-Aldrich, St. Louis, MO) with diameter 20.0 ± 4.8 nm, and LUDOX SM (Sigma-Aldrich, St. Louis, MO) with diameter 8.6 ± 1.3 nm. The 20 nm nanoparticles were selected to facilitate comparison with Chapter 3; however, very large indentation depths were often observed with this material when using the maximum load of 800 nN used in the previous chapters. The area function could only be computed accurately when the applied load was limited to 400 nN. The 8.6 nm particles featured smaller indentation depths, allowing the contact area, elastic modulus, and hardness to be computed for maximum applied loads of 800 nN.

The porosity of the packings is adjusted by changing the pH in order to allow the solutions to aggregate before spin-coating [17], as discussed in Sections 2.1.1 and 2.1.2. A complete description of the synthesis procedures is available in Sections 2.1.1 and 2.1.2. In addition to altering the porosity of the film, the process also changes the resulting film thickness. Both porosity and thickness are measured for several samples using fluid-cell ellipsometry, as shown in Figure 6.1. Both the porosity and the film thickness exhibit a slight increasing trend with aggregation time, which can be attributed to the growth of larger flocks in solution, as has been observed previously [17]. The samples selected for further study are circled. These samples were chosen so that wherever possible, the change in porosity would counteract the change in thickness. Any trend that is observed can be unambiguously linked to either the variation in porosity, or to the variation in film thickness. We decided not to alter the deposition conditions, such as solution concentration or spin rate, since these conditions would introduce an additional variable which could affect the structure of the film.

6.2. Mechanical properties evaluated on porous films

Figure 6.2a shows the stiffness S (defined as in Figure 2.5b) measured on films with varied packing fractions. Two sets of films were used, one corresponding to each of the types of nanoparticles observed previously. No systematic variation in the stiffness S can be observed. This result is surprising, as the rule of mixtures [123] suggests that a 30% decrease in density should reduce the stiffness by a similar amount. By contrast, the average indentation depth is seen to be less at greater packing fractions, as is the amount of energy dissipated per indentation experiment (Figs. 6.2b and 6.2d). This suggests that the film becomes more prone to plastic rearrangements as the density decreases. This implies

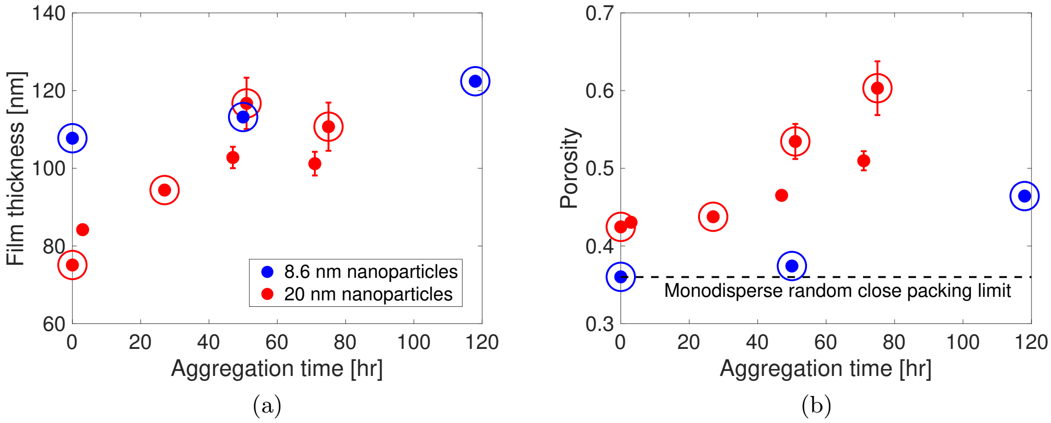

Figure 6.1: (a) the thickness and (b) the porosity of films prepared after various aggregation times, as measured by fluid-cell ellipsometry. Of these samples, the circled samples were selected for further study.

a transition to more ductile or fluid-like behavior, which indicates that compressing the material below the shear jamming transition should convert the system to a shear-jammed state [122]. The elastic modulus evaluated during the approach part of the force distance curve can be evaluated using the Hertz model [92], as shown in Figure 6.2c. The Hertz contact modulus is seen to be greater at high packing fraction, which stands in contrast to the stiffness, which shows no dependence on packing fraction.

The result that stiffness does not change with porosity is unexpected, and merits further discussion. One possible explanation is that due to the presence of voids, the film is more readily able to compact and rearrange during the approach portion of the force curve. The packing is able to reach a stable configuration because particle mobility is unhindered. Once the maximum load is reached, the packing may have attained a stable and densely packed configuration which behaves similarly to a film that was closely packed from the outset. This is a challenging hypothesis to test in an experiment. It could, however, be tested in simulation where the trajectories and number of contacts of every particle can be tracked. The fact that the contact modulus evaluated via the Hertz model increases as expected [102] bolsters this hypothesis: a loose packing does initially exhibit a more compliant mechanical response than a dense packing, but upon compression it becomes densely packed and is as

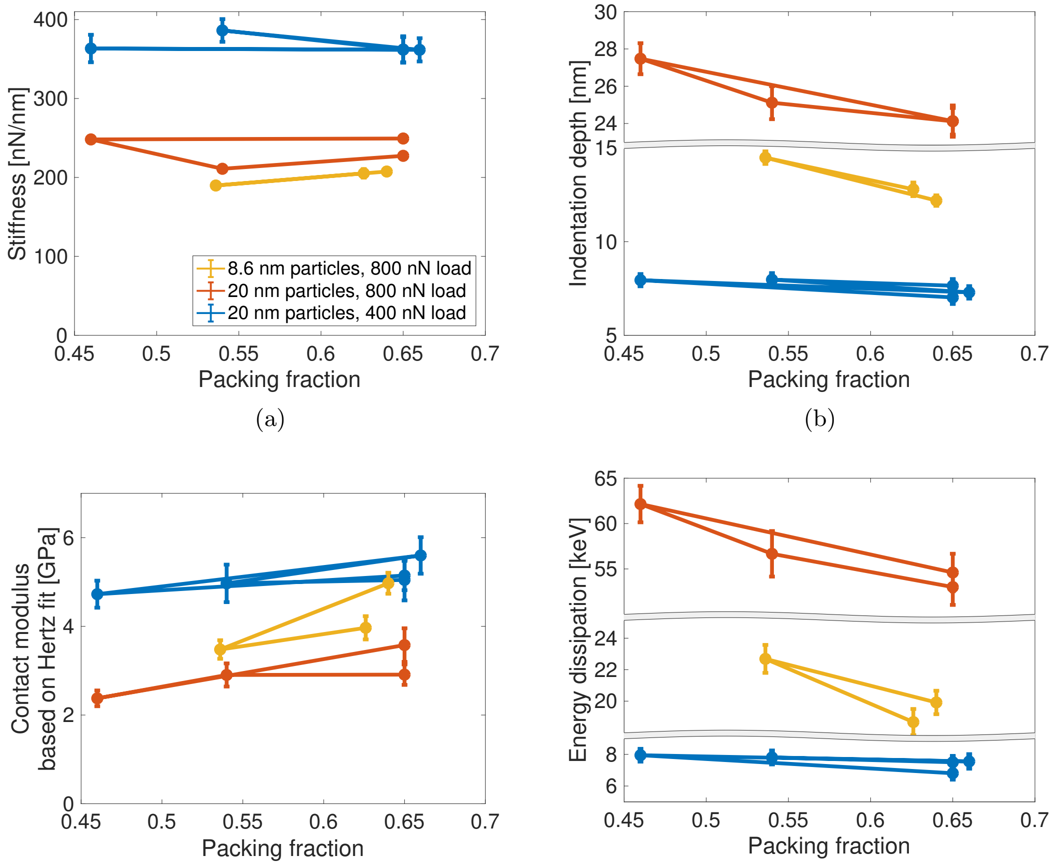

(a)

(b)

(c)

(d)

Figure 6.2: The measured (a) stiffness, (b) indentation depth, (c) elastic modulus evaluated via the Hertz model, and (d) energy dissipated resulting from indentation on films of two different species of nanoparticles, aggregated for different periods to produce films of various porosities. For the 20 nm particles, two different peak loads were selected: 800 nN to match with the 8.6 nm particles, and 400 nN to allow for an analysis of elastic modulus and hardness, as discussed in the text. The lines indicate the order in which the experiments were performed, which was randomized. Indentation depth and energy dissipation both decrease as density increases. There is no evidence that porosity affects the measured stiffness of the material.

stiff as a packing which was densely packed at the outset.

In Figures 6.2 and 6.3, the error bars are the standard deviation of the mean of the total number of experiments, which ranged from 51–64 per data point. Due to the large number of experiments, in some cases the error bars are nearly invisible. Most of the indentation depth and energy dissipation data collected with maximum loads of 800 nN exhibit distributions which are statistically distinct with $p < 0.05$. The distributions of the Hertz contact modulus data do not always exhibit statistical significance; however, the increasing trend remains clearly repeatable in every experiment. The sole exceptions are the data collected on the 20 nm nanoparticle film with a packing fraction of $\Phi = 0.54$. In some cases these data cannot be distinguished with statistical significance from the data corresponding to $\Phi = 0.65$ and $\Phi = 0.46$ with the same nanoparticle species. However, the data corresponding to $\Phi = 0.65$ and $\Phi = 0.46$ are statistically distinct from each other in all cases. The dataset collected for the 20 nm particles using a maximum load of 400 nN does not pass the T-test for statistical significance, but nonetheless the trends are in agreement with the trends in indentation depth and energy dissipation observed in the other two datasets.

6.3. Evaluation of intrinsic mechanical properties

For the datasets associated with the 8.6 nm nanoparticles and the 20 nm nanoparticles indented to a maximum load of 400 nN, the measured values of hardness and effective elastic modulus are plotted in Figure 6.3. Due to the high indentation depths in the case of the 20 nm diameter particles loaded to 800 nN, which in many cases exceed the tip radius, it is not possible to accurately evaluate the elastic modulus or hardness because the area function cannot accurately be computed. The hardness is seen to increase with packing fraction for each of the two sets of data, and the effective elastic modulus is seen to increase with packing fraction only for the 8.6 nm nanoparticles. The stiffness S was previously observed to be unaffected by indentation depth (Figure 6.2a). The elastic modulus is a function of the stiffness S and of contact area (Eqn. 2.3); the latter is a function of indentation depth

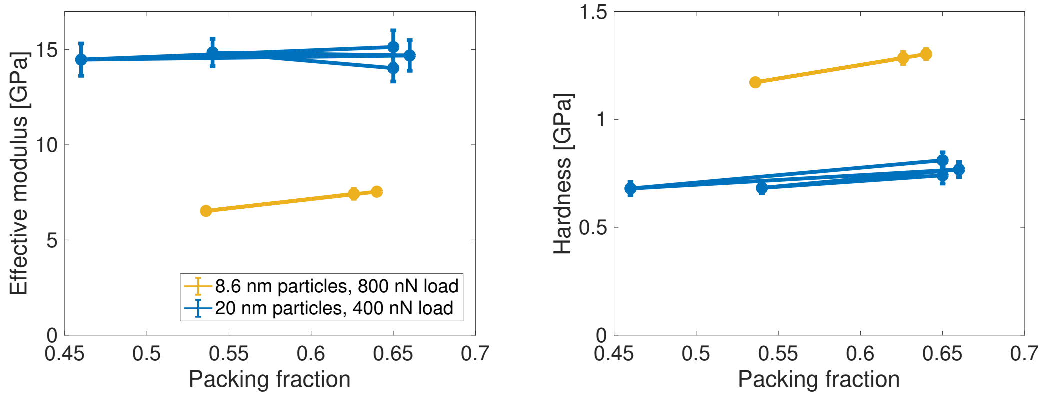

(a) (b)

Figure 6.3: The measured (a) effective elastic modulus and (b) for two different films of nanoparticles. Hardness is seen to increase with packing fraction; the elastic modulus is seen to increase only for the 8.6 nm nanoparticles. Both of these trends can be explained by the change in indentation depth shown in Figure 6.2b, as discussed in the main text. The ellipsometry measurements were performed by Jyo Lyn Hor.

[83, 84]. Hardness is a function only of the applied load, here prescribed to be 400 nN or 800 nN and the contact area (Eqn. 2.5). Therefore, it appears that the fluctuations observed in Figure 6.3 are solely due to the change in indentation depth, as the maximum load is fixed and the stiffness, while variable, does not change systematically with porosity.

The observation that the elastic modulus does not vary with porosity may be contrasted with the mechanical properties of bidisperse frictionless granular packings. One study investigated the mechanics of a packing of frictionless polydisperse spheres, which had diameters ranging from 3 to 35 nm and which interacted via a Lennard-Jones potential function [124]. Simulated nanoindentation experiments demonstrated that a denser packing exhibited a stiffer mechanical response [124]. Because these packings had no friction, they were necessarily at or very close to the close packing limit, as this is a prerequisite for rigidity in frictionless systems. The porosity was varied by tuning the polydispersity of the system, which also changes the close packing limit. The system was intended to represent concrete, so the sizes of spheres were bidisperse to separately represent aggregates and the cement phase. It is likely that some combination of the lack of friction, the polydispersity of particle sizes, and the proximity to the close-packed limit, explains the discrepancy in behavior.

Table 6.1: Measured values of the effective elastic modulus and hardness of nanoparticle films prepared from 20 nm diameter silica nanoparticles, and the mean indentation depths observed for each set of experiments. The film deposited without adjusting the pH had no opportunity for aggregation. The second film was spin-coated immediately after adjusting the pH. All measurements were performed with a maximum load of 400 nN.

Deposition condition	Eff. elastic modulus	Hardness	Indentation depth
pH not adjusted	12.9 ± 1.0 GPa	1.1 ± 0.1 GPa	3.1 ± 0.2 nm
pH adjusted to 6.4	14.7 ± 0.8 GPa	0.77 ± 0.04 GPa	7.3 ± 0.3 nm

The measured value of the elastic modulus in the densely packed film (in which the pH of the original solution was adjusted, but the solution was deposited without any time to aggregate) is comparable with the results in Chapter 3 [6]: the spread of the two datasets overlap, and the mean values of the two datasets differ by only 13%. The measured elastic modulus and hardness of each film is summarized in Table 6.1. The uncertainties given here are the standard deviations of the mean as in Figures 6.2 and 6.3. Interestingly, the modulus is seen to increase when the pH is adjusted, whereas the hardness is seen to decrease; however, the moduli and hardnesses actually match within the spread of the data. The indentation depth is substantially greater in the film in which the solution pH was adjusted than the film where the pH was not adjusted. This could indicate that the adjustment resulted in a slightly greater porosity which accommodated greater deformation. However, the experiments were performed on different days with different AFM probes, so exact comparisons are tenuous.

Conventional nanoindentation (TriboIndenter, Hysitron, Inc.) using a Berkovich indenter was performed on nanoparticle packings of nominally identical composition to those described here, but the pH of the colloidal solution was not modified and the spin coating was performed repeatedly to produce a 430 nm thick film. The greater film thickness was necessary to accommodate the greater depth of the affected volume that results from conventional nanoindentation. These experiments indicated that the effective elastic modulus was 22 ± 10 GPa, which is greater than the value determined by AFM (Table 6.1), but the range of values determined by each method overlap within the uncertainty of the conventional nanoindentation measurements. No published studies have been found where conventional nanoindentation experiments were performed on the 20 nm silica nanoparticles used in this study (Section 2.1.1). However, studies performing conventional nanoindentation on 24 nm silica nanoparticles with a rougher texture (Fig. 2.1c) revealed an elastic modulus of 16 ± 1 GPa [95].

6.4. Concluding remarks

The present work reflects the first time that the mechanical properties of a nanoscale granular material have been characterized at the single constituent scale over a range of packing fractions. The results here indicate that disordered nanoparticle packings may be strengthened by tuning the deposition conditions to produce a densely packed film, and conversely may be made more ductile by producing a more loosely packed film. These conditions may be achieved by spin-coating suitably aggregated solutions [17], or for a densely packed film, by spin-coating films which have not been aggregated [80]. It is also possible to deposit a nanoparticle film using the layer-by-layer technique rather than the spin-coating technique used in this chapter. Using the layer-by-layer technique, the porosity can be adjusted by carefully tuning the pH of both solutions [125]. By adjusting the pH, the coverage of each layer is tuned, which results in a change in porosity as the film is built up. Although an investigation of the tuning of pH is outside the scope of the present work, it may be a suitable method for producing strong, tough packings on irregular surfaces where spin-coating cannot be performed.

Several of the nanoparticle packings discussed in this chapter have packing fractions which are well below the close-packed limit of 64%. The packing is nevertheless stable under these conditions, even though a frictionless packing of the same density would not be packed tightly enough to achieve stability [37]. The combination of adhesion and friction provides the additional forces needed to fully constrain this system. This system is not in the true shear-jammed state when it is at rest, as the shear-jammed state exists only under an external applied stress [1]. However, the region in the immediate vicinity of the indenter may be viewed as shear jammed. As the load increases, the system is deformed into a new state with greater stability, echoing the observed change in local structure that has been previously observed in simulations of shear-jammed packings [126].

It may be possible to use the present material system to more fully study the phenomenon of shear jamming, and its counterpart, the fragile state in which any relaxation of the applied force will result in flow [1]. Existing research is limited to simulations [126] and packings of macroscopic granular materials [1, 127, 122]. By contrast, disordered nanoparticle packings represent the smallest length scale at which a frictional packing is able to exist, and could provide further information about the scaling of this phenomenon. In particular, at the nanoscale, adhesion forces become significant [128, 129] and will significantly alter the mechanics of the material. One means to study the shear jammed and fragile states is to use the AFM in a mode similar to the continuous stiffness method used in conventional nanoindentation [130]. Although impossible to accomplish using the Bruker Nanoscope software used for this study, it may be possible to program the AFM manually. By applying a small cyclic load as the applied force is increased and observing the stiffness of the response, it could be possible to identify the load or indentation depth at which a transition to rigidity occurs. This procedure could then be repeated on nanoparticle thin films of various porosities as was done in the present chapter. With this information, the shear jamming phase diagram could be mapped for the first time in a material with strong adhesion interactions.

CHAPTER 7 : Conclusions

Though techniques for synthesizing disordered nanoparticle packings abound [82, 81, 17, 115], and their mechanical properties have been characterized at the bulk scale [93, 79, 131, 132], the fundamental deformation mechanisms of disordered nanoparticle packings have not until now been investigated at the constituent length scale. Atomic force microscopy provides the tools needed to characterize plasticity in nanoparticle packings with excellent spatial resolution. The sub-micronewton forces required to induce rearrangements at the particle level without triggering a shear band, fracture, or system-spanning avalanche match the measurement capabilities of AFM-based nanoindentation.

The present work demonstrates that disordered nanoparticle packings under applied stress feature rearrangements that share strong similarities to the shear transformation zones identified in prior literature on bubble rafts [2] and colloidal silica glasses [63]. The exact signature of these rearrangements in the force-displacement response depends on the nature of the film, with smooth yielding commonly occurring in dense spin-coated films (Chapter 3) and unstable load drops in porous films deposited layer-by-layer (Chapter 4). However, the size of the rearrangement in all cases is on the order of a handful of particles. It is possible to tune the mechanical response of the material by changing the environmental conditions (Chapter 4) and also by changing porosity (Chapter 6). In whole, the mechanical response of disordered nanoparticle packings under a variety of deposition, loading, and environmental conditions are now more fully understood. In addition to being integral to the design of nanomaterials with targeted mechanical properties, this work contributes to the scientific understanding of the mechanics of disordered materials in general.

7.1. Implications for the general problem of plasticity in disordered materials

Several of the findings in the present work bear marked similarities to results related to other disordered materials. Most notably, the present work was included in a seminal study which demonstrated that various disordered materials all exhibit a similar yield strain of $2.9 \pm 0.3\%$, even though the systems studied spanned a wide range of sizes, dimensionality, and bonding configurations [59]. Twelve types of experiments and three simulations were performed on a variety of materials, including metallic glass, polymers, colloidal packings, and granular materials. These materials spanned twelve orders of magnitude in stiffness and ten orders of magnitude in constituent size, indicating that the scaling of mechanical response is universal and independent of size and stiffness. Tensile, compressive, indentation, and shear experiments were used to explore these materials. Despite the wide range of materials and geometries investigated, the universal scaling in yield strain was still observed. An analysis of the size of rearrangements was also performed in six of the investigated systems, demonstrating that the spatial extent of rearrangements featured an exponential decay with a decay length on the order of a constituent diameter. Although the present disordered nanoparticle packings were not a part of the latter analysis, it was demonstrated in Section 5.4 that an analysis of the spatial extent of rearrangements in nanoparticle packings produces a similar result to that found in the study of Cubuk et al. [59]. The fact that this matching result was determined by a completely different method as the original study [59] shows that this universal scaling relationship is independent of the means of analysis.

Another seminal study demonstrated that a wide variety of materials, including nanocrystals, metallic glass, and geological materials universally exhibit avalanche behavior under mechanical load [8]. As well, in other work, larger-scale granular materials have been observed to follow similar scaling [9]. In Chapter 5 it is demonstrated that disordered nanoparticle films, not covered by these prior studies, exhibit similar scaling behavior. Avalanche scaling indicates that a plastic rearrangement or slip event has the potential to trigger one or more subsequent events, resulting in large-scale deformation initiating from a single site. This is the first time that avalanche scaling has been identified in a nanoscale granular material. This material provides a convenient system in which avalanche scaling may be investigated. It is convenient to change various properties of this system, including the constituent and sample size [81], the bonding and environmental conditions, and the porosity [125]. For example, it has been demonstrated that changing the sample size and indenter size do not significantly affect the overall shape of the avalanche distribution; however, the number of rearrangement events that occur does change. When the ambient humidity is increased, more rearrangements occur, but the overall shape of the avalanche distribution remains unaffected except at saturation. These findings serve to demonstrate why avalanche scaling is so ubiquitous: it is independent of length scale and the strengths of the bonds between constituents. Avalanche scaling is driven primarily by geometry and structure, one of the few aspects of the present material system that remained consistent in all of these experiments.[6]

Further similarities are identified between the present material system and other disordered materials; however, unlike the prior discussion of plasticity and avalanche scaling, these similarities cannot be quantified as readily. As discussed in Chapter 3, disordered nanoparticle packings exhibit substantial spatial mechanical heterogeneity, with mechanical properties varying by up to 80% across different locations. Locally strong and weak spots in these films can be identified using nanoindentation. These locally strong and weak spots are similar to those which have been identified previously in simulations using a vibrational mode analysis [37] and in experiments on metallic glasses using dynamic AFM [39, 133].

In Chapter 3, disordered nanoparticle packings are observed to compact under repeated loading. This phenomenon has also been observed in granular materials using other techniques such as mechanical vibration [134]. Nowak et al. demonstrated that the granular material stiffens as it is compacted, which matches prior research on compaction [135]. This finding also agrees with the literature on jamming, which states that above the jamming transition, the material stiffens as the density increases, at a rate proportional to the square root of the increment of the packing fraction [31]. It is likely that mechanical annealing could be used to strengthen or toughen this material, if a means could be identified to do so on a deposited film. This could be accomplished, for example, by applying a conformal plate to the thin film and cyclically applying a load to the plate. It would be important to choose surface chemistry so that the particles do not adhere to the plate. This condition is particularly important because, in the present work, particles have sometimes adhered to the AFM probes.

---

[6] The size and chemical composition of the present material was also consistent throughout the present experiments; however, this factor could not also explain why similar scaling is observed in the scientific literature in vastly different materials.

Substantial research has been dedicated to the study of capillary structure in granular materials exposed to water vapor [7]. In Chapter 4, it was demonstrated that the change in capillary structure between the pendular, funicular, and capillary states as a function of relative humidity causes an attendant change in the mechanical properties of the film. Specifically, the finding that the material weakens or softens under higher humidity agrees with findings from simulations on pairs of nanoparticles [112] and on granular packings [111], suggesting that the force exerted by capillary bridges weakens as the ambient humidity and size of the capillary grows. The fact that the pull-off forces between the AFM tip and the nanoparticles increase as the humidity increases is an unusual result compared with most capillary literature, but it is in line with experiments that were performed on surfaces with nanometer-scale roughness [114].

7.2. Future work

The research described in this thesis could be continued in several directions as outlined below. The directions of research described here will be of interest to the scientific community because the information to be discovered will elucidate how the plasticity of nanoparticle packings relates to the bigger picture of plasticity in disordered materials. Moreover, commercial applications of these materials will benefit from superior understanding of the effects of tuning their deposition conditions, and the means by which these materials may be strengthened.

7.2.1. Simulations facilitate understanding of the significance of material parameters that cannot be directly investigated in experiment

In the present work, methods have been identified to tune parameters associated with certain aspects of the system: the film thickness (Chapters 3 and 5) the packing fraction (Chapter 6), the interparticle forces (Chapter 4, and the particle size (Chapter 6). Other parameters are more challenging to control directly, such as interparticle friction and damping. Nevertheless, these parameters are quite significant and preliminary investigation suggests that they have a substantial impact on the mechanical properties of the material.

Computer simulations offer a potential means to investigate the effects of tuning some of these parameters which are out of the reach of experiments. Continuing the computational work which was briefly mentioned in Chapter 3, it will be possible to systematically probe the effects of friction and damping, among other possibilities. Even the adhesion force, which was controlled indirectly via humidity (Chapter 4), may be controlled with greater independence in simulations. In the existing experimental work, the formation of capillary bridges may simultaneously affect friction, damping, and repulsive interactions as well. The information to be learned from simulations will be helpful in understanding how the results observed here relate to the general problem of plasticity in disordered materials. In particular, it may be possible to more fully understand the differences between various disordered materials. For example, the load drop analysis in Chapters 4 and 5 yields a density of one defect per every six particles in a nanoparticle packing. By contrast, conventional nanoindentation on metallic glass suggests a defect density that is orders of magnitude lower [40]. It is likely that this discrepancy relates to the sizes of constituents, or the ratio between strengths of particle-particle bonds and the magnitude of the applied force acting on each system. Simulations may be able to determine to what degree the defect density is sensitive to the parameters of the analysis technique used to measure it. For example, changing the threshold for the minimum size of load drop that is recognized as a rearrangement will change the number of defects that are observed.

7.2.2. Varying deposition conditions can strengthen a disordered nanoparticle packing

Previous work has demonstrated that disordered nanoparticle packings can be strengthened by performing atomic layer deposition to create a conformal coating that provides rigidity by strengthening interparticle contacts [94, 95]. Another option is to introduce a polymer matrix that fills in the gaps between the particles via capillary rise infiltration [115, 116], which produces a nanocomposite. Conventional nanoindentation experiments have been performed on disordered nanoparticle packings that were assembled using each of these techniques; however, neither type of strengthened packing has been mechanically probed at the constituent length scale, as is possible with the techniques proposed in the present work. It is likely that the atomic layer deposition-strengthened films would become more brittle as a result of the small aluminum oxide bridges that form, which upon breaking would not reform bonds. Conversely, the films prepared via capillary rise infiltration may have some capacity for ductility because the interstitial material is a viscous polymer. As such, rate-dependent mechanical properties may be observed, and a relaxation or healing time might be identified.

Packings synthesized from anisotropic nanoparticles have been demonstrated to feature improved strength and stiffness over films produced from isotropic nanoparticles [79]. Using the techniques described in this thesis, such films could be investigated at the single-constituent level to more fully understand how anisotropy affects the mechanical response of these nanoparticle packings. An outstanding challenge is to find a way to prevent adhesion between the titania nanoparticles and the diamond-like carbon tip. This could possibly be accomplished by changing the surface chemistry of the AFM tip or by performing the experiments in a fluid which would reduce the force of adhesion.

7.2.3. Means of tuning porosity in layer-by-layer films

In Chapters 4 and 5, it was discussed how a layer-by-layer deposited film exhibits load drops which likely come about due to the collapse of voids. These films are unusually porous, often having packing fractions below 60% [82]. The packing fraction may possibly as low as 48%, as determined using Rutherford backscattering. This is markedly less than the random close packing limit of 64% for monodisperse spheres, and the random close packing limit would in fact be greater for the polydisperse spheres used in these layer-by-layer deposited films. In Chapter 6, the porosity of a spin-coated film is tuned directly by way of aggregation [17], and the attendant effects on mechanical properties have been investigated. It is also possible to control the porosity of a layer-by-layer deposited film by altering the pH of the nanoparticle solutions [125]; however, this was outside the scope of the present work.

Future work could focus on how altering the assembly conditions for layer-by-layer deposition affects the mechanics of the film. The pH of each solution could be tuned through a range and nanoindentation experiments could be performed as discussed previously. Ideally, a set of deposition conditions would be identified which produces a layer-by-layer film with a high packing fraction, comparable to the spin-coated films. If such a film can be produced, it will be possible to determine whether the load drops observed previously in nanoindentation experiments on porous layer-by-layer assembled packings continue to occur on the more densely packed film. This information could test the hypothesis presented in Chapter 4 that the load drops observed in the layer-by-layer films are the result of the collapse of voids. Moreover, the results would be of substantial commercial interest, because they would suggest how the films could be stiffened or strengthened by tuning the assembly conditions.

7.2.4. AFM-based scratch testing experiments suggest how disordered nanoparticle packings may survive working conditions

Disordered nanoparticle packings have been proposed for many applications, including optical coatings [81, 17, 19] and nanoprinting for microelectromechanical systems [21]. In some such applications, the packings are susceptible to abrasive wear, such as debris falling on or blowing over a solar cell or window. Present deposition techniques produce films

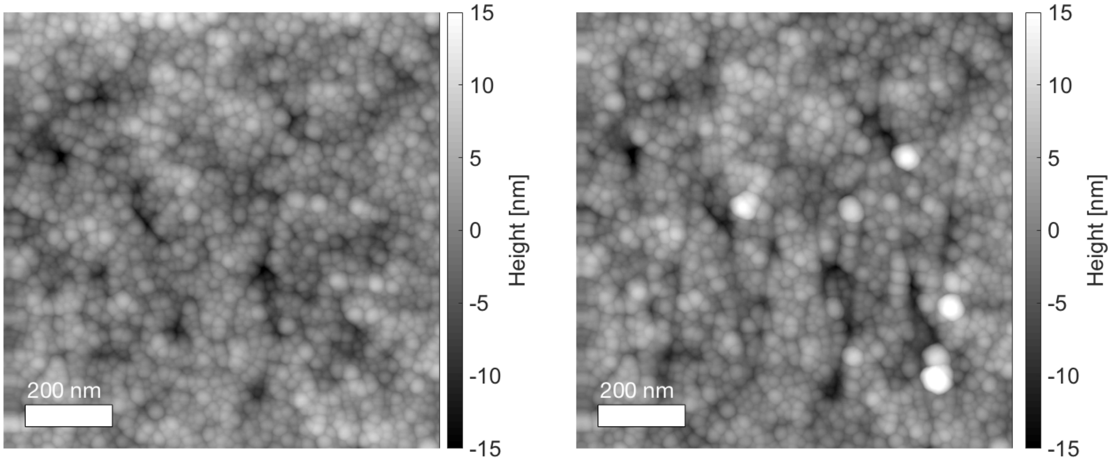

(a) (b)

Figure 7.1: Tapping-mode topography images collected (a) before and (b) after a scratching experiment was performed. The applied load during the scratch test was 400 nN, and the AFM probe moved in a zig-zag pattern from right to left. The scratch pattern is faintly visible in (b), as are several displaced particles.

which are easily scratched; even a light touch from tweezers can damage the film. In order to develop nanoparticle packings for commercial use, they must be more durable. An AFM operating in contact mode can duplicate scratch testing experiments that might otherwise be performed using a tribometer, producing a nanoscale scratch that is similar in size to the nanoparticles, as shown in Figure 7.1. One advantage to using an AFM for this type of experiment is its excellent control over the applied force, which can be less than 100 nN. For materials such as the present nanoparticle packings, severe wear is observed at loads of 400 nN, which is far below what most tribometers are able to accomplish. With this platform for performing scratch testing experiments, it becomes possible to systematically investigate how the tribological properties of these films might be improved. For example, depositing a more densely packed film or using atomic layer deposition or capillary rise infiltration, such as have been discussed in the previous two sections, may help to improve the resistance of nanoparticle packings to scratching.

7.2.5. Nanoindentation on a disordered nanoparticle film under biaxial compression

Disordered nanoparticle packings, in particular those deposited by spin-coating, generally feature a residual tensile stress, as evidenced by their tendency to crack [80] or even form shear bands [62]. It is likely that the mechanical properties of the disordered nanoparticle packings are affected by the state of residual stress. Numerous studies have reported that the triaxial stress state affects the yield criterion in disordered materials, in particular metallic glass [136, 137, 138, 66]. Generally the proposed mechanism is that compression either increases friction on the slip planes on which STZs actuate [138, 66], or that compression increases the packing fraction (or density) of the material. Increasing the packing fraction is known to result in stiffening in granular materials [31] and presumably strength. It is reasonable to assume that disordered nanoparticle packings exhibit similar behavior.

In addition to investigating the failure criterion in disordered nanoparticle packings, it may also be possible to investigate how confinement pressure affects avalanche scaling. Prior research has demonstrated that an increase in confinement pressure increases the cutoff magnitude, ξ, at which the transition between power-law and exponential scaling begins [9]. If a suitable arrangement can be found for creating a confining pressure in a disordered nanoparticle packing, it will be possible to observe whether nanoparticle packings exhibit similar scaling behavior as well.

One potential method for investigating the effect of a confining pressure on the mechanical properties of a disordered nanoparticle packing is to construct a fixture which would allow the substrate to be deformed. A schematic of how this fixture might be constructed is shown in Figure 7.2. The interior may be pumped to low pressure with a vacuum pump, so that atmospheric pressure bends the substrate inward, inducing a compressive stress on the film on top. Nanoindentation or scratch testing experiments may be performed on the top surface under a variety of stress states. A similar fixture could be envisioned to apply a tensile stress, by way of fixing the substrate at the top and applying pressure from beneath, although it is unlikely that such a stress state would be desired in in this particular material system. Cracking observed in thick samples suggests that the residual stress in these

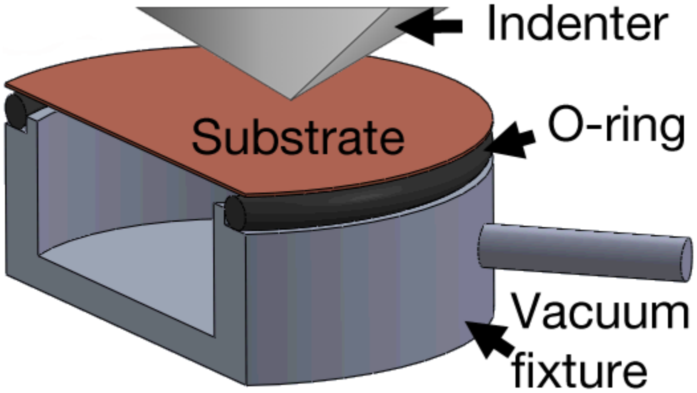

Figure 7.2: Cutaway view of a fixture conceived to allow a thin film to be loaded into compression by bending the substrate. The substrate with a thin film is placed over the hollow fixture and sealed with an O-ring. A vacuum is pulled on the fixture through the hose. Atmospheric pressure causes the substrate to bend, applying a nearly uniform compressive stress at the center of the thin film. By adjusting the pressure and moving to different radial locations, various states of stress can be explored.

nanoparticle films is often close to the film's ultimate strength in tension even in absence of any substrate bending.

An interesting feature of this loading configuration is that the fixture is able to reproduce several different permutations of in-plane stress, including uniaxial and biaxial compression as well as intermediate stress states. This can be accomplished by adjusting the pressure differential and by moving the indentation location to various locations on the surface. Symmetry dictates that the imposed stress state is biaxial compression in the center, but the radial stress and strain decay more rapidly than the azimuthal stress and strain, as shown in Figure 7.3. The applied pressure and the radial position provide two degrees of freedom with which to control the two in-plane principal stresses. The maximum compressive stress that can be obtained is limited by the ultimate strength of the substrate. If the substrate is a $< 100 >$ silicon wafer, this maximum stress state is

$$\sigma_{\max} = \sigma_{\mathrm{Si,max}} \frac{E_{\mathrm{packing}}}{1-\nu_{\mathrm{packing}}} \frac{1-\nu_{\mathrm{Si}}}{E_{\mathrm{Si}}} \approx 7 \text{ GPa} \times 8 \text{ GPa} \, \frac{1-0.25}{130 \text{ GPa}} = 0.32 \text{ GPa}, \tag{7.1}$$

where E_{packing} and E_{Si} are the plane strain moduli of the packing and wafer, respectively,

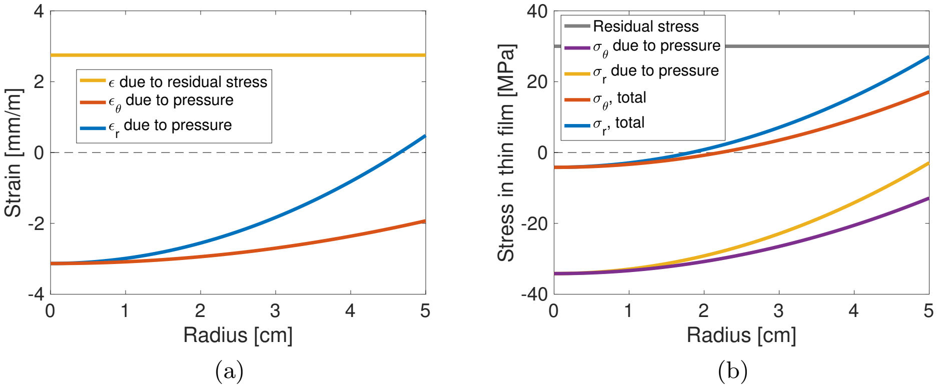

(a) (b)

Figure 7.3: The radial and axial (a) strain and (b) that can be achieved with the indentation jig shown in Figure 7.2. The sample is assumed to be a 500 nm thick nanoparticle packing on a standard size silicon wafer, mounted against a 10 cm O-ring and a vacuum drawn to one half of atmospheric pressure. The lines marked residual stress and strain are rough estimates of the residual tensile stress that results from deposition.

and $\sigma_{\mathrm{Si,max}}$ is the ultimate stress of the silicon. The material properties shown here for silicon are selected from Cheng and Ma [78], and the properties for disordered nanoparticle packings are taken from Lefever et al. [6]. In addition to investigating the mechanical properties of disordered nanoparticle packings under a variety of stress states, this fixture could be used to investigate an almost unlimited selection of materials deposited as thin films. Thin films of metallic glass would be of particular interest to the portion of the scientific community focused on studying disordered solids.

7.3. Implications of these results

For the scientific community, these results represent a new insight into the fundamentals of plastic deformation in disordered materials. For manufacturers and those with commercial interest, these results provide information about how disordered nanoparticle packings might be incorporated into devices. A discussion of the significance of this work to each community follows.

7.3.1. Strengthening films to improve durability in manufactured devices and applications

The current techniques for producing pure disordered nanoparticle packings result in a film which is very weak and subject to scratching even under very light loads. For this reason, it is difficult to imagine this material deployed successfully as an exposed optical coating. For example, disordered nanoparticle packings have been proposed for use on solar cells [19], but would likely not hold up to wind or rain. Further research must be done before the material can hold up to these conditions. Another potential application for disordered nanoparticle packings is chemical sensors [22]. These sensors have the benefit that they are often enclosed and protected from debris and external forces. Nanoprinting shows promise as a means of rapidly manufacturing such devices [20, 21]. However, this technique typically relies on flexible substrates [21] which are compatible with roll-to-roll manufacturing. Bending the flexible substrate will also impose a stress on the film that could cause cracking. Therefore, the response to an applied stress is of substantial importance in both exposed optical coatings and sensors made from flexible substrates, among other applications.

This work demonstrates how the mechanical response of a disordered nanoparticle packing could be expected to change depending on deposition or environmental conditions. For example, in Chapter 4, it was demonstrated that the ductility of a film increases as the humidity increases. It is therefore possible that working under humid conditions might facilitate producing nanoparticle packings on flexible substrates without cracking. Humidity control has also been proposed as a means to target functionalization to particular regions of a nanoparticle film, by controlling the pore size with nanoparticles of different sizes [139]. The present work suggests how this humidity control might affect the mechanics of the film: the portion of the film which has been targeted to produce a capillary will become more ductile than the portion of the film which remains comparatively dry.

In addition to providing useful results, the techniques discussed in this work may be useful for research into manufacturing processes. The AFM is able to quickly produce a large amount of data from a sample with a small physical size. This could speed up the process of characterization in research and development, where large numbers of samples must be tested efficiently.

7.3.2. Using disordered nanoparticle packings to model the response of other disordered materials

Due to the substantial similarities between the disordered nanoparticle packings shown here and many other disordered materials (Section 7.1), it is possible to relate the results from the present material to other disordered materials as well. Making these connections may help to resolve some of the outstanding questions in this field.

As avalanche scaling has been observed in geological materials [8], metallic glasses [118], polymer packings [9], and now nanoparticle packings, it is reasonable to assume that many other disordered materials feature this scaling. Based on the present results, the shape of the avalanche distribution is likely to be affected by system length scales and geometries, but is not likely affected by the strength of particle interactions. Conversely, the number of avalanches that occur under a given loading configuration can be expected to change with the strength of particle interactions, but the shape of the distribution of their magnitudes is not likely to change.

The water content in granular materials is known to affect the strength of forces [7, 112]. This finding can be observed intuitively in a sand castle [98], where a certain amount of water is necessary to maintain structure but an excess of water will cause the castle to lose its structure. Here it is observed that these interactions vary with humidity in two distinct ways. The forces between constituents weaken with an increase in water content due to the change in capillary structure. However, the pull-off force between the tip and sample in fact increases with the water content because of the growth of the capillary bridge. These relationships are likely to be scale-independent and true for larger granular materials such as sand as well.

The results here may also facilitate greater understanding of the spatial extent and number of soft spots or defects that occur in disordered materials. Armed with this information, it will be possible to observe how changing the composition and assembly conditions of a disordered nanoparticle packing affects its strength and durability. These observations have direct analogies to atomic glasses, in that a thermally annealed atomic glass likely behaves similarly to a mechanically annealed or relaxed nanoparticle packing. In the big picture, the results here have significance that could aid in the search for stronger and more fracture-resistant glass for applications as diverse as windows and cellular phone screens.

BIBLIOGRAPHY

[1] Dapeng Bi, Jie Zhang, Bulbul Chakraborty, and R P Behringer. Jamming by shear. *Nature*, 480(7377):355–358, 2011.

[2] A S Argon. Plastic deformation in metallic glasses. *Acta Metallurgica*, 27(1):47–58, 1979.

[3] A Tanguy, F Leonforte, and J L Barrat. Plastic response of a 2D Lennard-Jones amorphous solid: Detailed analysis of the local rearrangements at very slow strain rate. *European Physical Journal E*, 20(3):355–364, 2006.

[4] A J Cao, Y Q Cheng, and E Ma. Structural processes that initiate shear localization in metallic glass. *Acta Materialia*, 57(17):5146–5155, 2009.

[5] Dongchan Jang, Cameron T Gross, and Julia R Greer. Effects of size on the strength and deformation mechanism in Zr-based metallic glasses. *International Journal of Plasticity*, 27(6):858–867, 2011.

[6] Joel A Lefever, Tevis D B Jacobs, Qizhan Tam, Jyo Lyn Hor, Yun-Ru Huang, Daeyeon Lee, and Robert W Carpick. Heterogeneity in the small-scale deformation behavior of disordered nanoparticle packings. *Nano Letters*, 16(4):2455–2462, 2016.

[7] Namiko Mitarai and Franco Nori. Wet granular materials. *Advances in Physics*, 55 (1-2):1–45, 2006.

[8] Jonathan T Uhl, Shivesh Pathak, Danijel Schorlemmer, Xin Liu, Ryan Swindeman, Braden A W Brinkman, Michael LeBlanc, Georgios Tsekenis, Nir Friedman, Robert Behringer, Dmitry Denisov, Peter Schall, Xiaojun Gu, Wendelin J Wright, Todd Hufnagel, Andrew Jennings, Julia R Greer, P K Liaw, Thorsten Becker, Georg Dresen, and Karin A Dahmen. Universal quake statistics: From compressed nanocrystals to earthquakes. *Scientific Reports*, 5:16493, 2015.

[9] D V Denisov, K A Lörincz, J T Uhl, K A Dahmen, and P Schall. Universality of slip avalanches in flowing granular matter. *Nature Communications*, 7:10641, 2016.

[10] William L Johnson. Bulk glass-forming metallic alloys: Science and technology. *MRS Bulletin*, 24(10):42–56, 1999.

[11] W Klement, R H Willens, and Pol Duwez. Non-crystalline structure in solidified gold-silicon alloys. *Nature*, 187:869–870, 1960.

[12] J Robertson. Properties of diamond-like carbon. *Surface and Coatings Technology*, 50(3):185–203, 1992.

[13] Daniel J Strickland, Yun-Ru Huang, Daeyeon Lee, and Daniel S Gianola. Robust scaling of strength and elastic constants and universal cooperativity in disordered colloidal micropillars. *Proceedings of the National Academy of Sciences of the United States of America*, 111(51):18167–72, 2014.

[14] L Vanel, D Howell, D Clark, R P Behringer, and E Clément. Memories in sand: experimental tests of construction history on stress distributions under sandpiles. *Physical Review E*, 60(5):R5040–R5043, 1999.

[15] Th Bauer, P Lunkenheimer, and A Loidl. Cooperativity and the freezing of molecular motion at the glass transition. *Physical Review Letters*, 111(22):225702, 2013.

[16] George E Dieter. *Mechanical Metallurgy.* McGraw-Hill, New York, 3rd edition, 1986.

[17] Kevin T Cook, Kwadwo E Tettey, Robert M Bunch, Daeyeon Lee, and Adam J Nolte. One-step index-tunable antireflection coatings from aggregated silica nanoparticles. *ACS Applied Materials and Interfaces*, 4(12):6426–6431, 2012.

[18] Yun-Ru Huang, Jung Tae Park, Jacob H Prosser, Jong Hak Kim, and Daeyeon Lee. Multifunctional all-$\mathrm{TiO_2}$ Bragg stacks based on blocking layer-assisted spin coating. *Journal of Materials Chemistry C*, 2(17):3260–3269, 2014.

[19] Jung Tae Park, Jong Hak Kim, and Daeyeon Lee. Excellent anti-fogging dye-sensitized solar cells based on superhydrophilic nanoparticle coatings. *Nanoscale*, 6(13):7362–68, 2014.

[20] Seung H Ko, Inkyu Park, Heng Pan, Costas P Grigoropoulos, Albert P Pisano, Christine K Luscombe, and Jean M J Fréchet. Direct nanoimprinting of metal nanoparticles for nanoscale electronics fabrication. *Nano Letters*, 7(7):1869–1877, 2007.

[21] Inkyu Park, Seung H Ko, Heng Pan, Costas P Grigoropoulos, Albert P Pisano, Jean M J Fréchet, Eung Sug Lee, and Jun Ho Jeong. Nanoscale patterning and electronics on flexible substrate by direct nanoimprinting of metallic nanoparticles. *Advanced Materials*, 20(3):489–496, 2008.

[22] Xu Chun Song, Xia Wang, Yi Fan Zheng, Rong Ma, and Hao Yong Yin. A hydrogen peroxide electrochemical sensor based on Ag nanoparticles grown on ITO substrate. *Journal of Nanoparticle Research*, 13(10):5449–5455, 2011.

[23] Jörg F Löffler. Bulk metallic glasses. *Intermetallics*, 11(6):529–540, 2003.

[24] Parmanand Sharma, Neelam Kaushik, Hisamichi Kimura, Yasunori Saotome, and Akihisa Inoue. Nano-fabrication with metallic glass-an exotic material for nano-electromechanical systems. *Nanotechnology*, 18(3):035302, 2007.

[25] Mamoru Ishida, Hideki Takeda, Nobuyuki Nishiyama, Kazuhiko Kita, Yukiharu Shimizu, Yasunori Saotome, and Akihisa Inoue. Wear resistivity of super-precision microgear made of Ni-based metallic glass. *Materials Science and Engineering A*, 448-451(2007):149–154, 2007.

[26] M Z Ma, R P Liu, Y Xiao, D C Lou, L Liu, Q Wang, and W K Wang. Wear resistance of Zr-based bulk metallic glass applied in bearing rollers. *Materials Science and Engineering A*, 386(1-2):326–330, 2004.

[27] L Liu, C L Qiu, C Y Huang, Y Yu, H Huang, and S M Zhang. Biocompatibility of Ni-free Zr-based bulk metallic glasses. *Intermetallics*, 17(4):235–240, 2009.

[28] A Inoue, X M Wang, and W Zhang. Developments and applications of bulk metallic glasses. *Reviews on Advanced Materials Science*, 18:1–9, 2008.

[29] Heinrich M Jaeger, Sidney R Nagel, and Robert P Behringer. Granular solids, liquids, and gases. *Reviews of Modern Physics*, 68(4):1259–1273, 1996.

[30] H P Zhang and H A Makse. Jamming transition in emulsions and granular materials. *Physical Review E - Statistical, Nonlinear, and Soft Matter Physics*, 72(1):1–27, 2005.

[31] Andrea J Liu and Sidney R Nagel. The jamming transition and the marginally jammed solid. *Annual Review of Condensed Matter Physics*, 1:347–369, 2010.

[32] T S Majmudar, M Sperl, S Luding, and R P Behringer. Jamming transition in granular systems. *Physical Review Letters*, 98(5):058001, 2007.

[33] Robert W Balluffi, Samuel M Allen, and W Craig Carter. *Kinetics of materials*. John Wiley & Sons, Hoboken, NJ, 2005.

[34] James G Berryman. Random close packing of hard spheres and disks. *Physical Review A*, 27(2):1053–1061, 1983.

[35] H M Jaeger and S R Nagel. Physics of the granular state. *Science*, 255(5051):1523–1531, 1992.

[36] Robert S Farr and Robert D Groot. Close packing density of polydisperse hard spheres. *Journal of Chemical Physics*, 131(24):244104, 2009.

[37] M L Manning and A J Liu. Vibrational modes identify soft spots in a sheared disordered packing. *Physical Review Letters*, 107:108302, 2011.

[38] Jun Ding, Sylvain Patinet, Michael L Falk, Yongqiang Cheng, and Evan Ma. Soft spots and their structural signature in a metallic glass. *Proceedings of the National Academy of Sciences of the United States of America*, 111(39):14052–14056, 2014.

[39] Y H Liu, D Wang, K Nakajima, W Zhang, A Hirata, T Nishi, A Inoue, and M W Chen. Characterization of nanoscale mechanical heterogeneity in a metallic glass by dynamic force microscopy. *Physical Review Letters*, 106(12):125504, 2011.

[40] Weidong Li, H Bei, Y Tong, W Dmowski, and Y F Gao. Structural heterogeneity induced plasticity in bulk metallic glasses: From well-relaxed fragile glass to metal-like behavior. *Applied Physics Letters*, 103(17):171910, 2013.

[41] Daniel M Sussman, Carl P Goodrich, Andrea J Liu, and Sidney R Nagel. Disordered surface vibrations in jammed sphere packings. *Soft Matter*, 11:2745–2751, 2015.

[42] C R Daley, Z Fakhraai, M D Ediger, and J A Forrest. Comparing surface and bulk flow of a molecular glass former. *Soft Matter*, 8(7):2206, 2012.

[43] Matthew C Wingert, Soonshin Kwon, Shengqiang Cai, and Renkun Chen. Fluid-like surface layer and its flow characteristics in glassy nanotubes. *Nano Letters*, 16(12): 7545–7550, 2016.

[44] E D Cubuk, S S Schoenholz, J M Rieser, B D Malone, J Rottler, D J Durian, E Kaxiras, and A J Liu. Identifying structural flow defects in disordered solids using machine-learning methods. *Physical Review Letters*, 114(10):108001, 2015.

[45] Jörg Rottler, Samuel S Schoenholz, and Andrea J Liu. Predicting plasticity with soft vibrational modes: From dislocations to glasses. *Physical Review E*, 89(4):042304, 2014.

[46] A S Argon and L T Shi. Analysis of plastic flow in an amorphous soap bubble raft by the use of an inter-bubble potential. *Philosophical Magazine A*, 46(2):275–294, 1982.

[47] Frans Spaepen. A microscopic mechanism for steady state inhomogeneous flow in metallic glasses. *Acta Metallurgica*, 25(4):407–415, 1977.

[48] Yuxing Zhou and Scott T Milner. T1 process and dynamics in glass-forming hard-sphere liquids. *Soft Matter*, 11(13):2700–2705, 2015.

[49] Mark Telford. The case for bulk metallic glass. *Materials Today*, 7(3):36–43, 2004.

[50] Bing Liao, Shi Yang Wu, and L Yang. Free volume: An indicator of the glass-forming ability in binary alloys. *AIP Advances*, 7(10):1–13, 2017.

[51] Christopher A Schuh, Alan C Lund, and T G Nieh. New regime of homogeneous flow in the deformation map of metallic glasses: elevated temperature nanoindentation experiments and mechanistic modeling. *Acta Materialia*, 52(20):5879–5891, 2004.

[52] D J Magagnosc, R Ehrbar, G Kumar, M R He, J Schroers, and D S Gianola. Tunable tensile ductility in metallic glasses. *Scientific Reports*, 3:16–18, 2013.

[53] Dominik Tönnies, Robert Maaß, and Cynthia A Volkert. Room temperature homogeneous ductility of micrometer-sized metallic glass. *Advanced Materials*, 26(32): 5715–5721, 2014.

[54] P Gadó. X-ray powder diffraction study of the WO_3 - $W_{20}O_{58}$ shear transformation. *Acta Physica Academiae Scientiarum Hungaricae*, 18(2):111–117, 1965.

[55] R H Baughman, P A Apgar, R R Chance, A G MacDiarmid, and A F Garito. Shear transformation to produce a new phase of polymeric sulfur nitride $(SN)_x$. *The Journal of Chemical Physics*, 71(2), 1976.

[56] A S Argon and H Y Kuo. Plastic flow in a disordered bubble raft (an analog of a metallic glass). *Materials Science and Engineering*, 39(1):101–109, 1979.

[57] Nathan C Keim and Paulo E Arratia. Yielding and microstructure in a 2D jammed material under shear deformation. *Soft Matter*, 9(27):6222, 2013.

[58] Weidong Li, Yanfei Gao, and Hongbin Bei. On the correlation between microscopic structural heterogeneity and embrittlement behavior in metallic glasses. *Scientific Reports*, 5:14786, 2015.

[59] E D Cubuk, R J S Ivancic, S S Schoenholz, D J Strickland, A Basu, Z S Davidson, J Fontaine, J L Hor, Y-R Huang, Y Jiang, N C Keim, K D Koshigan, J A Lefever, T Liu, X-G Ma, D J Magagnosc, E Morrow, C P Ortiz, J M Rieser, A Shavit, T Still, Y Xu, Y Zhang, K N Nordstrom, P E Arratia, R W Carpick, D J Durian, Z Fakhraai, D J Jerolmack, Daeyeon Lee, Ju Li, R Riggleman, K T Turner, A G Yodh, D S Gianola, and Andrea J Liu. Universal signatures of plasticity in disordered solids. *Science*, 358(6366):1033–1037, 2017.

[60] C E Packard and C A Schuh. Initiation of shear bands near a stress concentration in metallic glass. *Acta Materialia*, 55(16):5348–5358, 2007.

[61] A L Greer, Y Q Cheng, and E Ma. Shear bands in metallic glasses. *Materials Science and Engineering: R: Reports*, 74(4):71–132, 2013.

[62] Bin Yang, James S Sharp, and Michael I Smith. Shear banding in drying films of colloidal nanoparticles. *ACS Nano*, 2015.

[63] Peter Schall, David A Weitz, and Frans Spaepen. Structural rearrangements that govern flow in colloidal glasses. *Science*, 318(5858):1895–1899, 2007.

[64] M L Falk and J S Langer. Dynamics of viscoplastic deformation in amorphous solids. *Physical Review E*, 57(6):7192–7205, 1998.

[65] Penghui Cao, Xi Lin, and Harold S Park. Surface shear-transformation zones in amorphous solids. *Physical Review E*, 90(1):012311, 2014.

[66] Christopher A Schuh, Todd C Hufnagel, and Upadrasta Ramamurty. Mechanical behavior of amorphous alloys. *Acta Materialia*, 55(12):4067–4109, 2007.

[67] C Q Chen, Y T Pei, and J T M De Hosson. Effects of size on the mechanical response of metallic glasses investigated through *in situ* TEM bending and compression experiments. *Acta Materialia*, 58(1):189–200, 2010.

[68] D Z Chen, D Jang, K M Guan, Q An, III Goddard, W A, and J R Greer. Nanometallic glasses: Size reduction brings ductility, surface state drives its extent. *Nano Letters*, 13(9):4462–4468, 2013.

[69] Khalid A Alshibli and Stein Sture. Shear band formation in plane strain experiments of sand. *Journal of Geotechnical & Geoenvironmental Engineering*, 126(6):495–503, 2000.

[70] Michael P Marder. *Condensed Matter Physics*. John Wiley & Sons, Hoboken, NJ, 2nd edition, 2010.

[71] Ning Xu, Thomas K Haxton, Andrea J Liu, and Sidney R Nagel. Equivalence of glass transition and colloidal glass transition in the hard-sphere limit. *Physical Review Letters*, 103(24):245701, 2009.

[72] Kamran Karimi, Ezequiel E Ferrero, and Jean-Louis Barrat. Inertia and universality of avalanche statistics: the case of slowly deformed amorphous solids. *Physical Review E*, 95:013003, 2017.

[73] R R Hartley and R P Behringer. Logarithmic rate dependence of force networks in sheared granular materials. *Nature*, 656:928–931, 2003.

[74] Pinshane Y Huang, Simon Kurasch, Jonathan S Alden, Ashivni Shekhawat, Alexander A Alemi, Paul L Mceuen, James P Sethna, Ute Kaiser, and David A Muller. Imaging atomic rearrangements in two-dimensional silica glass: Watching silica's dance. *Science*, 342:224–227, 2013.

[75] Alfred Grill. Diamond-like carbon: State of the art. *Diamond and Related Materials*, 8(2-5):428–434, 1999.

[76] C A Volkert and F Spaepen. Crossover relaxation of the viscosity of $Pd_{40}Ni_{40}P_{19}Si_1$ near the glass transition. *Acta Metallurgica*, 37(5):1355–1362, 1989.

[77] Hai Bin Yu, Wei Hua Wang, and Konrad Samwer. The β relaxation in metallic glasses: An overview. *Materials Today*, 16(5):183–191, 2013.

[78] Y Q Cheng and E Ma. Atomic-level structure and structure-property relationship in metallic glasses. *Progress in Materials Science*, 56(4):379–473, 2011.

[79] Lei Zhang, Gang Feng, Zorana Zeravcic, Teresa Brugarolas, Andrea J Liu, and Daeyeon Lee. Using shape anisotropy to toughen disordered nanoparticle assemblies. *ACS Nano*, 7(9):8043–8050, 2013.

[80] Jacob H Prosser, Teresa Brugarolas, Steven Lee, Adam J Nolte, and Daeyeon Lee. Avoiding cracks in nanoparticle films. *Nano Letters*, 12(10):5287–91, 2012.

[81] Daeyeon Lee, Zekeriyya Gemici, Michael F Rubner, and Robert E Cohen. Multilayers of oppositely charged SiO_2 nanoparticles: Effect of surface charge on multilayer assembly. *Langmuir*, 23(17):8833–8837, 2007.

[82] Daeyeon Lee, Michael F Rubner, and Robert E Cohen. All-nanoparticle thin-film coatings. *Nano Letters*, 6(10):2305–12, 2006.

[83] W C Oliver and G M Pharr. An improved technique for determining hardness and elastic modulus using load and displacement sensing indentation experiments. *Journal of Materials Research*, 7(6):1564–1583, 1992.

[84] W C Oliver and G M Pharr. Measurement of hardness and elastic modulus by instrumented indentation: Advances in understanding and refinements to methodology. *Journal of Materials Research*, 19(1):3–20, 2004.

[85] Greg Haugstad. *Atomic force microscopy*. John Wiley & Sons, Hoboken, NJ, 2012.

[86] Jeffrey L Hutter and John Bechhoefer. Calibration of atomic-force microscope tips. *Review of Scientific Instruments*, 64(7):1868–1873, 1993.

[87] John E Sader, James W M Chon, and Paul Mulvaney. Calibration of rectangular atomic force microscope cantilevers. *Review of Scientific Instruments*, 70(10):3967–3969, 1999.

[88] John E Sader, Ian Larson, Paul Mulvaney, and Lee R White. Method for the calibration of atomic force microscope cantilevers. *Review of Scientific Instruments*, 66(7): 3789–3798, 1995.

[89] Lars-Oliver Heim, Michael Kappl, and Hans-Jürgen Butt. Tilt of atomic force microscope cantilevers: effect on spring constant and adhesion measurements. *Langmuir*, 20(7):2760–2764, 2004.

[90] Jeffrey L Hutter. Comment on tilt of atomic force microscope cantilevers: Effect on spring constant and adhesion measurements. *Langmuir*, 21(6):2630–2632, 2005.

[91] Tevis D B Jacobs, Graham E Wabiszewski, Alexander J Goodman, and Robert W Carpick. Characterizing nanoscale scanning probes using electron microscopy: A novel fixture and a practical guide. *Review of Scientific Instruments*, 87(1):013703, 2016.

[92] Heinrich Hertz. Über die Berührung fester elastischer Körper. *Journal für die Reine und Angewandte Mathematik*, 92:156–171, 1882.

[93] Dongyun Lee, Shengguo Jia, Sarbajit Banerjee, Joze Bevk, Irving P Herman, and Jeffrey W Kysar. Viscoplastic and granular behavior in films of colloidal nanocrystals. *Physical Review Letters*, 98(2):026103, 2007.

[94] Majemite I Dafinone, Gang Feng, Teresa Brugarolas, Kwadwo E Tettey, and Daeyeon Lee. Mechanical reinforcement of nanoparticle thin films using atomic layer deposition. *ACS Nano*, 5(6):5078–87, 2011.

[95] Lei Zhang, Jacob H Prosser, Gang Feng, and Daeyeon Lee. Mechanical properties of atomic layer deposition-reinforced nanoparticle thin films. *Nanoscale*, 4(20):6543–52, 2012.

[96] Danielle S Bassett, Eli T Owens, Mason A Porter, M Lisa Manning, and Karen E Daniels. Extraction of force-chain network architecture in granular materials using community detection. *Soft Matter*, 11:2731–2744, 2015.

[97] Yuhang Chen and Wenhao Huang. Numerical simulation of the geometrical factors affecting surface roughness measurements by AFM. *Measurement Science and Technology*, 15(10):2005–2010, 2004.

[98] C Mathew Mate. *Tribology on the Small Scale*. Oxford University Press, Oxford, 2008.

[99] T Y Tsui and G M Pharr. Substrate effects on nanoindentation mechanical property measurement of soft films on hard substrates. *Journal of Materials Research*, 14(1): 292–301, 1999.

[100] Charles A Clifford and M P Seah. Modelling of nanomechanical nanoindentation measurements using an AFM or nanoindenter for compliant layers on stiffer substrates. *Nanotechnology*, 17(21):5283–5292, 2006.

[101] T S Majmudar and R P Behringer. Contact force measurements and stress-induced anisotropy in granular materials. *Nature*, 435:1079–1082, 2005.

[102] C S O'Hern, L E Silbert, A J Liu, and S R Nagel. Jamming at zero temperature and zero applied stress: The epitome of disorder. *Physical Review E*, 68(1):011306, 2003.

[103] Yang Tse Cheng and Che Min Cheng. Scaling, dimensional analysis, and indentation measurements. *Materials Science and Engineering R: Reports*, 44(4-5):91–149, 2004.

[104] D M Marsh. Plastic flow in glass. *Proceedings of the Royal Society A: Mathematical, Physical and Engineering Sciences*, 279(1378):420–435, 1964.

[105] Yun Liu and Izabela Szlufarska. Chemical origins of frictional aging. *Physical Review Letters*, 109(18):186102, 2012.

[106] Andy Ruina. Slip instability and state variable friction laws. *Journal of Geophysical Research*, 88(B12):10359–10370, 1983.

[107] Qunyang Li, Terry E Tullis, David Goldsby, and Robert W Carpick. Frictional ageing from interfacial bonding and the origins of rate and state friction. *Nature*, 480(7376): 233–236, 2011.

[108] James W Landry, Gary S Grest, Leonardo E Silbert, and Steven J Plimpton. Confined granular packings: structure, stress, and forces. *Physical Review E*, 67(4):041303, 2003.

[109] Chang Liu. *Foundations of MEMS*. Pearson, Upper Saddle River, NJ, 2nd edition, 2012.

[110] B V Derjaguin, V M Muller, and Yu P Toporov. Effect of contact deformations on the adhesion of particles. *Journal of Colloid and Interface Science*, 53(2):314–326, 1975.

[111] Zdeněk Grof, Christopher J Lawrence, and František Štěpánek. The strength of liquid bridges in random granular materials. *Journal of Colloid and Interface Science*, 319 (1):182–192, 2008.

[112] Sabine Leroch and Martin Wendland. Influence of capillary bridge formation onto the silica nanoparticle interaction studied by grand canonical Monte Carlo simulations. *Langmuir*, 29(40):12410–12420, 2013.

[113] Francisco Gallego-Gómez, Víctor Morales-Flórez, Álvaro Blanco, Nicolás de la Rosa-Fox, and Cefe López. Water-dependent micromechanical and rheological properties of silica colloidal crystals studied by nanoindentation. *Nano Letters*, 12(9):1920–4924, 2012.

[114] Yakov I Rabinovich, Joshua J Adler, Madhavan S Esayanur, Ali Ata, Rajiv K Singh, and Brij M Moudgil. Capillary forces between surfaces with nanoscale roughness. *Advances in Colloid and Interface Science*, 96(1-3):213–230, 2002.

[115] Yun-Ru Huang, Yijie Jiang, Jyo Lyn Hor, Rohini Gupta, Lei Zhang, Kathleen J Stebe, Gang Feng, Kevin T Turner, and Daeyeon Lee. Polymer nanocomposite films with extremely high nanoparticle loadings via capillary rise infiltration (CaRI). *Nanoscale*, 7:798–805, 2015.

[116] Jyo Lyn Hor, Yijie Jiang, David J Ring, Robert A Riggleman, Kevin T Turner, and Daeyeon Lee. Nanoporous polymer-infiltrated nanoparticle films with uniform or graded porosity via undersaturated capillary rise infiltration. *ACS Nano*, 11(3): 3229–3236, 2017.

[117] D J Durian. Bubble-scale model of foam mechanics: Melting, nonlinear behavior, and avalanches. *Physical Review E*, 55(2):1739–1751, 1997.

[118] James Antonaglia, Wendelin J Wright, Xiaojun Gu, Rachel R Byer, Todd C Hufnagel, Michael Leblanc, Jonathan T Uhl, and Karin A Dahmen. Bulk metallic glasses deform via slip avalanches. *Physical Review Letters*, 112(15):1–5, 2014.

[119] Wendelin J Wright, Yun Liu, Xiaojun Gu, Katherine D Van Ness, Steven L Robare, Xin Liu, James Antonaglia, Michael LeBlanc, Jonathan T Uhl, Todd C Hufnagel, and Karin A Dahmen. Experimental evidence for both progressive and simultaneous shear during quasistatic compression of a bulk metallic glass. *Journal of Applied Physics*, 119(8):1–6, 2016.

[120] Tohru Okuzono and Kyozi Kawasaki. Intermittent flow behavior of random foams: A computer experiment on foam rheology. *Physical Review E*, 51(2):1246–1253, 1995.

[121] D Dhar and S N Majumdar. Abelian sandpile model on the Bethe lattice. *Journal of Physics A*, 23(19):4333–4350, 1990.

[122] Ivo R Peters, Sayantan Majumdar, and Heinrich M Jaeger. Direct observation of dynamic shear jamming in dense suspensions. *Nature*, 532(7598):214–217, 2016.

[123] Ju-Young Kim, Dongchan Jang, and Julia R Greer. Nanolaminates utilizing size-dependent homogeneous plasticity of metallic glasses. *Advanced Functional Materials*, 21(23):4550–4554, 2011.

[124] Enrico Masoero, Emanuela Del Gado, Roland J-M Pellenq, Sidney Yip, and Franz-Josef Ulm. Nano-scale mechanics of colloidal csh gels. *Soft Matter*, 10(3):491–499, 2014.

[125] Daeyeon Lee, Damali Omolade, Robert E Cohen, and Michael F Rubner. pH-dependent structure and properties of $TiO_{2/}SiO_2$ nanoparticle multilayer thin films. *Chemistry of Materials*, 19(6):1427–1433, 2007.

[126] H A Vinutha and Srikanth Sastry. Disentangling the role of structure and friction in shear jamming. *Nature Physics*, 12(6):578–583, 2016.

[127] Hu Zheng, Joshua A Dijksman, and R P Behringer. Shear jamming in granular experiments without basal friction. *Europhysics Letters*, 107(3):34005, 2014.

[128] G G Adams and M Nosonovsky. Contact modeling-forces. *Tribology International*, 33 (5):431–442, 2000.

[129] Tevis D B Jacobs, Joel A Lefever, and Robert W Carpick. Measurement of the length and strength of adhesive interactions in a nanoscale silicon-diamond interface. *Advanced Materials Interfaces*, 2(9):1400547, 2015.

[130] Xiaodong Li and Bharat Bhushan. A review of nanoindentation continuous stiffness measurement technique and its applications. *Materials Characterization*, 48(1):11–36, 2002.

[131] Pieter Van Der Scheer, Ties Van De Laar, and Jasper Van Der Gucht. Fragility and strength in nanoparticle glasses. *ACS Nano*, 11(7):6755–6763, 2017.

[132] Jeremy Avice, Christophe Boscher, Gwenaelle Vaudel, Guillaume Brotons, Vincent Juve, Mathieu Edely, Christophe Méthivier, Vitalyi E Gusev, Philippe Belleville, Herve Piombini, and Pascal Ruello. Controlling the nanocontact nature and the mechanical properties of a silica nanoparticles assembly. *The Journal of Physical Chemistry C*, 121(42):23769–23776, 2017.

[133] J F Zeng, J P Chu, Y C Chen, A Volland, J J Blandin, S Gravier, and Y Yang. On the use of atomic force microscopy for structural mapping of metallic-glass thin films. *Intermetallics*, 44(2014):121–127, 2014.

[134] E R Nowak, J B Knight, E Ben-Naim, H M Jaeger, and S R Nagel. Density fluctuations in vibrated granular materials. *Physical Review E*, 57(2):1971–1982, 1998.

[135] C Coulais, R P Behringer, and O Dauchot. Dynamics of the contacts reveals Widom lines for jamming. *Europhysics Letters*, 100(4):44005, 2012.

[136] P E Donovan. A yield criterion for $Pd_{40}Ni_{40}P_{20}$ metallic glass. *Acta Metallurgica*, 37 (2):445–456, 1989.

[137] K M Flores and R H Dauskardt. Mean stress effects on flow localization and failure in a bulk metallic glass. *Acta Materialia*, 49(13):2527–2537, 2001.

[138] C A Schuh and T G Nieh. A survey of instrumented indentation studies on metallic glasses. *Journal of Materials Research*, 19(1):46–57, 2004.

[139] Zekeriyya Gemici, Patrick I Schwachulla, Erik H Williamson, Michael F Rubner, and Robert E Cohen. Targeted functionalization of nanoparticle thin films via capillary condensation. *Nano Letters*, 9(3):1064–1070, 2009.